Systematics of metal–silicate partitioning for many siderophile elements applied to Earth's core formation

Julien Siebert [a,b,c,*], Alexandre Corgne [b,d], Frederick J. Ryerson [c]

[a] *Institut de Minéralogie et de Physique des Milieux Condensés, UMR CNRS 7590, Université Pierre et Marie Curie,*
Université Paris Diderot, 4 Place Jussieu, 75005 Paris, France
[b] *Institut de Physique du Globe de Paris, 1 rue Jussieu, 75005 Paris, France*
[c] *Lawrence Livermore National Laboratory, 7000 East Avenue, Livermore, CA 94550, USA*
[d] *Observatoire Midi-Pyrénées, UMR CNRS 5562, 14 avenue Edouard Belin, 31400 Toulouse, France*

Abstract

Superliquidus metal–silicate partitioning was investigated for a number of moderately siderophile (Mo, As, Ge, W, P, Ni, Co), slightly siderophile (Zn, Ga, Mn, V, Cr) and refractory lithophile (Nb, Ta) elements. To provide independent constrains on the effects of temperature, oxygen fugacity and silicate melt composition, isobaric (3 GPa) experiments were conducted in piston cylinder apparatus at temperature between 1600 and 2600 °C, relative oxygen fugacities of IW−1.5 to IW−3.5, and for silicate melt compositions ranging from basalt to peridotite. The effect of pressure was investigated through a combination of piston cylinder and multi-anvil isothermal experiments between 0.5 and 18 GPa at 1900 °C. Oxidation states of siderophile elements in the silicate melt as well as effect of carbon saturation on partitioning are also derived from these results. For some elements (e.g. Ga, Ge, W, V, Zn) the observed temperature dependence does not define trends parallel to those modeled using metal–metal oxide free energy data. We correct partitioning data for solute interactions in the metallic liquid and provide a parameterization utilized in extrapolating these results to the P–T–X conditions proposed by various core formation models. A single-stage core formation model reproduces the mantle abundances of several siderophile elements (Ni, Co, Cr, Mn, Mo, W, Zn) for core–mantle equilibration at pressures from 32 to 42 GPa along the solidus of a deep peridotitic magma ocean (∼3000 K for this pressure range) and oxygen fugacities relevant to the FeO content of the present-day mantle. However, these P–T–fO$_2$ conditions cannot produce the observed concentrations of Ga, Ge, V, Nb, As and P. For more reducing conditions, the P–T solution domain for single stage core formation occurs at subsolidus conditions and still cannot account for the abundances of Ge, Nb and P. Continuous core formation at the base of a magma ocean at P–T conditions constrained by the peridotite liquidus and fixed fO$_2$ yields concentrations matching observed values for Ni, Co, Cr, Zn, Mn and W but underestimates the core/mantle partitioning observed for other elements, notably V, which can be reconciled if accretion began under reducing conditions with progressive oxidation to fO$_2$ conditions consistent with the current concentration of FeO in the mantle as proposed by Wade and Wood (2005). However, neither oxygen fugacity path is capable of accounting for the depletions of Ga and Ge in the Earth's mantle. To better understand core formation, we need further tests integrating the currently poorly-known effects of light elements and more complex conditions of accretion and differentiation such as giant impacts and incomplete equilibration.
© 2011 Elsevier Ltd. All rights reserved.

1. INTRODUCTION

The concentration of siderophile elements in the Earth's mantle is the end result of planetary accretion and core formation. These elements were partitioned between core-forming, iron-rich metallic phases and residual silicate

* Corresponding author at: Institut de Minéralogie et de Physique des Milieux Condensés, UMR CNRS 7590, Université Pierre et Marie Curie, Université Paris Diderot, 4 Place Jussieu, 75005 Paris, France. Tel.: +33 1 44 27 98 19; fax: +33 1 44 27 37 85.
E-mail address: julien.siebert@impmc.jussieu.fr (J. Siebert).

mantle with their distribution controlled by a number of key variables including pressure (P), temperature (T), oxygen fugacity (fO_2) and the chemical compositions (X) of the metallic and silicate phases (e.g. Righter et al., 1997; Li and Agee, 2001). With respect to their chemical implications, current terrestrial core formation models are constrained by the results of partitioning experiments that yield an allowable P–T–X space compatible with the observed siderophile distribution of the mantle. It has been known for many years that the pattern of siderophile depletion (relative to chondrites) in the mantle cannot be explained by simple metal–silicate equilibrium at low pressures (Ringwood, 1966). The abundances of the moderately (e.g. Ni, Co) and highly (e.g. PGEs) siderophile elements in the mantle are generally greater than predicted by low-pressure metal–silicate partition coefficients (e.g. Newsom, 1990; Walter et al., 2000) while the abundances of slightly siderophile elements (e.g. V, Cr) or even elements referred to as lithophile (e.g. Nb) are sometimes more depleted (Drake et al., 1989; Ringwood et al., 1991; Wade and Wood, 2001).

Over the last three decades two classes of model have sought to reconcile this "siderophile element abundances anomaly". (1) Heterogeneous accretion (e.g. Wänke, 1981; Wänke and Dreibus, 1988; Newsom and Sims, 1991; O'Neill, 1991) in which the Earth initially accretes a highly-reduced component followed by the accretion of an oxidized component over approximately the last third of the accretion process. The first reduced phase would result in efficient extraction of siderophile elements into the core, including slightly siderophile elements. Moderately siderophile elements are replenished to their current mantle concentrations during the second oxidized phase of accretion. Finally, the addition of an oxidized "late veneer" is required to account for the abundances of highly siderophile elements in the mantle (e.g. Holzheid et al., 2000; Ertel et al., 2006; Brenan and McDonough, 2009). (2) Homogeneous accretion in which the core equilibrates with the silicate mantle in a "single-stage" event at the base of a deep magma ocean (e.g. Thibault and Walter, 1995; Li and Agee, 1996; Righter et al., 1997; Righter and Drake, 1999; Gessmann and Rubie, 2000; Li and Agee, 2001; Rubie et al., 2003; Chabot et al., 2005). Here, the high-pressure and high-temperature conditions of metal–silicate equilibration shift the partition coefficients of siderophile elements from their low P–T values in such a way that a transition in redox conditions (single fO_2) during core formation is no longer required. The validity of this model obviously depends upon the relative shifts in partitioning behavior with increasing pressure and temperature, and indeed, single-stage core formation has become popular due to its relative simplicity and our ability to test it experimentally. Generally, experimental studies (e.g. Righter et al., 1997; Gessmann and Rubie, 2000; Li and Agee, 2001; Chabot and Agee, 2003; Chabot et al., 2005; Cottrell et al., 2009; Mann et al., 2009) have demonstrated the validity of this scenario for some siderophile elements (e.g. Ni, Co, W, Mo, P, Cr, V) but require disparate magma ocean conditions ranging from 25 to 60 GPa and 2200 K to over 4000 K to reconcile the full range of elements of interest. An intermediate-depth magma ocean scenario at 20–30 GPa and 2000–2500 °C was first proposed (Li and Agee, 1996; Ohtani et al., 1997; Righter

et al., 1997) and is consistent with recent partitioning results for Pd, Mo and P (Righter et al., 2008; Righter et al., 2010). A deeper magma ocean scenario, 40–50 GPa and ∼3000 °C, was later proposed based on V–Cr–Mn (e.g. Gessmann and Rubie, 2000) and additional Ni–Co partitioning data (Li and Agee, 2001). More recently Wade and Wood (2005) also concluded that the metal–silicate partitioning of V, Ni, Co, Mn and Si were compatible with single stage core formation at ∼3500 °C, 40 GPa, but questioned the physical plausibility of the single-stage core formation model since the required temperature greatly exceeds that of the peridotite liquidus, the maximum basal temperature for a terrestrial magma ocean (see also, Corgne et al., 2008; Wood et al., 2008). An alternative, continuous accretion/core formation model was proposed in which metal–silicate equilibration takes place at the base of a magma ocean with increasing P–T conditions, defined by the P–T coordinates of the peridotite liquidus. To match observed siderophile abundance patterns this model also requires that the oxygen fugacity of the mantle increases with time due to "self-oxidation" resulting from pressure-induced stabilization of the perovskite and associated disproportionation of ferrous iron (Wade and Wood, 2005). That modulation of pressure, temperature and oxygen fugacity highlights the need to constrain independently the influence of each of these variables.

To test proposed scenarios of metal–silicate equilibration, internally consistent sets of partitioning data are required over a wide range of pressure and temperature. Furthermore, it requires integration of data for a large number of elements representing various degrees of siderophility and valences to refine a solution that is a function of multiple variables (P, T, fO_2, silicate and metal compositions). Despite numerous publications on metal–silicate partitioning, the experimental database and predictive expressions for elements partitioning are hampered by a lack of systematic investigations that separate these effects. Although a relatively complete experimental database describing Ni and Co partitioning now exists, it is not sufficient to unambiguously resolve proposed core formation models. For instance, new results on Ni and Co by Kegler et al. (2008) are in conflict with those previously obtained for these two elements (e.g. Chabot et al., 2005).

Here, we present new experimental metal–silicate partitioning for a large number of key elements normally regarded as moderately siderophile (Mo, As, Ge, W, P, Ni, Co), slightly siderophile (Zn, Ga, Mn, V, Cr), and refractory lithophile (Nb, Ta). Experiments were designed to systematically sample and separate the effects of each variable (P, T, silicate composition and fO_2) in isolation. These new data enhance our ability to model the chemistry of core formation in a number of respects. The effect of temperature on partitioning has been carefully studied for each element over a wide range of superliquidus temperatures. Hence, the temperature dependence of metal–silicate partitioning can now be modeled using experimental constraints rather than estimates (e.g. for Ga, Zn, V) based on the free energy of the metal–silicate exchange reactions for pure metal and oxide liquids (Wade and Wood, 2005; Corgne et al., 2008). While metal–silicate equilibration at the base of a terrestrial magma ocean implies a peridotite composition for the silicate melt, most of

the experiments in the existing database utilize basaltic compositions. Here, the majority of our experiments were carried out using a melt of peridotite composition, but we have also investigated the influence of silicate melt composition by performing additional experiments using a basalt composition. The dependence of partitioning on fO_2 was characterized to infer the valence states of siderophile elements in the silicate melts at relevant redox conditions for core formation. Generally, we provide enhanced constraints on the partitioning of some extensively considered elements, notably Ni, Co, and W, but also for elements that were poorly constrained and integrated in previous experiments and core formation modeling (e.g. Ge, As). In addition, we extend significantly the studied P–T ranges for additional elements (e.g. Mo, Zn, Ga, P) with relatively well-defined depletions in the Earth's mantle. This allows us to improve greatly thermodynamic parameterizations required to extrapolate partitioning to predicted conditions of core formation. Volatility loss (or incomplete condensation) of some studied elements might exceed their siderophile behavior. This experimental work provides insight to evaluate if the depletions in the mantle of Zn, Ge, and Ga for instance are due to their volatility or a combination of this and sequestration into the core. These results are applied in testing the chemical plausibility of a single-stage core formation in a magma ocean and to the more recent hypothesis of continuous polythermal–polybaric core segregation.

2. EXPERIMENTAL METHODS

Experiments were performed at 0.5–18 GPa at temperatures between 1600 and 2600 °C using an end-loaded piston cylinder apparatus (0.5–3 GPa) and a 1000-ton multi-anvil press (5–18 GPa) at the Lawrence Livermore National Laboratory (LLNL). Table 1 provides a summary of run conditions.

Two different 1/2″ piston–cylinder assemblies were used in these experiments. Experiments between 1600 and 1850 °C were conducted using a standard $BaCO_3$ pressure cell, MgO spacers and graphite or MgO capsules (Fig. 1a). Experiments between 1850 and 2600 °C employed a furnace design developed by Cottrell and Walker (2006), comprising a Ca-doped $LaCrO_3$ insulator inserted between the $BaCO_3$ pressure cell and a shortened graphite furnace (Fig. 1b). Temperature was monitored using a type D thermocouple ($W_{97}Re_3/W_{75}Re_{25}$) inserted axially in an alumina or magnesia four-bore thermocouple sleeve above the capsule. Beyond type D thermocouple calibration range (~2350 °C), we either continued to read temperature or estimated it with a well-constrained and reproducible output power-temperature regression line (Fig. 1c). The latter case was used for experiments at temperature close to the eutectic in the W–Re system (~2600 °C) where the thermocouple failed. Temperatures in excess of the melting point of Al_2O_3 (~2000 °C) or the MgO–Al_2O_3 eutectic (~1875 °C) often resulted in heater failure or MgO and Al_2O_3 contamination after short run durations. To allow longer run durations and minimize contamination, experiments were performed either without thermocouple or with MgO four-bore thermocouple tubing (Saint Gobain Industrial Ceramics product). Temperature uncertainties are esti-

mated as less than ±50 °C for all runs. At temperature above 2000 °C, piston life was significantly increased by the addition of a 1.5 mm thick steel disk placed between the piston and the assembly to prevent direct contact between the furnace assembly and the WC piston (Wade and Wood, 2002). Samples were first taken to run pressure, then heated to 900 °C and sintered at that temperature for 6–12 h. Runs were then held at 1400 °C for 10 min to stabilize the pressure before quickly ramping (200–400 °C/min) to run temperatures. Run durations varied inversely with temperature from 15 min for lowest temperature runs to 1 min for the highest temperature runs. This limited infiltration and interaction of the low viscosity melts contained in our samples with the assembly. Thibault and Walter (1995) and Corgne et al. (2008) have shown that run durations as short as few tens of second were sufficient to reach chemical equilibrium at similar P–T conditions. All the piston-cylinder assemblies were wrapped with Pb foil to lubricate the pressure vessel for easier extraction and to reduce frictional loss. Pressure was calibrated using the Al_2O_3 content of orthopyroxene coexisting with pyrope (Perkins et al., 1981) leading to less than 10% friction loss correction (Appendix A). McDade et al. (2002) reported a 9% friction loss for standard 1/2″ $BaCO_3$ pressure cell assembly consistent with results from our work.

Multi-anvil isothermal experiments (1850–1900 °C) were carried out using 10 mm edge length octahedral pressure assemblies and 5 mm truncated edge length cubic WC anvils. The sample assembly consisted of a pure MgO octahedron with rhenium foil heaters contained within $LaCrO_3$ thermal insulation sleeve, along with a combination of MgO and ZrO_2 spacers (Fig. 1). MgO capsules were used instead of graphite. As observed in previous works (Thibault and Walter, 1995), runs performed with C-capsules led to significant loss and migration of the liquid metal through the container even for short run duration. This is due to low surface tension between the liquid metal and the capsule that has partially transformed to diamond. The multi-anvil assembly was calibrated for pressure using the SiO_2 coesite–stishovite transition at 9 GPa–1200 °C, Mg_2SiO_4 forsterite to wadsleyite (α–β) at 14 GPa–1300 °C and wadsleyite to ringwoodite (β–γ) at 18 GPa–1100 °C. Temperature was monitored using a C-type thermocouple ($W_{95}Re_5/W_{74}Re_{26}$) inserted axially in an alumina four bore thermocouple sleeve above the capsule. No pressure correction was applied to the thermocouple emf. Uncertainty in pressure and temperature are estimated around ±10% and ±50 °C. Note that estimation of pressure uncertainty integrates the slight drop in pressure at run temperatures greater than those of the pressure calibration temperatures. The effect of temperature on pressure at constant load has been well constrained for this 10/5 designed COMPRES assembly. Experiments were raised to target pressures before ramping at 100 °C/min to run temperature. Run duration was kept short (90 s) to avoid percolation of the metal through the polycrystalline MgO capsules and limit MgO contamination of the samples. Recovered capsules were mounted in epoxy resin, polished down to 1 μm and carbon-coated for chemical analyses.

Starting materials were prepared by mixing metallic powders of Fe, Ni and Si with ground natural KLB-1

Table 1
Experimental conditions.

Run #	T (°C)	P (GPa)	t (min)	ΔIW^a	ΔIW^b	nbo/t^c	Capsule material/silicate composition
50	1850	1.5	15	−1.44	−0.65	3.66	Graphite/KLB1
51	1850	1.5	3	−1.47	−0.68	3.58	Graphite/KLB1
52	1850	1.5	10	−1.99	−1.64	4.13	MgO/KLB1
85	2200	2.5	5	−2.08	−1.27	4.61	Graphite/KLB1
93	2000	3	3	−1.99	−1.18	3.30	Graphite/KLB1
94	1900	3	5	−1.79	−0.99	3.39	Graphite/KLB1
95	2100	3	3	−1.98	−1.17	3.82	Graphite/KLB1
96	2200	3	3	−1.57	−0.79	4.42	Graphite/KLB1
97	2300	3	3	−1.87	−1.09	3.52	Graphite/KLB1
101	1600	3	15	−1.54	−0.75	1.22	Graphite/basalt
102	2000	3	6	−2.05	−1.24	3.42	Graphite/KLB1
103	2200	3	2	−2.22	−1.42	4.06	Graphite/KLB1
116	1850	3	15	−2.28	−1.48	2.93	Graphite/KLB1
118	1900	3	5	−2.35	−1.56	2.94	Graphite/KLB1
120	2000	3	3	−2.74	−1.97	4.15	Graphite/KLB1
121	2100	3	2	−2.30	−1.51	2.88	Graphite/KLB1
122	2200	3	2	−2.42	−1.64	3.00	Graphite/KLB1
124	1850	3	10	−1.96	−1.16	2.81	Graphite/KLB1
126	1850	3	15	−1.76	−0.96	1.06	Graphite/basalt
127	1700	3	15	−1.81	−1.00	1.05	Graphite/basalt
128	1600	3	15	−1.81	−1.02	1.06	Graphite/basalt
129	2300	3	2	−2.11	−1.33	3.02	Graphite/KLB1
130	2400	3	1.5	−2.07	−1.28	2.92	Graphite/KLB1
131	2500	3	1.5	−1.98	−1.20	2.90	Graphite/KLB1
132	2600^d	3	1	−2.19	−1.41	3.31	Graphite/KLB1
133	2200	3	2	−2.18	−1.38	2.86	Graphite/KLB1
134	2200	3	3	−2.60	−1.82	2.11	Graphite/basalt
135	2200	3	2	−3.27	−2.46	2.56	Graphite/KLB1
139	1850	3	3	−2.27	−1.92	3.15	MgO/KLB1
140	1850	3	3	−2.47	−2.12	2.94	MgO/basalt
141	1850	2	3	−2.57	−2.22	3.28	MgO/basalt
142	1850	1	3	−2.10	−1.74	3.39	MgO/basalt
143	1850	3	5	−1.83	−1.04	1.56	Graphite/basalt + KLB1
144	1850	3	5	−1.91	−1.12	2.16	Graphite/basalt + KLB1
145	1850	0.5	2	−2.22	−1.87	3.04	MgO/basalt
MA17	1900	10	2	−2.63	−2.28	2.63	MgO/basalt
MA18	1850	10	1.5	−2.63	−2.28	2.90	MgO/basalt
MA20	1850	5	1.5	−2.55	−2.20	3.83	MgO/basalt
MA21	1900	15	1.5	−2.34	−1.99	2.55	MgO/basalt
MA22	1900	18	1.5	−2.42	−2.07	2.48	MgO/basalt

[a] Oxygen fugacity relative to the iron-wüstite buffer calculated assuming ideal mixing behavior.

[b] Oxygen fugacity relative to the iron-wüstite buffer calculated assuming non ideal mixing. γ_{Fe}^{metal} and $\gamma_{FeO}^{silicate}$ are different from unity (see text for details).

[c] nbo/t is calculated according to Mysen et al. (1982) and considering all cations in the oxidation state determined for conditions of our experiments (i.e. W^{4+}, Mo^{4+}, Cr^{2+}, Ge^{3+}).

[d] Temperature estimated with a power-temperature regression line (see Fig. 1).

peridotite or/and olivine tholeiite basalt (Kilauea, Hawaii, see composition in Hofmann and Magaritz (1977)). The silicate portions of the starting mixtures were previously doped with trace amounts of high-purity oxides at 1–2 wt% level. Addition of silicon metal was required to balance the excess of oxygen introduced by the addition of oxides and to maintain relatively low oxygen fugacity (∼IW-2). To assess the effect of silicate melt composition on partitioning, various proportions of tholeiite basalt and KLB-1 peridotite were mixed together and used to make the silicate portion of some of the starting mixtures. These compositions produced silicate melts with intermediate nbo/t (molar ratio of non-bridging oxygens per tetrahe-

drally coordinated cations) between 1 and 2.8. Mixed portions of metal relative to silicate ranged between 20 and 40 wt%. Starting powders were grounded and homogenized in an agate mortar under ethanol.

All samples contained several quench blebs of molten alloy from 20 to 400 μm in diameter (average size ∼200 μm) surrounded by quench silicate melt. Fig. 2 shows backscattered-electron images of typical run products. Experiments in which tholeiitic basalt was used as the silicate starting material (low nbo/t), typically quenched to a homogeneous glass (Fig. 2c). Experiments that included KLB1 peridotite as the starting composition or used MgO capsules resulted in less polymerized melt compositions
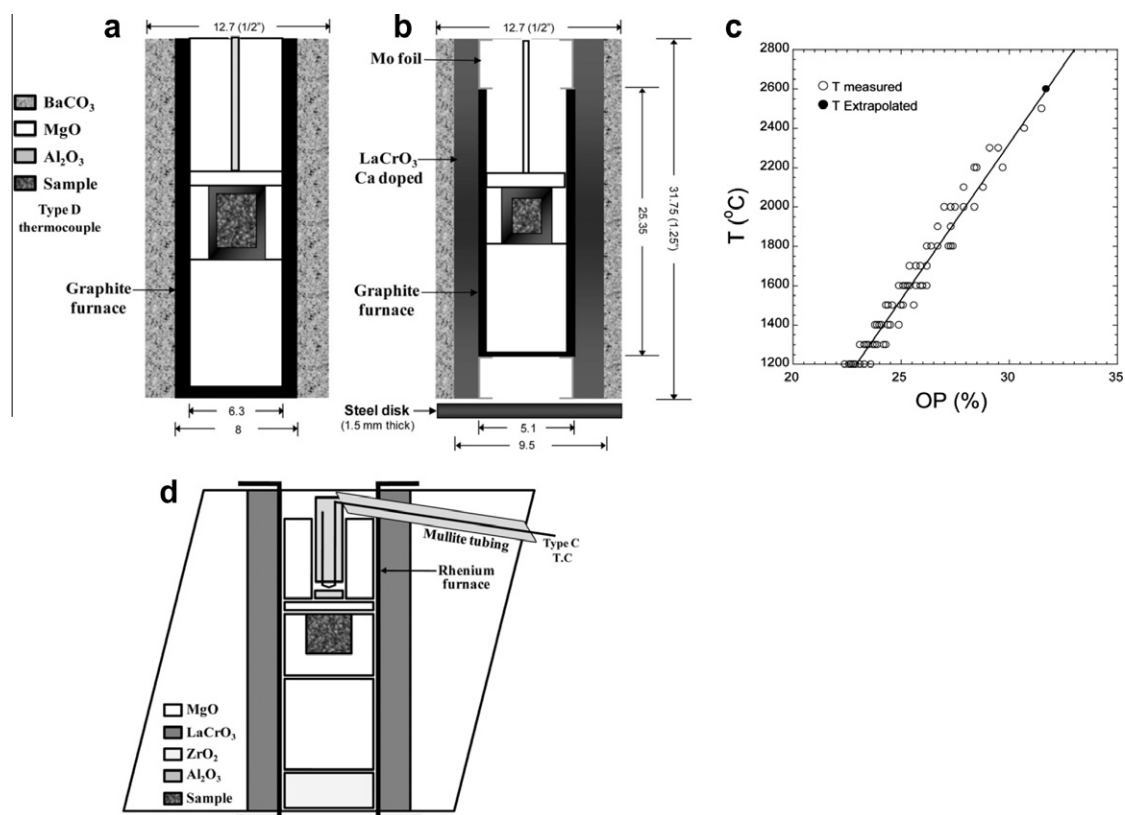
Fig. 1. Piston-cylinder and multi-anvil assemblies used in the present work. (a) Piston cylinder assembly used to cover temperature below 1850 °C. (b) Piston cylinder assembly used to cover high temperature range between 1900 and 2600 °C. (c) Power input-measured temperature regression line for temperature calibration of piston cylinder experiment conducted at 2600 °C without thermocouple to avoid possible contamination. (d) Multi-anvil assembly used to cover pressure above 3 GPa.
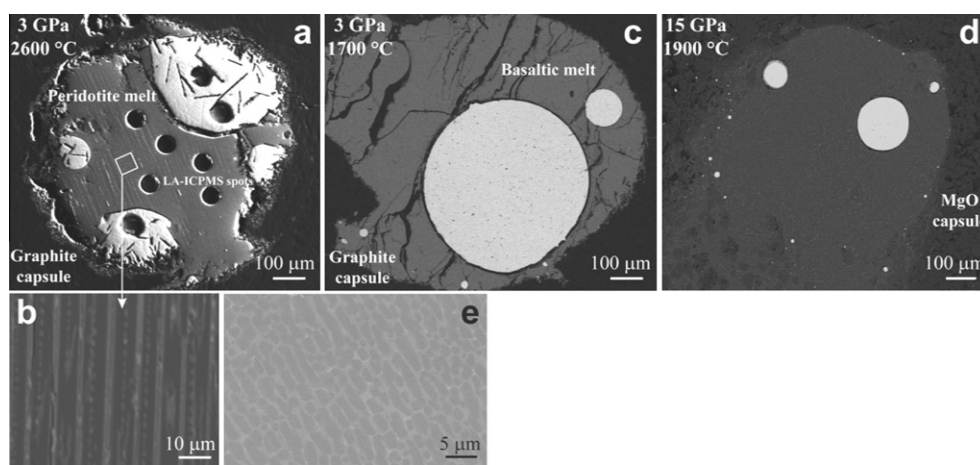

Fig. 2. Electron images of typical run products. (a) Secondary electron image of sample #132 (3 GPa, 2600 °C) contained in graphite capsule. Metallic phases (white) and silicate melt (gray) are well separated. A 60 μm diameter laser ablation beam was used for both metal and silicate analyses to reintegrate quenched compositions. Metals contained in graphite capsules quenched to C-bearing alloys containing laths of graphite. Graphite is likely the product of both quench and carbon saturation at runs conditions. (b) Back-scattered electron image of the region enclosed by the white frame showing quench texture of peridotite melt composed of dendritic quenched olivine crystals and interstitial melt (brighter gray). (c) Back-scattered electron image of sample #127 (3 GPa, 1700 °C) contained in graphite capsule. Basaltic melt quenched as a homogeneous silicate glass. (d) Back-scattered electron image of a multi-anvil sample #MA21 (15 GPa, 1900 °C) contained in MgO capsule. Silicate melt quenched to a heterogeneous texture resulting from reactions with the capsule and MgO enrichment of the basaltic melt. Note that the presence of nanonuggets in silicate melt was not observed by SEM imaging or time-resolved LA-ICPMS analyses. (e) Back-scattered electron image of typical quenched texture of C-rich alloy (#132) observed in experiments performed with graphite capsules.

Table 2
Average major and trace element compositions of the quenched silicate melts determined by EPMA and LA-ICPMS.

Run #	50	51	52	85	93	94	95	96	97	101	102	103
EPMA (wt%)	$N = 32$[a]	$N = 40$	$N = 20$	$N = 20$	$N = 17$	$N = 22$	$N = 15$	$N = 21$	$N = 19$	$N = 38$	$N = 16$	$N = 20$
MgO	37.59 (1.22)[b]	37.07 (1.12)	43.99 (2.09)	48.47 (1.59)	40.92 (1.05)	40.22 (1.45)	44.32 (1.04)	43.58 (1.15)	41.30 (1.45)	7.48 (0.32)	40.40 (1.55)	46.73 (1.73)
SiO_2	37.03 (0.59)	37.16 (0.56)	35.24 (1.78)	34.85 (1.39)	41.08 (0.79)	40.38 (0.53)	38.03 (0.80)	34.52 (0.78)	38.95 (0.69)	44.84 (0.40)	40.66 (1.08)	37.4 (1.15)
Al_2O_3	2.14 (0.28)	2.21 (0.22)	2.03 (0.37)	1.02 (0.05)	1.85 (0.11)	1.75 (0.18)	1.62 (0.12)	1.34 (0.13)	2.06 (0.25)	10.45 (0.11)	1.19 (0.19)	1.18 (0.25)
CaO	1.36 (0.18)	1.41 (0.16)	2.15 (0.48)	2.31 (0.22)	1.78 (0.12)	1.43 (0.20)	1.59 (0.14)	2.02 (0.21)	1.65 (0.11)	10.17 (0.16)	1.32 (0.23)	1.22 (0.21)
Na_2O	0.34 (0.06)	0.31 (0.06)	0.31 (0.05)	0.33 (0.04)	0.08 (0.005)	0.14 (0.018)	0.12 (0.01)	0.02 (0.05)	0.18 (0.01)	1.88 (0.08)	0.09 (0.01)	–
K_2O	0.07 (0.01)	0.07 (0.01)	0.11 (0.02)	0.09 (0.01)	–	–	0.07 (0.01)	0.040 (0.006)	0.05 (0.01)	0.32 (0.02)	0.02 (0.04)	–
FeO	15.98 (0.55)	15.26 (0.63)	11.48 (0.86)	7.44 (0.69)	8.90 (0.28)	11.27 (0.48)	9.24 (0.42)	14.73 (0.33)	10.14 (0.61)	13.08 (0.43)	7.81 (0.56)	6.74 (0.52)
Ga_2O_3	0.383 (0.048)	0.417 (0.034)	0.104 (0.030)	0.492 (0.055)	0.237 (0.018)	0.303 (0.026)	0.260 (0.026)	0.288 (0.028)	0.292 (0.019)	0.452 (0.023)	0.314 (0.030)	0.312 (0.033)
MnO	0.853 (0.027)	0.846 (0.031)	0.602 (0.040)	0.589 (0.025)	0.429 (0.010)	0.448 (0.032)	0.443 (0.027)	0.346 (0.015)	0.480 (0.025)	1.985 (0.036)	1.440 (0.066)	1.305 (0.108)
GeO_2	–	–	–	0.042 (0.005)	–	–	–	0.064 (0.008)	0.037 (0.004)	–	–	–
P_2O_5	0.026 (0.003)	0.024 (0.003)	0.010 (0.005)	0.600 (0.043)	0.295 (0.018)	0.458 (0.029)	0.391 (0.027)	0.431 (0.026)	0.299 (0.024)	0.062 (0.003)	0.305 (0.039)	0.371 (0.034)
As_2O_5	–	–	–	–	–	–	–	–	–	–	–	–
Nb_2O_5	0.870 (0.090)	0.780 (0.070)	0.334 (0.041)	0.555 (0.038)	0.249 (0.023)	0.191 (0.015)	0.261 (0.020)	0.173 (0.016)	0.233 (0.018)	1.208 (0.016)	0.688 (0.067)	0.254 (0.032)
SO_3	0.018 (0.003)	0.021 (0.003)	0.011 (0.003)	0.047 (0.007)	0.012 (0.004)	0.009 (0.003)	0.013 (0.006)	0.069 (0.004)	0.010 (0.005)	–	0.038 (0.008)	0.031 (0.007)
CoO	0.064 (0.005)	0.062 (0.005)	0.032 (0.004)	0.042 (0.004)	0.021 (0.003)	0.023 (0.002)	0.022 (0.002)	0.030 (0.005)	0.022 (0.003)	0.016 (0.002)	0.012 (0.002)	0.011 (0.003)
MoO_3	–	–	–	–	–	–	–	–	–	–	–	–
NiO	0.020 (0.005)	0.020 (0.004)	–	0.018 (0.004)	0.014 (0.003)	0.016 (0.003)	0.014 (0.002)	0.017 (0.004)	0.021 (0.003)	–	0.013 (0.002)	0.018 (0.004)
ZnO	–	–	–	–	–	–	–	–	–	–	–	–
TiO_2	0.978 (0.113)	0.976 (0.098)	0.426 (0.021)	0.073 (0.008)	0.684 (0.050)	0.642 (0.057)	0.744 (0.050)	0.606 (0.049)	0.678 (0.052)	2.706 (0.043)	0.695 (0.056)	0.537 (0.047)
Ta_2O_5	–	–	–	0.548 (0.042)	0.517 (0.033)	0.433 (0.033)	0.593 (0.045)	0.391 (0.031)	0.518 (0.039)	1.312 (0.045)	0.896 (0.075)	0.422 (0.038)
V_2O_3	0.580 (0.070)	0.67 (0.096)	0.263 (0.032)	0.465 (0.039)	0.922 (0.091)	0.943 (0.065)	0.872 (0.078)	0.561 (0.047)	0.914 (0.012)	1.410 (0.027)	1.211 (0.085)	1.020 (0.094)
WO_3	0.243 (0.035)	0.221 (0.033)	0.111 (0.014)	0.128 (0.011)	–	0.019 (0.007)	0.024 (0.004)	0.222 (0.038)	0.011 (0.006)	–	–	0.063 (0.009)
Cr_2O_3	0.951 (0.110)	1.060 (0.111)	0.336 (0.055)	0.638 (0.048)	0.825 (0.065)	0.868 (0.059)	0.703 (0.083)	0.599 (0.064)	0.782 (0.041)	1.142 (0.040)	1.121 (0.011)	0.900 (0.092)
Total[c]	99.50	98.59	97.54	98.75	98.81	99.55	99.61	100.25	99.06	98.53	98.22	98.51

LA–ICPMS (ppm)

	116	118	120	121	122	124	126	127	128	129	130	131
P 31	117 (6)	153 (10)	55 (4)	–	–	2206 (85)	2088 (101)	2272 (92)	1921 (126)	234 (14)	–	–
Ti 47	5906 (115)	5712 (110)	2615 (222)	–	–	3631 (93)	4246 (106)	3577 (38)	3953 (126)	16,838 (302)	–	–
V 51	3987 (254)	4699 (185)	2038 (115)	–	–	6295 (319)	5925 (225)	4437 (204)	6588 (206)	10,900 (390)	–	–
Cr 52	7012 (299)	7338 (150)	2514 (214)	–	–	5780 (296)	4632 (139)	3681 (178)	5139 (235)	7981 (238)		
Mn 55	7405 (170)	7209 (183)	5113 (110)	–	3661 (220)	3987 (240)	3232 (108)	2332 (80)	4084 (225)	16,258 (487)	–	–
Co 59	374 (15)	366 (16)	228 (11)	–	115 (7)	121 (11)	86 (4)	156 (6)	132 (4)	43 (2)	–	–
Ni 60	205 (9)	202 (10)	121 (7)	–	–	123 (12)	83 (5)	148 (6)	189 (11)	73 (5)	–	–
Zn 66	57 (2)	63 (3)	38 (4)	–	–	97 (3)	141 (6)	80 (2)	78 (5)	80 (5)	–	–
Ga 69	6047 (142)	6796 (182)				4739 (115)	4079 (137)	4537 (78)	4604 (83)	4925 (291)		
Ge 72	374 (12)	396 (18)	98 (10)	–	112 (14)	314 (20)	366 (22)	813 (25)	666 (30)	48 (1)	–	–
As 75	–	–	–	–	–	0.25 (0.02)	0.25 (0.02)	0.75 (0.05)	0.45 (0.1)	–	–	–
Nb 93	7396 (186)	6750 (144)	3751 (548)	–	1451 (49)	1501 (34)	1957 (45)	1238 (42)	1798 (66)	8701 (310)	–	–
Mo 95	37 (1.5)	35 (2)	47 (8)	–	9 (1)	8 (1)	8 (1)	48 (0.5)	14 (2)	3 (0.5)	–	–
Ta 181	–	–	–	–	4386 (101)	3515 (80)	4420 (55)	3414 (113)	4105 (125)	11,279 (427)	–	–
W 182	–	–	–	–	89 (4)	214 (9)	249 (13)	2066 (118)	193 (5)	36 (3)	–	–
Run #	116	118	120	121	122	124	126	127	128	129	130	131
EPMA (wt%)	$N = 40^a$	$N = 25$	$N = 40$	$N = 26$	$N = 20$	$N = 64$	$N = 40$	$N = 40$	$N = 45$	$N = 48$	$N = 45$	$N = 45$
MgO	37.04 (1.25)^b	38.18 (1.35)	49.34 (0.85)	36.95 (1.21)	39.35 (1.28)	34.00 (1.09)	8.54 (0.11)	8.39 (0.15)	8.23 (0.09)	38.16 (1.11)	37.41 (0.73)	34.99 (1.30)
SiO_2	42.79 (0.63)	43.07 (1.14)	37.17 (0.65)	43.30 (0.58)	42.90 (1.00)	43.04 (0.71)	47.55 (0.39)	47.94 (0.40)	47.06 (0.52)	43.14 (0.79)	43.68 (0.46)	42.43 (1.41)
Al_2O_3	2.44 (0.14)	2.18 (0.17)	1.63 (0.24)	2.37 (0.16)	2.19 (0.18)	2.63 (0.17)	11.01 (0.10)	11.02 (0.12)	11.02 (0.10)	2.15 (0.23)	2.22 (0.10)	2.14 (0.15)
CaO	1.51 (0.13)	1.66 (0.20)	1.25 (0.21)	1.67 (0.12)	1.48 (0.15)	1.60 (0.10)	9.27 (0.08)	9.38 (0.09)	9.27 (0.06)	1.81 (0.26)	1.44 (0.07)	2.57 (0.15)
Na_2O	0.26 (0.02)	0.25 (0.019)	0.17 (0.04)	0.30 (0.03)	0.26 (0.03)	0.31 (0.04)	1.90 (0.10)	1.92 (0.07)	1.92 (0.05)	0.30 (0.03)	0.26 (0.03)	0.33 (0.03)
K_2O	0.09 (0.03)	0.05 (0.01)	0.07 (0.005)	0.08 (0.01)	0.06 (0.01)	0.09 (0.02)	0.41 (0.01)	0.41 (0.01)	0.41 (0.01)	0.08 (0.01)	0.08 (0.01)	0.10 (0.01)
FeO	6.45 (0.18)	5.95 (0.19)	4.03 (0.36)	6.21 (0.28)	5.37 (0.21)	8.78 (0.30)	10.25 (0.44)	9.89 (0.32)	9.86 (0.41)	7.40 (0.33)	7.59 (0.28)	8.13 (0.44)
Ga_2O_3	0.457 (0.021)	0.426 (0.038)	0.379 (0.044)	0.478 (0.032)	0.400 (0.031)	0.451 (0.036)	0.493 (0.010)	0.549 (0.022)	0.577 (0.015)	0.449 (0.037)	0.444 (0.017)	0.408 (0.042)
MnO	1.136 (0.040)	1.027 (0.049)	0.973 (0.041)	1.138 (0.044)	1.047 (0.056)	1.205 (0.061)	1.131 (0.022)	1.141 (0.023)	1.148 (0.021)	1.158 (0.028)	1.202 (0.024)	1.048 (0.041)
GeO_2	–	–	–	–	–	–	–	–	–	–	–	–
P_2O_5	0.081 (0.005)	0.090 (0.005)	0.308 (0.041)	0.087 (0.005)	0.072 (0.006)	0.102 (0.008)	0.023 (0.002)	0.029 (0.002)	0.033 (0.003)	0.130 (0.010)	0.099 (0.006)	0.109 (0.019)
As_2O_5	–	–	–	–	–	–	–	–	–	–	–	–
Nb_2O_5	1.189 (0.051)	0.701 (0.056)	0.962 (0.136)	1.077 (0.089)	0.784 (0.092)	1.284 (0.141)	1.164 (0.019)	1.198 (0.029)	1.218 (0.016)	1.047 (0.099)	1.060 (0.067)	0.802 (0.069)
SO_3	–	–	0.008 (0.004)	0.011 (0.003)								0.081 (0.030)
CoO	0.009 (0.004)	0.012 (0.004)	0.007 (0.003)	0.010 (0.003)	0.009 (0.003)	0.013 (0.004)	0.011 (0.004)	–	–	0.017 (0.004)	0.018 (0.004)	0.019 (0.004)
MoO_3	–	–	–	–	–	–	–	–	–	–	–	–
NiO	–	–	–	–	–	–	–	–	–	0.011 (0.004)	0.010 (0.005)	0.013 (0.004)
ZnO	0.798 (0.026)	0.684 (0.021)	0.424 (0.024)	0.766 (0.022)	0.761 (0.029)	0.799 (0.027)	0.707 (0.012)	0.725 (0.030)	0.751 (0.034)	0.604 (0.018)	0.598 (0.012)	0.588 (0.021)

Table 2 (*continued*)

Run #	116	118	120	121	122	124	126	127	128	129	130	131
EPMA (wt%)	$N = 40$[a]	$N = 25$	$N = 40$	$N = 26$	$N = 20$	$N = 64$	$N = 40$	$N = 40$	$N = 45$	$N = 48$	$N = 45$	$N = 45$
TiO_2	0.144 (0.008)	0.105 (0.006)	0.130 (0.007)	0.141 (0.010)	0.123 (0.015)	0.148 (0.012)	2.006 (0.032)	2.061 (0.037)	2.071 (0.019)	0.162 (0.010)	0.173 (0.008)	0.094 (0.006)
Ta_2O_5	1.017 (0.065)	0.569 (0.047)	0.775 (0.098)	0.916 (0.064)	0.697 (0.073)	1.088 (0.095)	1.664 (0.036)	1.652 (0.060)	1.655 (0.045)	0.848 (0.069)	0.884 (0.051)	0.580 (0.051)
V_2O_3	0.969 (0.027)	0.853 (0.032)	0.576 (0.064)	0.927 (0.042)	0.852 (0.054)	1.032 (0.072)	0.872 (0.017)	0.980 (0.033)	1.016 (0.015)	0.704 (0.027)	0.674 (0.028)	0.573 (0.067)
WO_3	–	–	–	–	–	–	–	–	–	–	–	–
Cr_2O_3	0.897 (0.023)	0.807 (0.025)	0.442 (0.049)	0.721 (0.040)	0.640 (0.039)	1.038 (0.061)	0.734 (0.012)	0.815 (0.024)	0.846 (0.014)	0.702 (0.031)	0.671 (0.025)	0.760 (0.037)
Total[c]	97.28	96.61	98.64	97.31	97.00	97.61	97.77	98.163	97.13	98.88	98.52	95.76
LA–ICPMS (ppm)												
P 31	459 (11)	387 (10)	–	426 (31)	375 (18)	567 (41)	121 (2)	140 (50)	145 (8)	631 (23)	509 (27)	488 (31)
Ti 47	862 (16)	625 (53)	–	828 (59)	762 (12)	900 (11)	12,230 (78)	11,953 (326)	11,666 (302)	912 (36)	1019 (11)	632 (34)
V 51	6533 (222)	6004 (294)	–	6384 (277)	5889 (275)	6849 (263)	6088 (95)	6792 (255)	7146 (138)	4975 (306)	5094 (143)	4074 (199)
Cr 52	5886 (166)	5336 (274)	–	4877 (288)	4221 (287)	7027 (274)	4927 (72)	5522 (231)	5856 (139)	4732 (341)	4396 (98)	5084 (172)
Mn 55	10,607 (168)	9402 (421)	–	–	9772 (466)	10,998 (239)	8974 (69)	9936 (370)	8911 (198)	9183 (449)	9407 (326)	9312 (326)
Co 59	72 (2)	69 (3)	–	80 (3)	62 (3)	101 (4)	86 (2)	63 (4)	52 (2)	101 (4)	115 (8)	156 (6)
Ni 60	4 (0.2)	–	–	5 (1)	5.5 (0.5)	85 (7)	55 (2)	33 (4)	34 (3)	104 (4)	134 (10)	127 (6)
Zn 66	7070 (140)	5990 (435)	–	6171 (614)	6394 (494)	6574 (258)	6040 (101)	6283 (245)	6541 (236)	5177 (249)	5519 (219)	5402 (327)
Ga 69	5860 (138)	5725 (330)	–	5207 (569)	4813 (205)	5652 (161)	5287 (78)	6450 (623)	5890 (190)	6363 (189)	5488 (41)	6599 (153)
Ge 72	57 (2)	56 (4)	–	77 (4)	84 (4)	55 (4)	49 (2)	29 (3)	22 (2)	117 (9)	173 (21)	158 (2)
As 75	0.6 (0.1)	–	–	–	1.6 (0.2)	2 (1)	0.4 (0.08)	–	–	1.75 (0.1)	3 (0.5)	2.2 (0.3)
Nb 93	8659 (260)	5606 (457)	–	7937 (914)	6356 (362)	9632 (227)	8492 (155)	8908 (96)	8989 (210)	8027 (317)	8163 (93)	6573 (275)
Mo 95	1 (0.05)	1.3 (0.1)	–	1.5 (0.5)	2.5 (1)	3 (1)	1.2 (0.05)	1.1 (0.5)	1 (1)	3 (1)	4 (0.5)	5 (0.1)
Ta 181	10,041 (166)	5780 (227)	–	7490 (1145)	6446 (283)	9576 (123)	14,057 (107)	14,472 (439)	13,774 (347)	7416 (291)	7773 (149)	6912 (206)
W 182	25 (0.5)	33 (2)	–	–	–	60 (4)	13 (0.3)	10 (0.5)	9 (0.5)	71 (6)	58 (3)	67 (11)

Run #	132	133	134	135	139	140	141	142	143	144	145	MA17
EPMA (wt%)	$N = 45$[a]	$N = 15$	$N = 46$	$N = 13$	$N = 24$	$N = 30$	$N = 34$	$N = 35$	$N = 32$	$N = 30$	$N = 14$	$N = 15$
MgO	39.73 (1.93)[b]	37.66 (0.43)	28.04 (1.00)	39.27 (1.65)	37.73 (2.09)	34.37 (1.56)	38.12 (2.01)	34.91 (1.77)	17.7 (0.11)	26.85 (0.64)	34.76 (1.74)	33.56 (0.58)
SiO_2	40.01 (0.99)	44.81 (0.54)	39.41 (0.39)	48.51 (0.72)	41.28 (0.42)	34.48 (0.36)	33.37 (0.74)	31.70 (1.27)	46.83 (0.26)	45.24 (0.37)	34.76 (0.74)	37.03 (0.44)
Al_2O_3	1.90 (0.22)	2.07 (0.07)	9.23 (0.36)	1.96 (0.24)	2.69 (0.27)	7.97 (0.48)	7.25 (0.57)	6.15 (0.59)	7.69 (0.05)	4.95 (0.15)	7.21 (0.59)	7.92 (0.22)
CaO	2.05 (0.33)	1.33 (0.08)	8.12 (0.46)	2.83 (0.31)	2.09 (0.22)	7.55 (0.64)	7.16 (0.54)	6.24 (0.35)	6.61 (0.03)	3.98 (0.18)	6.04 (0.47)	7.23 (0.36)
Na_2O	0.36 (0.05)	0.28 (0.02)	1.78 (0.17)	0.25 (0.02)	0.31 (0.04)	1.32 (0.21)	1.23 (0.15)	0.98 (0.08)	1.26 (0.04)	0.78 (0.05)	1.13 (0.11)	1.10 (0.05)
K_2O	0.07 (0.04)	0.08 (0.01)	0.35 (0.03)	0.05 (0.006)	0.10 (0.02)	0.33 (0.04)	0.31 (0.04)	0.25 (0.02)	0.31 (0.01)	0.18 (0.01)	0.24 (0.03)	0.22 (0.01)
FeO	6.39 (0.38)	6.87 (0.25)	4.19 (0.3)	1.90 (0.11)	8.43 (0.64)	7.05 (0.42)	6.36 (0.39)	10.50 (0.69)	10.00 (0.19)	9.40 (0.23)	9.49 (0.45)	5.77 (0.30)
Ga_2O_3	0.366 (0.043)	0.413 (0.011)	0.224 (0.012)	0.099 (0.011)	0.093 (0.009)	0.094 (0.009)	0.081 (0.006)	0.129 (0.018)	0.513 (0.013)	0.537 (0.017)	0.071 (0.012)	0.110 (0.008)

MnO	0.902 (0.079)	1.179 (0.016)	0.955 (0.038)	0.913 (0.057)	1.236 (0.085)	0.864 (0.041)	0.756 (0.038)	0.640 (0.018)	1.210 (0.012)	1.214 (0.014)	0.852 (0.034)	0.688 (0.020)
GeO_2	–	–	–	–	–	–	–	–	–	–	–	–
P_2O_5	0.088 (0.012)	0.083 (0.003)	0.041 (0.011)	–	0.011 (0.002)	0.059 (0.007)	0.065 (0.006)	0.325 (0.037)	0.052 (0.004)	0.089 (0.005)	0.12 (0.014)	0.007 (0.002)
As_2O_5	–	–	–	–	–	–	–	–	–	–	–	–
Nb_2O_5	0.794 (0.101)	1.014 (0.060)	0.905 (0.072)	0.403 (0.062)	1.463 (0.162)	1.013 (0.121)	0.935 (0.100)	0.740 (0.032)	1.099 (0.028)	1.194 (0.039)	0.804 (0.071)	0.796 (0.038)
SO_3	0.021 (0.005)	–	0.013 (0.004)	0.010 (0.003)	–	–	–	0.013 (0.004)	–	–	–	0.026 (0.005)
CoO	0.016 (0.004)	0.012 (0.004)	–	–	0.012 (0.004)	–	–	0.018 (0.003)	0.014 (0.003)	0.015 (0.003)	0.012 (0.002)	0.011 (0.004)
MoO_3	–	–	–	–	–	–	–	–	–	–	–	–
NiO	0.009 (0.004)	0.009 (0.002)	–	–	–	–	–	–	–	–	–	–
ZnO	0.445 (0.027)	0.637 (0.011)	0.449 (0.031)	0.535 (0.055)	0.421 (0.031)	0.34 (0.015)	0.248 (0.016)	0.223 (0.011)	0.676 (0.013)	0.660 (0.017)	0.308 (0.026)	0.288 (0.012)
TiO_2	0.080 (0.009)	0.162 (0.005)	2.156 (0.092)	0.117 (0.013)	0.193 (0.022)	1.947 (0.162)	1.693 (0.140)	1.847 (0.080)	1.760 (0.024)	0.995 (0.022)	1.749 (0.175)	1.866 (0.040)
Ta_2O_5	0.775 (0.062)	0.776 (0.057)	1.402 (0.052)	0.665 (0.075)	1.237 (0.136)	1.434 (0.154)	1.353 (0.110)	1.12 (0.059)	1.228 (0.039)	1.044 (0.035)	1.130 (0.162)	1.367 (0.066)
V_2O_3	0.283 (0.068)	0.914 (0.022)	0.503 (0.020)	0.331 (0.022)	0.996 (0.081)	0.759 (0.050)	0.557 (0.040)	0.683 (0.049)	1.015 (0.024)	0.977 (0.048)	1.043 (0.108)	0.509 (0.009)
WO_3	–	–	–	–	–	0.012 (0.008)	0.028 (0.010)	0.141 (0.045)	–	–	0.066 (0.006)	–
Cr_2O_3	0.550 (0.042)	0.748 (0.027)	0.383 (0.016)	0.330 (0.025)	0.978 (0.083)	0.639 (0.052)	0.439 (0.029)	0.373 (0.040)	0.774 (0.030)	0.776 (0.031)	0.738 (0.053)	0.425 (0.013)
Total[c]	94.84	99.05	98.19	98.29	99.29	100.28	100.00	97.21	98.78	98.90	100.55	98.90

LA–ICPMS (ppm)

P 31	367 (24)	–	183 (11)	38 (4)	137 (7)	288 (21)	299 (13)	1018 (59)	246 (3)	366 (19)	434 (35)	–
Ti 47	497 (19)	–	11,903 (396)	691 (23)	1058 (31)	10,864 (323)	10,191 (392)	10,573 (212)	10,133 (144)	5327 (136)	10,095 (237)	10,953 (161)
V 51	2195 (258)	–	3547 (160)	2423 (21)	7067 (208)	5474 (247)	3769 (177)	4232 (127)	7049 (299)	6931 (230)	6892 (146)	3612 (110)
Cr 52	3693 (170)	–	2475 (150)	2315 (107)	6593 (82)	4242 (147)	2886 (189)	2427 (150)	5147 (206)	5372 (192)	4876 (269)	2955 (122)
Mn 55	6477 (377)	–	7336 (226)	7787 (293)	9118 (251)	6487 (115)	5862 (138)	4675 (184)	9078 (66)	9214 (196)		5211 (126)
Co 59	125 (6)	–	48 (2)	17 (1)	81 (5)	52 (2)	36 (3)	64 (4)	76 (5)	80 (4)	33 (1.5)	92 (5)
Ni 60	116 (6)	–	30 (2)	28 (3)	74 (4)	38 (2)	56 (4)	79 (4)	67 (5)	60 (4)	26 (1)	78 (2)
Zn 66	4033 (152)	–	4709 (633)	4263 (210)	3485 (282)	3191 (96)	2269 (153)	2611 (115)	5939 (260)	5412 (257)	2340 (179)	2219 (118)
Ga 69	–	–	–	–	–	–	–	–	–	–	–	–
Ge 72	161 (12)	–	61 (4)	24 (3)	15 (1)	9 (0.3)	11 (1)	32 (4)	43 (4)	45 (2)	16 (1)	9 (1)
As 75	2 (0.2)	–	2 (1)	–	0.75 (0.02)	0.7 (0.1)	–	2 (0.2)	–	–	0.75 (0.2)	1.5 (0.2)
Nb 93	5285 (215)	–	6601 (162)	3015 (110)	11,093 (616)	7009 (143)	6444 (177)	5317 (162)	8240 (206)	8621 (146)	5925 (284)	5836 (211)
Mo 95	9 (4)	–	1.25 (0.2)	0.3 (0.02)	6 (0.5)	12 (0.7)	12 (1)	75 (1.5)	1.75 (1)	1.5 (0.1)	11.5 (0.7)	18 (2)
Ta 181	5912 (115)	–	11,748 (428)	5394 (239)	11,268 (189)	11,467 (276)	10,486 (339)	8463 (146)	10,027 (218)	9430 (245)	9161 (237)	10,974 (288)
W 182	68 (3)	–	–	5 (1)	–	108 (9)	135 (38)	272 (44)	23 (3)	31 (3)	311 (15)	–

Table 2 (*continued*)

Run #	MA18	MA20	MA21	MA22
EPMA	$N = 40$[a]	$N = 14$	$N = 37$	$N = 18$
(wt%)				
MgO	35.82 (0.76)[b]	41.84 (2.27)	31.18 (0.42)	31.03 (0.48)
SiO_2	36.42 (0.41)	31.49 (1.29)	37.27 (0.53)	38.54 (0.60)
Al_2O_3	7.06 (0.31)	6.04 (0.65)	8.08 (0.13)	7.89 (0.17)
CaO	7.40 (0.32)	6.80 (0.81)	7.38 (0.18)	7.51 (0.29)
Na_2O	1.01 (0.06)	1.18 (0.19)	1.27 (0.04)	1.25 (0.06)
K_2O	0.19 (0.01)	0.32 (0.04)	0.24 (0.01)	0.20 (0.01)
FeO	5.91 (0.25)	6.52 (0.45)	7.96 (0.22)	7.31 (0.28)
Ga_2O_3	0.095 (0.007)	0.071 (0.009)	0.161 (0.010)	0.223 (0.009)
MnO	0.666 (0.025)	0.505 (0.015)	0.780 (0.010)	0.765 (0.028)
GeO_2	–	–	–	–
P_2O_5	0.004 (0.002)	0.021 (0.001)	0.005 (0.001)	0.005 (0.001)
As_2O_5	–	–	–	–
Nb_2O_5	0.882 (0.042)	0.716 (0.062)	0.754 (0.032)	0.714 (0.028)
SO_3	0.023 (0.004)	0.017 (0.003)	0.008 (0.003)	0.009 (0.003)
CoO	–	0.024 (0.006)	0.016 (0.004)	0.19 (0.003)
MoO_3	–	–	–	–
NiO	–	–	0.018 (0.004)	0.020 (0.004)
ZnO	0.253 (0.014)	0.410 (0.049)	0.385 (0.013)	0.330 (0.011)
TiO_2	1.919 (0.051)	1.456 (0.099)	1.908 (0.038)	1.889 (0.035)
Ta_2O_5	1.380 (0.077)	1.147 (0.109)	1.074 (0.056)	1.121 (0.049)
V_2O_3	0.418 (0.011)	0.406 (0.055)	0.614 (0.008)	0.647 (0.011)
WO_3	–	–	–	–
Cr_2O_3	0.335 (0.011)	0.328 (0.041)	0.509 (0.011)	0.490 (0.012)
Total[c]	99.82	99.32	99.64	100.16
LA–ICPMS (ppm)				
P 31	–	–	–	–
Ti 47	11,137 (276)	9032 (320)	11,006 (200)	11,098 (177)
V 51	2815 (128)	2916 (228)	4266 (199)	4445 (171)
Cr 52	2253 (104)	2144 (253)	3399 (188)	3288 (116)
Mn 55	4974 (128)	4220 (205)	5992 (223)	5816 (177)
Co 59	61 (3)	67 (4)	138 (3)	143 (3)
Ni 60	95 (4)	83 (7)	143 (4)	168 (6)
Zn 66	2088 (72)	3576 (178)	3025 (128)	2908 (68)
Ga 69	–	–	–	–
Ge 72	9 (1)	13 (2)	16 (1)	16 (1.5)
As 75	2.5 (0.3)	1 (0.2)	3 (0.1)	3 (0.2)
Nb 93	6308 (262)	5281 (375)	5328 (211)	5083 (180)
Mo 95	27 (3)	26 (2)	48 (3)	32 (2)
Ta 181	11,632 (363)	9155 (434)	9017 (297)	9211 (210)
W 182	128 (5)	61 (7)	148 (3)	170 (6)

[a] Number of analyses.
[b] Values in parentheses are errors given as two standard deviations for EPMA and one for LA-ICPMS.
[c] Totals also include traces of elements that concentrations are not reported (Te, Sb).

Table 3
Average major and trace element compositions of the metallic melts determined by EPMA and LA-ICPMS analyses.

Run #	50	51	52	85	93	94	95	96	97	101	102	103
EPMA (wt%)	$N = 30$[a]	$N = 22$	$N = 18$	$N = 8$	$N = 11$	$N = 12$	$N = 8$	$N = 10$	$N = 6$	$N = 13$	$N = 52$	$N = 16$
Fe	73.080 (0.748)[b]	73.458 (0.630)	75.022 (0.730)	71.910 (0.283)	79.353 (0.175)	79.353 (0.844)	80.957 (0.650)	83.186 (1.279)	82.890 (0.883)	78.146 (0.988)	75.77 (1.100)	77.82 (0.995)
Ga	0.469 (0.016)	0.510 (0.020)	1.910 (0.04)	1.367 (0.123)	0.748 (0.063)	0.643 (0.023)	0.592 (0.029)	0.321 (0.081)	0.661 (0.092)	0.979 (0.023)	1.180 (0.050)	1.066 (0.058)
Mn	–	–	–	0.033 (0.007)	–	–	–	–	–	–	0.025 (0.003)	0.053 (0.006)
Ge	2.300 (0.076)	2.232 (0.040)	2.711 (0.055)	2.265 (0.172)	3.372 (0.117)	3.051 (0.157)	2.650 (0.070)	2.413 (0.596)	2.690 (0.365)	2.049 (0.034)	2.050 (0.050)	1.779 (0.148)
P	0.009 (0.002)	0.009 (0.001)	0.035 (0.003)	0.151 (0.035)	0.378 (0.053)	0.234 (0.014)	0.134 (0.015)	0.034 (0.006)	0.211 (0.028)	0.716 (0.057)	0.546 (0.018)	0.321 (0.023)
As	–	–	–	2.196 (0.331)	0.083 (0.019)	0.051 (0.013)	0.042 (0.015)	0.033 (0.009)	0.039 (0.009)	0.026 (0.005)	0.022 (0.007)	–
Nb	–	–	–	–	–	–	–	–	–	0.011 (0.003)	0.019 (0.002)	0.011 (0.004)
S	0.064 (0.004)	0.065 (0.004)	0.085 (0.007)	0.066 (0.003)	0.062 (0.004)	0.050 (0.003)	0.047 (0.002)	0.101 (0.024)	0.040 (0.004)	0.058 (0.003)	0.058 (0.003)	0.051 (0.004)
Co	3.346 (0.060)	3.224 (0.051)	3.433 (0.040)	3.368 (0.131)	1.122 (0.015)	1.202 (0.026)	1.107 (0.026)	1.193 (0.046)	1.149 (0.030)	0.782 (0.018)	0.825 (0.024)	0.662 (0.020)
Mo	3.094 (0.092)	2.770 (0.060)	3.120 (0.081)	3.173 (0.245)	2.271 (0.085)	1.967 (0.072)	1.657 (0.082)	2.047 (0.161)	1.881 (0.104)	2.603 (0.079)	2.851 (0.155)	2.971 (0.178)
Ni	7.613 (0.153)	7.458 (0.100)	8.500 (0.092)	7.052 (0.372)	5.452 (0.122)	5.766 (0.144)	5.037 (0.201)	5.147 (0.462)	5.424 (0.514)	7.195 (0.214)	7.530 (0.152)	6.859 (0.207)
Zn	–	–	–	–	–	–	–	–	–	–	–	–
Ta	–	–	–	–	–	–	–	–	–	–	–	–
V	–	–	–	0.159 (0.006)	0.218 (0.006)	0.149 (0.010)	0.236 (0.014)	0.095 (0.009)	0.210 (0.014)	0.132 (0.015)	0.305 (0.033)	0.399 (0.012)
W	2.333 (0.058)	2.400 (0.072)	2.106 (0.063)	3.867 (0.275)	1.074 (0.029)	1.062 (0.044)	1.002 (0.015)	1.163 (0.037)	1.043 (0.069)	2.429 (0.287)	3.020 (0.452)	2.492 (0.106)
Cr	0.143 (0.015)	0.161 (0.005)	–	0.492 (0.092)	0.258 (0.015)	0.262 (0.044)	0.293 (0.021)	0.156 (0.017)	0.498 (0.029)	0.238 (0.017)	0.470 (0.061)	0.768 (0.030)
Si	–	–	0.023 (0.003)	–	0.024 (0.011)	0.166 (0.023)	0.333 (0.055)	0.037 (0.013)	0.334 (0.187)	0.023 (0.025)	0.039 (0.044)	0.010 (0.006)
Total[c]	92.45	92.29	96.94	96.01	94.46	94.03	94.28	96.74	97.11	95.30	94.89	95.42
C (wt%)[d]	6.77	6.77	–	7.75	7.43	7.21	7.65	7.85	8.05	6.47	7.43	7.85
LA–ICPMS (ppm)												
Ti 47	–	–	–	–	–	12 (5)	–	–	6 (3)	–	–	–
V 51	–	140 (25)	–	–	–	1553 (67)	–	1010 (34)	2011 (29)	1183 (111)	–	–
Cr 52	1487 (55)	1622 (48)	–	–	–	2686 (34)	2733 (78)	1680 (89)	4874 (56)	2416 (88)	–	–
Mn 55	75 (2)	70 (2)	154 (3)	–	107 (5)	62 (7)	120 (11)	67 (2)	131 (5)	42 (2)	–	–
Zn 66	–	–	–	–	–	16 (1.5)	–	21 (1)	30 (2)	–	–	–

Table 3 (*continued*)

Run #	50	51	52	85	93	94	95	96	97	101	102	103
EPMA (wt%)	$N = 30$[a]	$N = 22$	$N = 18$	$N = 8$	$N = 11$	$N = 12$	$N = 8$	$N = 10$	$N = 6$	$N = 13$	$N = 52$	$N = 16$
Nb 93	–	–	31 (1)	–	–	19 (1)	–	15 (4)	51 (2)	106 (5)	–	–
Ta 181	–	–	–	–	–	9 (3)	–	11 (3)	6 (2)	–	–	–

Run #	116	118	120	121	122	124	126	127	128	129	130	131
EPMA (wt%)	$N = 29$[a]	$N = 10$	$N = 20$	$N = 24$	$N = 22$	$N = 35$	$N = 35$	$N = 40$	$N = 35$	$N = 18$	$N = 25$	$N = 20$
Fe	81.946 (0.928)[b]	82.661 (0.996)	84.498 (0.339)	83.36 (0.800)	83.184 (0.748)	78.409 (0.890)	80.35 (0.743)	79.006 (1.011)	80.102 (0.908)	81.225 (0.272)	79.762 (0.404)	80.585 (0.361)
Ga	1.986 (0.046)	1.999 (0.099)	1.780 (0.085)	2.065 (0.076)	2.100 (0.057)	1.429 (0.049)	1.525 (0.041)	1.412 (0.043)	1.334 (0.030)	1.932 (0.084)	1.887 (0.092)	1.754 (0.029)
Mn	0.018 (0.007)	0.021 (0.005)	0.065 (0.004)	0.043 (0.010)	0.058 (0.006)	0.018 (0.004)	0.011 (0.004)	–	–	0.044 (0.003)	0.066 (0.008)	0.071 (0.010)
Ge	1.350 (0.103)	1.259 (0.098)	1.353 (0.047)	1.278 (0.044)	1.223 (0.031)	1.113 (0.051)	1.036 (0.033)	0.995 (0.032)	1.028 (0.031)	1.162 (0.045)	1.217 (0.054)	1.257 (0.045)
P	0.654 (0.046)	0.640 (0.026)	0.668 (0.022)	0.663 (0.037)	0.700 (0.019)	0.428 (0.031)	0.734 (0.026)	0.722 (0.028)	0.681 (0.019)	0.574 (0.048)	0.626 (0.039)	0.705 (0.037)
As	1.312 (0.118)	1.234 (0.051)	1.359 (0.049)	1.135 (0.075)	1.268 (0.042)	1.084 (0.068)	1.001 (0.037)	1.010 (0.042)	0.974 (0.029)	1.167 (0.111)	1.249 (0.074)	1.247 (0.035)
Nb	–	–	–	–	–	–	–	–	–	–	–	–
S	0.039 (0.003)	0.046 (0.003)	0.040 (0.003)	0.038 (0.002)	0.038 (0.003)	0.036 (0.003)	0.050 (0.003)	0.053 (0.003)	0.053 (0.004)	0.038 (0.002)	0.038 (0.004)	0.137 (0.012)
Co	1.499 (0.036)	1.524 (0.033)	1.507 (0.029)	1.514 (0.035)	1.434 (0.025)	1.384 (0.028)	1.219 (0.023)	1.217 (0.030)	1.230 (0.026)	1.371 (0.015)	1.450 (0.021)	1.474 (0.012)
Mo	1.764 (0.118)	2.050 (0.061)	1.888 (0.096)	1.683 (0.095)	1.746 (0.025)	1.545 (0.051)	2.179 (0.039)	2.242 (0.039)	2.311 (0.174)	1.612 (0.058)	1.700 (0.066)	1.645 (0.029)
Ni	0.405 (0.025)	0.474 (0.017)	0.450 (0.014)	0.416 (0.013)	0.401 (0.011)	5.577 (0.120)	3.725 (0.070)	3.657 (0.052)	3.683 (0.119)	5.891 (0.219)	5.941 (0.107)	5.607 (0.077)
Zn	0.294 (0.012)	0.275 (0.016)	0.291 (0.009)	0.372 (0.020)	0.366 (0.013)	0.216 (0.015)	0.172 (0.010)	0.101 (0.012)	0.052 (0.010)	0.258 (0.019)	0.389 (0.012)	0.288 (0.017)
Ta	–	–	0.042 (0.006)	–	–	–	–	–	–	–	–	–
V	0.444 (0.016)	0.423 (0.010)	0.727 (0.021)	0.444 (0.026)	0.734 (0.038)	0.292 (0.011)	0.306 (0.005)	0.213 (0.004)	0.165 (0.008)	0.391 (0.009)	0.515 (0.029)	0.311 (0.008)
W	2.191 (0.084)	2.431 (0.062)	2.190 (0.080)	2.129 (0.109)	2.116 (0.067)	1.985 (0.072)	1.668 (0.065)	1.686 (0.058)	1.728 (0.145)	1.967 (0.073)	2.061 (0.082)	2.010 (0.029)
Cr	0.714 (0.019)	0.727 (0.013)	0.773 (0.033)	0.693 (0.016)	0.936 (0.006)	0.555 (0.019)	0.384 (0.012)	0.321 (0.008)	0.270 (0.009)	0.766 (0.012)	0.776 (0.018)	0.749 (0.016)
Si	–	–	–	–	–	–	–	–	–	–	–	–
Total[c]	94.62	95.76	97.63	95.83	96.30	94.10	94.36	92.38	93.45	98.40	97.70	97.84
C (wt%)[d]	7.09	7.21	7.43	7.65	7.85	7.09	7.09	6.73	6.47	8.05	8.24	8.42

LA-ICPMS (ppm)

	132	133	134	135	139	140	141	142	143	144	145	MA17
Ti 47	–	–	–	–	–	5 (2)	23 (1)	–	–	9 (3)	10 (1)	4 (0.5)
V 51	4551 (129)	4138 (114)	–	–	–	2818 (172)	2866 (51)	1887 (38)	1480 (55)	4369 (55)	4909 (92)	3395 (201)
Cr 52	6956 (170)	7190 (130)	–	–	–	5469 (102)	3829 (57)	3305 (60)	2722 (58)	7881 (159)	7785 (183)	7652 (137)
Mn 55	237 (19)	226 (14)	–	–	–	264 (8)	126 (2)	63 (3)	41 (1)	495 (20)	726 (29)	751 (30)
Zn 66	2848 (145)	2725 (160)	–	–	–	2386 (53)	1799 (104)	1082 (96)	547 (90)	2800 (125)	3863 (165)	2658 (184)
Nb 93	735 (46)		–	–	–	359 (19)	652 (8)	–	–	559 (21)	1032 (11)	1124 (83)
Ta 181	47 (6)	–	–	–	–	42 (5)	35 (2)	–	–	155 (11)	101 (12)	103 (5)
Run #	132	133	134	135	139	140	141	142	143	144	145	MA17
EPMA (wt%)	N = 25[a]	N = 25	N = 27	N = 11	N = 45	N = 45	N = 28	N = 16	N = 20	N = 20	N = 14	N = 30
Fe	80.274 (0.47)[b]	79.780 (0.501)	81.562 (0.518)	75.004 (0.176)	80.744 (0.354)	83.423 (0.243)	84.486 (0.520)	83.691 (0.470)	81.675 (0.111)	81.868 (0.096)	85.032 (0.237)	83.653 (0.205)
Ga	1.951 (0.071)	1.971 (0.064)	1.705 (0.045)	2.519 (0.027)	2.821 (0.046)	2.554 (0.038)	2.335 (0.034)	2.064 (0.055)	1.527 (0.039)	1.540 (0.044)	2.131 (0.026)	1.88 (0.047)
Mn	0.085 (0.010)	0.032 (0.004)	0.056 (0.003)	0.106 (0.009)	0.027 (0.009)	0.029 (0.006)	0.029 (0.011)	0.019 (0.010)	–	–	0.018 (0.004)	0.049 (0.006)
Ge	1.204 (0.031)	1.141 (0.028)	0.973 (0.028)	2.119 (0.032)	1.070 (0.028)	0.912 (0.027)	1.059 (0.035)	1.254 (0.020)	0.988 (0.026)	0.997 (0.023)	1.132 (0.020)	1.120 (0.035)
P	0.833 (0.042)	0.599 (0.036)	0.915 (0.039)	0.760 (0.034)	0.791 (0.063)	0.797 (0.048)	0.774 (0.021)	0.358 (0.031)	0.629 (0.020)	0.581 (0.021)	0.504 (0.054)	0.829 (0.016)
As	1.212 (0.124)	0.987 (0.061)	1.067 (0.047)	1.076 (0.046)	1.178 (0.055)	1.004 (0.047)	1.081 (0.038)	1.190 (0.077)	1.055 (0.024)	0.982 (0.026)	0.979 (0.042)	1.088 (0.027)
Nb	–	–	0.259 (0.034)	0.604 (0.021)	–	–	–	–	–	–	–	–
S	0.045 (0.002)	0.037 (0.002)	0.053 (0.003)	0.054 (0.002)	0.032 (0.002)	0.045 (0.003)	0.054 (0.004)	0.076 (0.007)	0.042 (0.002)	0.034 (0.001)	0.057 (0.006)	0.072 (0.004)
Co	1.379 (0.016)	1.426 (0.015)	1.223 (0.017)	1.091 (0.011)	1.464 (0.023)	1.289 (0.011)	1.054 (0.015)	1.239 (0.011)	1.128 (0.016)	1.107 (0.024)	1.075 (0.009)	1.332 (0.016)
Mo	1.734 (0.053)	1.384 (0.054)	2.271 (0.055)	2.622 (0.025)	1.630 (0.040)	2.388 (0.047)	2.378 (0.045)	2.825 (0.156)	1.686 (0.038)	1.644 (0.041)	2.449 (0.067)	2.493 (0.066)
Ni	5.489 (0.089)	6.233 (0.057)	3.521 (0.098)	4.546 (0.043)	6.262 (0.124)	4.071 (0.023)	4.131 (0.025)	4.578 (0.040)	4.888 (0.046)	4.945 (0.055)	4.133 (0.037)	4.010 (0.036)
Zn	0.332 (0.014)	0.332 (0.015)	0.423 (0.012)	0.695 (0.036)	0.728 (0.033)	0.542 (0.016)	0.553 (0.039)	0.312 (0.031)	0.181 (0.011)	0.192 (0.013)	0.420 (0.020)	0.438 (0.028)
Ta	–	–	–	–	–	–	–	–	–	–	–	–
V	0.461 (0.010)	0.515 (0.018)	0.603 (0.019)	0.910 (0.031)	0.113 (0.015)	0.088 (0.011)	0.064 (0.011)	0.057 (0.010)	0.221 (0.011)	0.181 (0.008)	0.070 (0.006)	0.079 (0.006)
W	2.013 (0.069)	1.800 (0.024)	1.639 (0.045)	2.580 (0.023)	1.966 (0.025)	1.660 (0.025)	1.245 (0.024)	0.935 (0.049)	1.321 (0.023)	1.300 (0.021)	1.290 (0.020)	1.755 (0.022)
Cr	1.110 (0.026)	0.501 (0.027)	0.599 (0.012)	0.981 (0.012)	0.294 (0.018)	0.172 (0.027)	0.169 (0.022)	0.099 (0.011)	0.345 (0.011)	0.318 (0.009)	0.167 (0.017)	0.220 (0.007)
Si	–	–	–	–	–	–	–	–	–	–	–	–
Total[c]	98.12	96.74	96.87	95.88	99.12	98.97	99.41	98.70	95.67	95.69	95.69	99.02
C (wt%)[d]	8.59	7.85	7.85	7.85	–	–	–	–	7.09	7.09	–	–

Table 3 (*continued*)

Run #	132	133	134	135	139	140	141	142	143	144	145	MA17
EPMA (wt%)	$N = 25$[a]	$N = 25$	$N = 27$	$N = 11$	$N = 45$	$N = 45$	$N = 28$	$N = 16$	$N = 20$	$N = 20$	$N = 14$	$N = 30$
LA-ICPMS (ppm)												
Ti 47	17 (3)	–	36 (4)	42 (6)	–	–	–	–	–	–	–	–
V 51	4863 (61)	–	6395 (119)	9457 (276)	1099 (108)	922 (56)	673 (76)	601 (56)	2387 (132)	1920 (111)	725 (44)	811 (41)
Cr 52	10,023 (210)	–	5841 (168)	9920 (143)	2876 (152)	1836 (188)	1675 (157)	1118 (66)	3344 (70)	3202 (56)	1657 (119)	2338 (51)
Mn 55	916 (29)	–	658 (25)	1096 (61)	266 (12)	278 (20)	285 (9)	171 (11)	133 (6)	128 (6)	215 (5)	496 (15)
Zn 66	3154 (38)	–	4038 (132)	6680 (256)	7203 (224)	5593 (220)	5558 (285)	2994 (202)	1667 (102)	1950 (96)	3983 (206)	4411 (223)
Nb 93	1458 (155)	–	2723 (126)	6410 (166)	179 (4)	208 (4)	175 (5)	148 (5)	–	409 (11)	228 (3)	–
Ta 181	139 (12)	–	22 (5)	–	9 (4)	16 (3)	–	–	–	30 (5)	–	–

Run #	MA18	MA20	MA21	MA22
EPMA (wt%)	$N = 100$[a]	N = 30	$N = 25$	$N = 23$
Fe	84.708 (0.170)[b]	83.111 (0.418)	83.394 (0.170)	83.277 (0.182)
Ga	2.069 (0.056)	2.094 (0.034)	1.791 (0.027)	1.772 (0.040)
Mn	0.056 (0.007)	0.027 (0.010)	0.053 (0.005)	0.058 (0.009)
Ge	1.029 (0.043)	1.123 (0.024)	1.225 (0.022)	1.191 (0.032)
P	0.804 (0.023)	0.816 (0.028)	0.805 (0.026)	0.808 (0.022)
As	1.026 (0.025)	0.863 (0.028)	0.990 (0.020)	1.010 (0.041)
Nb	–	–	–	–
S	0.074 (0.004)	0.076 (0.004)	0.067 (0.003)	0.088 (0.003)
Co	1.281 (0.017)	1.372 (0.015)	1.362 (0.008)	1.296 (0.007)
Mo	2.486 (0.035)	2.616 (0.039)	2.732 (0.042)	2.555 (0.049)
Ni	3.782 (0.034)	4.257 (0.030)	4.597 (0.019)	4.481 (0.040)
Zn	0.400 (0.015)	0.678 (0.035)	0.382 (0.022)	0.405 (0.022)
Ta	–	–	–	–
V	0.094 (0.006)	0.072 (0.015)	0.064 (0.004)	0.061 (0.008)
W	1.739 (0.028)	1.787 (0.025)	1.868 (0.037)	1.796 (0.036)
Cr	0.234 (0.005)	0.201 (0.023)	0.218 (0.009)	0.236 (0.011)
Si	–	–	–	–
Total[c]	99.78	99.09	99.55	99.03
C (wt%)[d]	–	–	–	–
LA-ICPMS (ppm)				
Ti 47	–	–	–	–
V 51	953 (84)	769 (34)	666 (35)	631 (50)
Cr 52	2312 (43)	2175 (165)	2263 (39)	2436 (42)
Mn 55	548 (8)	295 (9)	541 (10)	592 (10)
Zn 66	4051 (131)	6625 (302)	3905 (180)	3944 (201)
Nb 93	64 (4)	101 (3)	44 (6)	–
Ta 181	18 (4)	36 (5)	22 (4)	–

[a] Number of analyses.
[b] Values in parentheses are errors given as two standard deviations for EPMA and one for LA-ICPMS.
[c] Totals also include traces of elements that concentrations are not reported (Te, Se, Sb).
[d] Calculated carbon solubility at run conditions (See text for details).

(high *nbo/t*) that quenched to a heterogeneous texture of small olivine quench crystals and interstitial glass as can be seen in Fig. 2b. Quenched metallic liquids exhibit a more subtle quench texture, only visible at high contrast, comprising dendrites of Fe-rich alloys (Fig. 2e). Most of the experiments performed using graphite capsules produced Fe–Ni–C alloys (iron dendrites surrounded by C-rich interstitial phase) saturated with graphite.

3. ANALYTICAL METHODS

Metal and silicate phases of the samples were first analyzed using the JEOL JXA-8200 electron probe micro-analyzer (EPMA) at LLNL. X-ray intensities were reduced using the CITZAF correction routine (Armstrong, 1995). Operating conditions were 15 kV accelerating voltage, 10 nA beam current and counting times of 10–20 s on peak and background for major elements in silicate (Si, Mg, Fe, Al, Ca, Na, K). For trace elements in both metal and silicate, analyses were collected with 20 kV accelerating voltage, 100 nA beam current and counting times up to 50–100 s on peak and background giving detection limits (i.e. peak counts approximately three sigma over the background counts) between 100 and 300 ppm for most elements except W, Nb and Ta which were more likely detected above 300 ppm. Diopside glass (Si), wollastonite (Ca), orthoclase (K), anorthite (Al), albite (Na) and pure oxides (Fe_2O_3, MgO, SiO_2, CaO and Al_2O_3) were used as standards for the major elements. Pure metals were used as standards for the trace elements except gallium arsenide for Ga and As, apatite for P, pyrite for S, rutile for Ti and spessartine for Mn in silicate melt. Care was taken to correct for line interferences in the samples containing a large number of trace elements when peak interferences could not be resolved by the instrument resolution. Measurements of the intensity of the overlapping lines in standards that did not contain the element of interest were used to correct the data measured on the unknown specimens. Due to the quench textures, analyses with a defocused beam (40–80 μm for silicate melt; 20–40 μm for metallic melt) were used to determine the bulk compositions. Exsolution features in the metallic phases, with significant concentrations of V, Cr, Mn, as previously described (O'Neill et al., 1998), were observed occasionally in our samples. Nucleation processes combined with diffusion during quench explain the presence of such exsolution blobs in the center of metallic phases with blob-free border zone (>50 μm large) along the boundary with the silicate. Therefore, only analyses from the central regions of large-sized metallic phases were considered reliable for measuring partition coefficients representative of the composition at run conditions.

The carbon content of the metal liquid was not directly measured in this study (work in progress using a nuclear microprobe, CEA, France) due to difficulty in quantitatively measuring C with the electron probe (surface contamination, X-ray absorption, C-coat on the samples and reliable standard issues) and in resolving the proportion of exsolved carbon reflecting graphite saturation and solubility at run conditions versus that exsolved on quench.

The expected carbon content at run conditions was then calculated on thermodynamic grounds as detailed below.

LA-ICPMS measurements were performed at LLNL and at the University of California Davis (UCD). Ablation was conducted using a deep UV (213 nm) Nd:YAG New wave Research UP-213 laser system operated at 10 Hz for the laser frequency and 6–10 J/cm^2 for the energy density. A 60-μm beam size was employed for averaging the compositions of both metal and silicate phases with fine-grained quench textures. Helium gas was flushed into the ablation cell minimizing aerosol deposition around the ablation pit and improving transport efficiency. Laser-induced aerosol particles were carried by helium and then mixed with argon before entering the plasma. The laser system was coupled to a quadrupole ICP mass spectrometer (Agilent 7500ce (UCD); X series (LLNL)). Both mass spectrometers use collision reaction cell technology to remove polyatomic interferences. RF power was set around 1400 W and coolant gas to 13 L/min. Dwell time was set between 10 and 50 ms for all isotopes depending on their expected abundances in metal or silicate phases. The following isotopes were monitored: ^{31}P, ^{43,44}Ca, ^{46,47}Ti, ^{51}V, ^{52,53}Cr, ^{55}Mn, ^{59}Co, ^{60}Ni, ^{66,68}Zn, ^{69}Ga, ^{72}Ge, ^{75}As, ^{93}Nb, ^{95,97}Mo, ^{181}Ta and ^{182}W. Each spot analysis consisted of 30 s background measurement (gas blank) followed by 30–60 s laser firing time. The ablation cell was flushed for 2 min (no ablation) between analyses to reduce memory effects. The trace element doped glass reference NIST 610 was used as calibration standard for both silicate and metal phases. Five measurements on NIST 610 were performed after every unknown analyzed sample to monitor instrumental drift. Concentrations of Ca in silicate and Co in metal measured by EPMA (JEOL JXA-8200) were used as internal standards to correct for variations in ablation yields between samples and reference material. Finally the accuracy of the calibration was assessed by routinely analyzing the fused basalt glass reference from the USGS, BCR-2G and BHVO-2G for silicate phases and an in house standard sample #124 for metal phases. Comparison with EPMA data obtained on metal phase of #124 was only possible for elements detectable by electron probe measurement, i.e. hundreds of ppm. Ti, Ta and Nb metal contents in #124 being below EPMA detection limits, the accuracy of the LA-ICPMS measurements for these elements could not be tested. The measured standard concentrations for most the elements lie within ±10% of the published values for BCR-2G, BHVO-2G and EPMA measurements on #124 (see Appendix B). Ga abundances were systematically overestimated by more than 25% compare to standards and EPMA measurements of the samples and were then not considered as reliable (see Appendix B). Thus, we only considered data obtained by EPMA for Ga. Data reduction including corrections for down-hole loss of intensity, instrumental drift, and recalculation of concentration data relative to predetermined internal standards was carried out using GLITTER and Thermo PlasmaLab softwares (Van Achterbergh et al., 2001). Minimum detection limits (at the 99% confidence level) were determined from Poisson counting statistics and are based on the total counts for each element during the background measurement. Tables 2 and 3 report the compositions of silicate and metallic melts.

4. RESULTS

4.1. Major element composition

The melt compositions in runs using KLB1 are perido-titic with ~40 wt% SiO$_2$ and MgO (Table 2). As expected, experiments in MgO capsules using tholeiitic basalt in the starting mixtures are affected by some MgO dissolution. The silicate melts in these runs contain MgO in excess of 30 wt% relative to ~8 wt% for runs performed in graphite containers. The metallic phases from the various runs contain ~71–85 wt% Fe (Table 3). Any systematic variation with temperature and pressure is masked by the variation in minor and trace element concentrations. Oxygen was not analyzed in these experiments due to its high detection limit and the low contents of oxygen in metal expected at the run conditions. Indeed, considering recent oxygen partitioning data between magnesiowüstite and iron liquid (Asahara et al., 2007), oxygen solubility should not exceed 1 wt% for the highest T run of this work. Low analytic totals, between 92 and 98 wt%, for metal when using graphite containers are explained by the presence of significant amounts of dissolved carbon, which was not measured. The analytical totals for metal in experiments run in MgO capsules are much closer to 100% (Table 3).

4.2. Carbon solubility in liquid iron

Carbon was not measured by electron microprobe based on a number of analytical issues discussed above. We modified the approach adopted by Wood (1993) to calculate the solubility of carbon in liquid iron at high pressures. Graphite was taken as the reference state and was assigned a free energy of 0 J mol^{-1} at 1 bar and all temperatures. The standard state free energy of C in Fe liquid was estimated from 1 atm solubility measurements (e.g. Chipman, 1972). The following polynomial expression was derived as a function of temperature (in K):

$$G^0 = 4533 + 16.11\,T + 1.74 \times 10^{-2}\,T^2 - 6.56$$
$$\times 10^{-6}\,T^3 \;(\text{J mol}^{-1}) \tag{1}$$

This relation approximates the 2-regime relationships used by Wood (1993). Third-order Birch–Murnaghan equations of state for graphite and liquid carbide were used to calculate the volume change with pressure. The derived pressure

Table 4
Equations of state properties used for modeling carbon solubility in liquid iron to 5 GPa.

Phase	V^0 (cm^3/mol)	α(T)	K (GPa)	K'
Graphite	5.3[a]	2.85×10^{-5}[b]	33.8[c]	8.9[c]
Carbon in liquid Fe	5.6[d]	$\alpha_{C–Fe}$ (T)[d]	442[e]	4[e]

$\alpha_{C–Fe}\,(T) = -7.85 \times 10^{-4} + 5.64 \times 10^{-7}\,T - 2.23 \times 10^{-10}\,T^2$.
All data refer to 298 K or 1 atm.
[a] Ref. Robie et al. (1978).
[b] Ref. Skinner (1966).
[c] Ref. Hanfland et al. (1989).
[d] This study.
[e] Ref. McSkimin and Andreatch (1972).
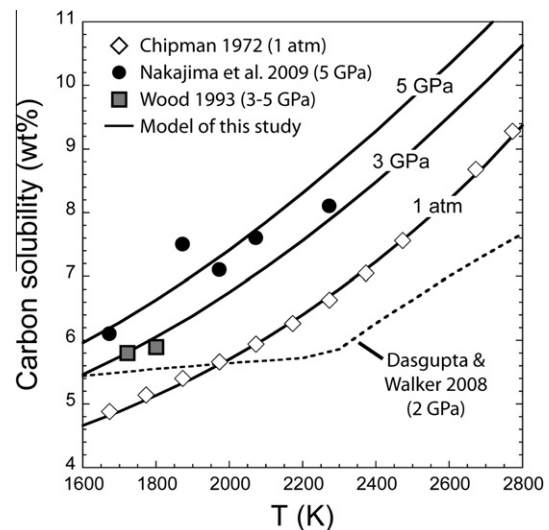
Fig. 3. Modeled carbon solubility curves as a function of pressure and temperature (see text for details). Note the good agreement with experimental data from Nakajima et al. (2009) at 5 GPa and Wood (1993) at 3 GPa. However, the data from Dasgupta and Walker (2008) and Wood (1993) at 5 GPa and 1800 K do not fit the model.

terms were then used to calculate the free energies of graphite and C in Fe liquid and C solubility at the pressure of interest (to 5 GPa). Equations of state properties are listed in Table 4. The partial molar volume of C and its thermal expansion in liquid Fe were derived from the density measurements of Ogino et al. (1984) and Jimbo and Cramb (1993) for C-rich iron carbides. Interestingly, the partial thermal expansion of C is a negative function of temperature. This is a consequence of the fact that the partial molar volume of Fe increases more rapidly than the molar volume of the carbide. Note that Wood (1993) assigned the bulk thermal expansion of the carbide to C. Carbide density measurements also indicate that the partial molar volume of C in liquid Fe is close to that of diamond at high temperatures. Given this similarity, we assumed that the compressibility of carbon in liquid iron is comparable to that of diamond ($K = 442$ GPa and $K' = 4$, from McSkimin and Andreatch (1972)). Wood (1993) made the same assumption in absence of relevant compressibility data, although he used slightly different values for diamond compressibility. Fig. 3 illustrates carbon solubility curves calculated as a function of pressure and temperature. Experimentally measured solubility data from the literature are also shown for comparison. The modeled solubility curves calibrated on 1 atm data from Chipman (1972) are consistent with measurements of Wood (1993) and Nakajima et al. (2009). However, there is a large discrepancy with the solubility measurements of Dasgupta and Walker (2008), which may indicate that these authors did not take account of some graphite exsolved from Fe liquid upon quenching.

4.3. Metal–silicate partitioning

We report results from 40 experiments constraining the partitioning behavior between liquid metal and liquid silicate of 14 elements normally regarded as moderately siderophile (Mo, As, Ge, W, P, Ni, Co), slightly siderophile (Zn, Ga,

Mn, V, Cr) and refractory lithophile (Nb, Ta). The effects of temperature (T), pressure (P), silicate melt composition and oxygen fugacity (fO_2) on partitioning were investigated separately (sets of isobaric and isothermal experiments). The basic reaction that describes the distribution of an element M between a metal phase and a silicate liquid is:
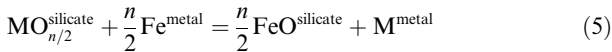
$$M^{metal} + \frac{n}{4}O_2 = MO_{n/2}^{silicate} \qquad (2)$$
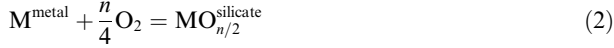
Where n is the valence of the cation M in the silicate melt. In this study, the partition coefficient D_M of an element M is defined as the ratio of the molar fractions of M in the metal over $MO_{n/2}$ in the silicate:

$$D_M = \frac{x_M^{metal}}{x_{MO_{n/2}}^{silicate}} \qquad (3)$$

With K the equilibrium constant of reaction (2) we derive the relationship:

$$\log D_M = -\frac{n}{4}\log fO_2 - \log K + \log\frac{\gamma_{MO_{n/2}}^{silicate}}{\gamma_M^{metal}} \qquad (4)$$

yielding a linear relationship between the logarithm of the partition coefficient and oxygen fugacity (fO_2). The slope ($-n/4$) gives the valence n of an element M in the silicate melt. To determine the effects of other variables (P, T, melt composition), it is necessary to compare the results at constant oxygen fugacity. An alternative approach, taken by Wade and Wood (2005) and Corgne et al. (2008), is to consider that metal silicate exchange of a cation M is related to the reduction–oxidation of iron as:

$$MO_{n/2}^{silicate} + \frac{n}{2}Fe^{metal} = \frac{n}{2}FeO^{silicate} + M^{metal} \qquad (5)$$

Taking logarithm of equilibrium constant K_a of reaction (5) yields:

$$\log K_a = \log\underbrace{\frac{(x_{FeO}^{silicate})^{n/2} \cdot (x_M^{metal})}{(x_{MO_{n/2}}^{silicate}) \cdot (x_{Fe}^{metal})^{n/2}}}_{K_M^D} + \log\frac{(\gamma_M^{metal})}{(\gamma_{Fe}^{metal})^{n/2}}$$
$$+ \log\frac{(\gamma_{FeO}^{silicate})^{n/2}}{(\gamma_{MO_{n/2}}^{silicate})} \qquad (6)$$

The exchange coefficient K_M^D is measured experimentally and calculation of activity coefficients in the metal is detailed further below. Following Wade and Wood (2005), we consider the ratio of oxide activity coefficients constant since it should not be strongly dependent of silicate melt composition. Then the apparent equilibrium constant used to report partitioning results can be expressed as:

$$\log K_{app} = \log K_M^D + \log\frac{(\gamma_M^{metal})}{(\gamma_{Fe}^{metal})^{n/2}} \qquad (7)$$

As discussed below (Section 4.5), the assumption that the ratio of oxide activity coefficients is constant as a function of melt composition appears to be a valid approximation for low valence cations but not necessarily for highly charged cations. To validate the use of Eq. (7) for all cations, values of $\log K_{app}$ were corrected using a proxy for the influence of silicate melt composition as discussed below in Section 4.5.

All the uncertainties reported for D_M and K_{app} are derived from the propagation of uncertainties in the analytical measurements. Calculated values for D_M and related uncertainties are given in Appendix C.

4.4. Effect of C and correction for metallic compositions

Presence of carbon in the metal phase is known to influence the partitioning of trace elements. Carbon saturation significantly increases the metal–silicate partition coefficients for W, Mo, Nb, Ta and V and decreases those of Ga, P and Zn, sometimes by more than an order of magnitude (see Fig. 4) and has been observed previously for some of these elements (Jana and Walker, 1997a; Righter and Drake, 2000; Chabot and Agee, 2003). To correct our partitioning data for solute interactions, we followed the thermodynamic approach employed by Wade and Wood (2005) and Corgne et al. (2008). The activity coefficients γ_{Fe}^{metal} and γ_i^{metal} were determined using the interaction parameter approach and the method described by Ma (2001). This approach allows the use of tabulated interaction parameters ε (e.g. The Japan Society for the Promotion of Science and The Nineteenth Committee on Steelmaking, 1988) and describes quantitatively the thermodynamics of multicomponent metallic solutions at both dilute and concentrated levels. The activity coefficients of Fe and the N-1 solutes (i) in a metallic solution containing N components can be expressed as:

$$\ln\gamma_{Fe} = \sum_{i=1}^{N-1}\varepsilon_i^i(X_i + \ln(1-X_i))$$
$$- \sum_{j=1}^{N-2}\sum_{k=j+1}^{N-1}\varepsilon_j^k X_j X_k\left(1 + \frac{\ln(1-X_j)}{X_j} + \frac{\ln(1-X_k)}{X_k}\right)$$
$$+ \sum_{i=1}^{N-1}\sum_{k=1(k\neq i)}^{N-1}\varepsilon_i^k X_i X_k\left(1 + \frac{\ln(1-X_k)}{X_k} - \frac{1}{1-X_i}\right)$$
$$+ \frac{1}{2}\sum_{j=1}^{N-2}\sum_{k=j+1}^{N-1}\varepsilon_j^k X_j^2 X_k^2\left(\frac{1}{1-X_j} + \frac{1}{1-X_k} - 1\right)$$
$$- \sum_{i=1}^{N-1}\sum_{k=1(k\neq i)}^{N-1}\varepsilon_i^k X_i^2 X_k^2\left(\frac{1}{1-X_i} + \frac{1}{1-X_k} + \frac{X_i}{2(1-X_i)^2} - 1\right)$$
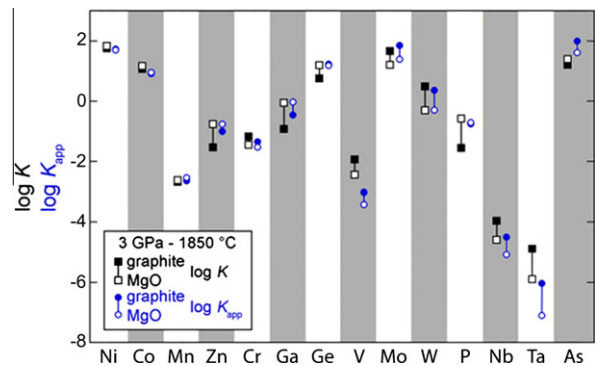$$(8)$$

Fig. 4. Effect of carbon on metal–silicate partitioning. The exchange coefficients K measured experimentally display the effect of C-rich liquid metal on partitioning (for #124 with graphite capsule compare to #139 with MgO capsule). Carbon has a positive effect on partitioning of Mo, W, Nb, Ta, and V and negative for Ga, Mn and P. Corrected values K_{app} (circles) for the effects of carbon and solutes interactions present a better agreement than measured K for most of the elements.

and

$$\ln \gamma_i = \ln \gamma_{Fe} + \ln \gamma_i^0 - \varepsilon_i^i \ln(1 - X_i)$$
$$- \sum_{j=1(j \neq i)}^{N-1} \varepsilon_i^j X_j \left(1 + \frac{\ln(1 - X_j)}{X_j} - \frac{1}{1 - X} \right)$$
$$+ \sum_{j=1(j \neq i)}^{N-1} \varepsilon_i^j X_j^2 X_i \left(\frac{1}{1 - X_i} + \frac{1}{1 - X_j} + \frac{X_i}{2(1 - X_i)^2} - 1 \right) \tag{9}$$

We used interaction parameters ε_i^j and activity coefficients γ_i^0 tabulated in the Steelmaking Data sourcebook (The Japan Society for the Promotion of Science and the Nineteenth Committee on Steelmaking, 1988). Values of the ε_i^j and γ_i^0 are reported at a reference temperature of 1873 K (see Appendix D) and extrapolated to run temperature following the relationships:

$$\ln \gamma_i^0(T) = \frac{T^0}{T} \ln \gamma_i^0(T^0) \tag{10}$$

and

$$\varepsilon_i^j(T) = \frac{T^0}{T} \varepsilon_i^j(T^0) \tag{11}$$

Values for ε_i^j and γ_i^0 are not yet quantified for all of the elements studied in this work (Appendix D) and are, hence, set to zero. Our inability to quantify these interactions could affect the calculation of activity coefficients for strong neglected interactions. However, we note that the interaction parameters for the carbon are relatively complete, i.e. ε_i^C parameters, under saturation conditions, were available for all the elements studied in this work. The ε_i^j approach takes into account the effects of temperature, but not those of pressure, due to the lack of high-pressure data. This along with the extrapolation of interaction parameters values to high temperature is a potential source of error when correcting for the effect of carbon on partitioning. Calculated partition coefficients corrected for the effect of carbon and solute interactions are in relatively good agreement with partition coefficients obtained for carbon free experiments (in MgO capsules) at similar conditions for most of the elements affected by the presence of carbon (Fig. 4), notably Mn, Zn, Ge, Ga, V and P. Corrections remain ineffective for Nb, Ta, As and Mo, however.

4.5. Silicate melt composition dependence

Experiments run at 3 GPa and 1850 °C were used to constrain the effect of silicate melt composition on partitioning. The compositional variation of silicate melts is expressed by the melt structural parameter nbo/t (Mysen et al., 1982), the molar ratio of non-bridging oxygens to tetrahedrally coordinated cations. The nbo/t parameter approach does not separate the effects of specific network modifying cations and does not consider any possible changes in cation coordination with pressure or temperature. Ideally the activities of individual oxides should be considered in describing the influence of melt composition on partitioning and the derivation of the activity coefficients ratio $\left(\gamma_{FeO}^{silicate} \right)^{n/2} / \left(\gamma_{MO_{n/2}}^{silicate} \right)$ in

Eq. (6). However, estimating activities in silicate melts is difficult given the scarcity of data. As done in previous related works (e.g. Walter and Thibault, 1995; Jana and Walker, 1997b; Jaeger and Drake, 2000; Cottrell et al., 2009) we use the nbo/t parameter as a first order approximation to characterize the effect of melt composition on partitioning, in particular the contribution of oxide activities. Results from our work (Fig. 5) in which nbo/t varies approximately between 1 (basalt) and 3 (peridotite) at 3 GPa and 1850 °C confirm results from previous studies (Jana and Walker, 1997b; Jaeger and Drake, 2000). The relative influence of melt composition on trace element partitioning is a function of cation oxidation state. Low valence cations (Cr^{2+}, Mn^{2+}, Co^{2+}, Ni^{2+}, Zn^{2+}) are essentially independent of the nbo/t parameter. However, high valence cations (P^{5+}, As^{5+}, Nb^{5+}, Mo^{4+}, W^{4+}) are strongly dependent of the nbo/t parameter with their affinity for silicate melts increasing in highly depolymerised melts (high nbo/t) (Fig. 5). This is because high valence cations may form polyhedral oxyanionic units with non-bridging oxygens and require more oxygens than divalent cations to be stabilized in the silicate melt (e.g. Ryerson, 1985). Basic silicate melts with high nbo/t ratio thus favor the solubility of high valence cations. Conversely, divalent cations can be integrated in the silicate network with fewer oxygens and their solubility is thus not as sensitive to nbo/t and the degree of polymerization. The partitioning of Ta and, to a lesser extent, Nb are exceptions for this trend, displaying unexpectedly weak dependencies with silicate melt composition for pentavalent cations.

Generally, for 2+ cations, the nbo/t dependence of K_{app} was considered negligible. FeO, NiO and CoO activity coefficients could vary by at least a factor of two over the range of compositions studied in this work and present a weak correlation with nbo/t (O'Neill and Eggins, 2002). However, since the activity coefficients of FeO, NiO and CoO are highly correlated (O'Neill and Eggins, 2002), it is reasonable to consider the ratio $\left(\gamma_{FeO}^{silicate} \right)^{n/2} / \left(\gamma_{MO_{n/2}}^{silicate} \right)$ to be constant, in good agreement with our experimental results. The same thermodynamic behavior was experimentally determined for other divalent cations like Cr or Mn in silicate melts (Hirschmann and Ghiorso, 1994; O'Neill and Berry, 2006). Activity coefficients for highly charged cations like Mo or W vary by a much larger factor (>20) over studied compositions and are more strongly influenced by changes in nbo/t than divalent cations (O'Neill and Eggins, 2002; O'Neill and Berry, 2006). Although the nbo/t parameter does not distinguish between the effects of MgO and CaO, estimating the $\left(\gamma_{FeO}^{silicate} \right)^{n/2} / \left(\gamma_{MO_{n/2}}^{silicate} \right)$ term in Eq. (6) using nbo/t is then an acceptable first order approximation.

4.6. Dependence on oxygen fugacity

As described above, we imposed different oxygen fugacities by varying the metallic silicon content of the starting materials. Oxygen fugacity relative to the iron-wüstite (IW) buffer is given by:

$$\Delta IW = 2 \log \left(\frac{a_{FeO}^{silicate}}{a_{Fe}^{metal}} \right) = 2 \log \left(\frac{x_{FeO}^{silicate}}{x_{Fe}^{metal}} \right) + 2 \log \frac{\gamma_{FeO}^{silicate}}{\gamma_{Fe}^{metal}} \tag{12}$$
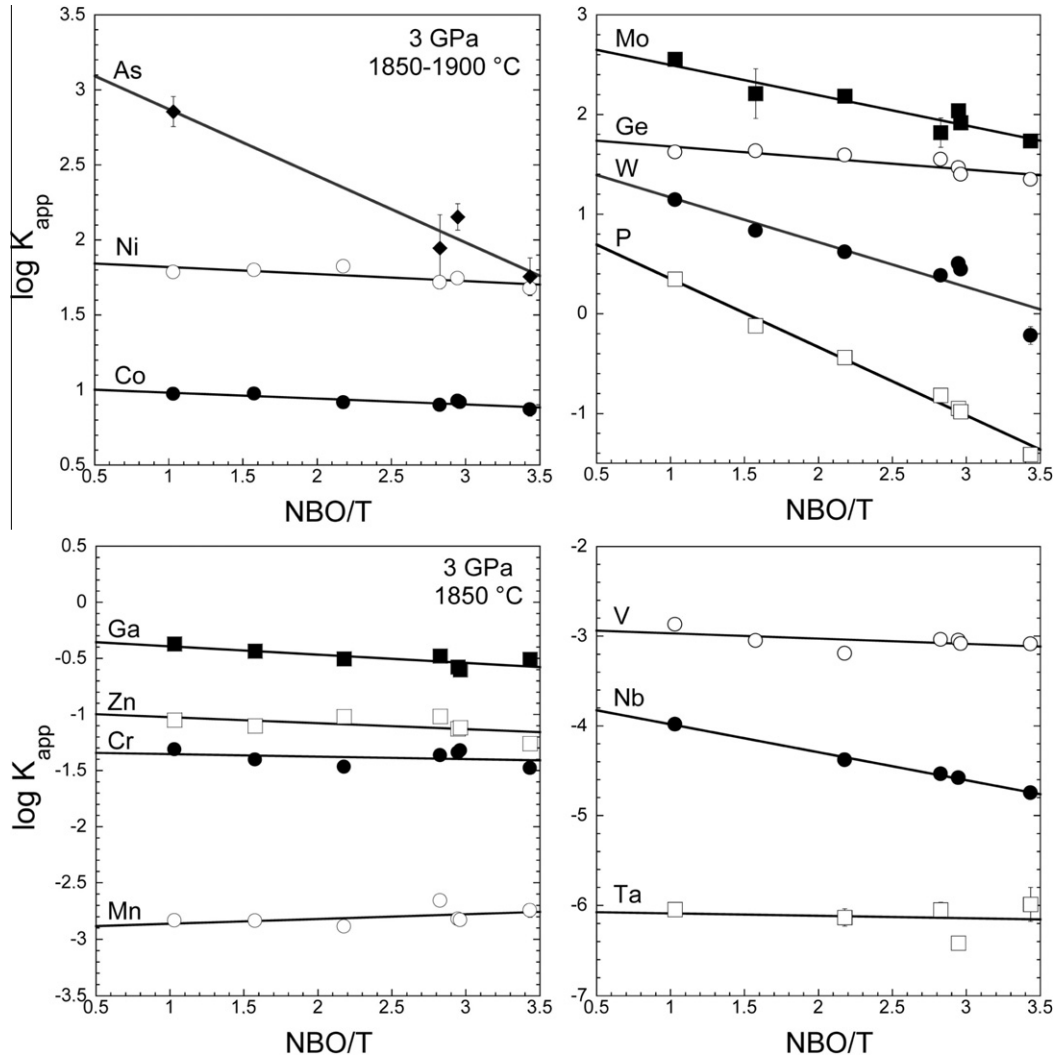
Fig. 5. Apparent equilibrium constant (K_{app}) plotted as a function of *nbo/t* for the 14 elements studied in this work. Dependencies are obtained from experiments of this work conducted at constant pressure and temperature (3 GPa–1850 °C) and are used to correct our dataset in Figs. 6–8 and model partitioning behaviors for *nbo/t* of 2.75 as estimated for the primitive mantle. Metal–silicate partitioning of high valence cations (4+, 5+) is strongly dependent of silicate melt composition expressed by the *nbo/t* parameter. No dependency for low valence cations (2+) is shown. Where no error bars are shown the uncertainties do not exceed the symbol size (also valid for the other figures).

where $a_{FeO}^{silicate}$ and a_{Fe}^{metal} are the activities of FeO in the silicate melt and Fe in the liquid metal, respectively. The activity coefficients for the metallic phase are estimated using the interaction parameter approach described previously. The values for γ_{Fe}^{metal} used to calculate ΔIW range roughly from 0.60 to 0.99 for carbon-bearing and carbon-free metallic compositions, respectively. An ideal mixing model for iron in the metallic alloys would thus decrease the calculated fO_2 by no more than half a log unit. FeO does not exhibit ideal mixing in silicate melts and $\gamma_{FeO}^{silicate}$ displays a small silicate melt compositional dependence (Holzheid et al., 1997; O'Neill and Eggins, 2002). Reported values of $\gamma_{FeO}^{silicate}$ from these studies yield a rough average of ~1.5 for compositions in the FCMAS system. Considering the absence of a simple dependence on any particular major element oxide component reported by O'Neill and Eggins (2002), a similar value of $\gamma_{FeO}^{silicate}$ was assumed for the different melt compositions studied here. Using these values for γ_{Fe}^{metal} and $\gamma_{FeO}^{silicate}$ in

Eq. (12) yields oxygen fugacities between −0.6 and −2.5 below the IW buffer for our experiments. Assuming ideal behavior for iron in both silicate and metallic melts would yield oxygen fugacities between −1.4 and −3.3 below the IW buffer (see Table 1).

We used isothermal and isobaric sets of experiments at 3 GPa and 1850 °C or 2200 °C to constrain the effect of oxygen fugacity on metal–silicate partitioning. Differences in silicate melt compositions among the runs of interest were corrected using results presented in Section 4.5. The variation in partition coefficients over 2 log units in fO_2 allows precise determination of valence state of various elements in the silicate melt. Following Eq. (4), the valence state can be estimated from the slope on a plot log D vs. ΔIW (Fig. 6). Whether we consider ideal or non-ideal behavior for fO_2 calculation does not induce any changes for the determined slopes and does not affect the valence state determinations. The calculated valences at both
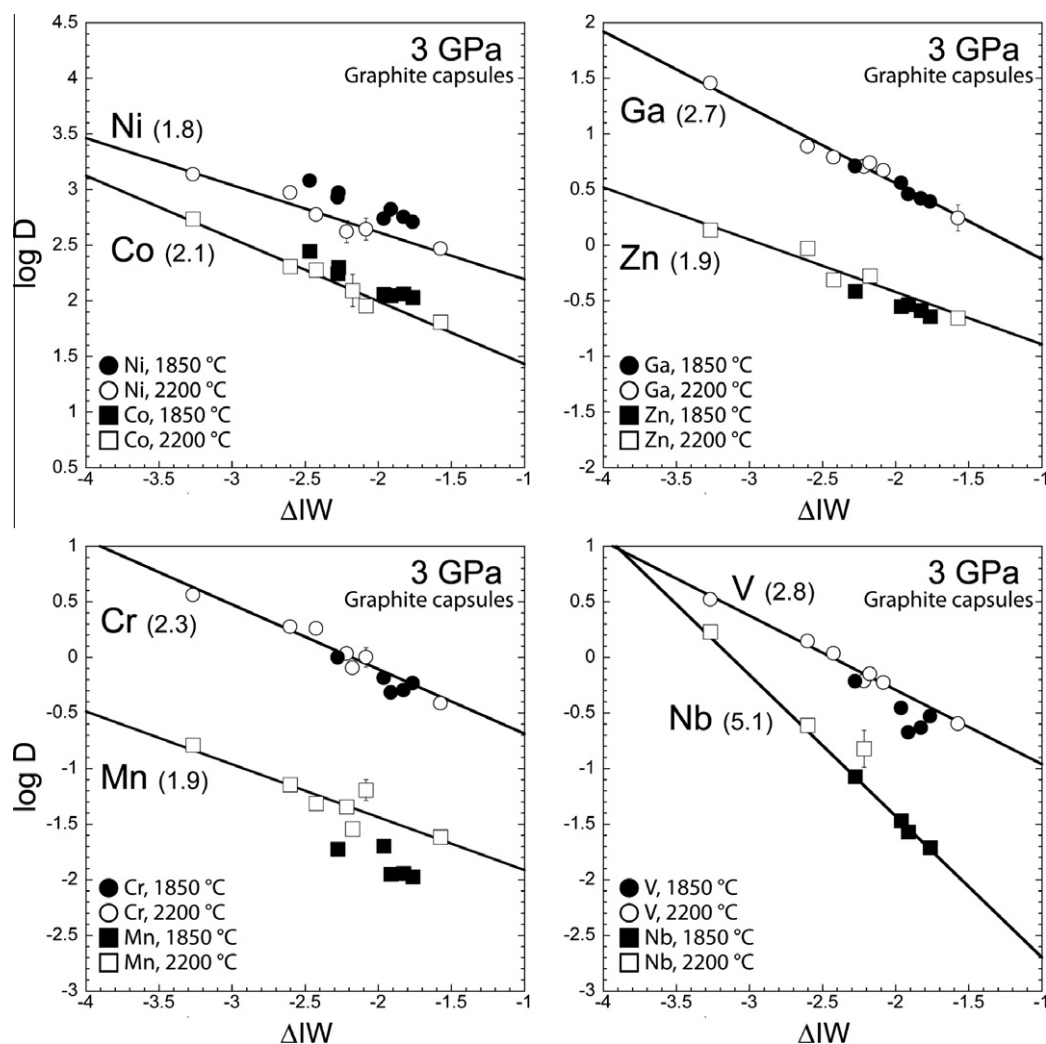
Fig. 6. Molar partition coefficients (D_M) as a function of the oxygen fugacity expressed relative to the IW buffer shown for experiments conducted with graphite capsules at 3 GPa, 1850 °C and 2200 °C, and a *nbo/t* of 2.75. Oxygen fugacity is calculated using an ideal model for activity coefficients of Fe in both metal and silicate melt (see text for details). The slope is proportional to the valence of the considered element in the silicate melt. Mean Valence obtained from experimental trends at 2200 °C (except As and Nb obtained from trends at 1850 °C) for each element is given in parentheses. Note the similar slopes and derived valence state obtained for data at 2200 °C and 1850 °C.

temperatures investigated (1850 and 2200 °C) are divalent for Ni, Co, Mn, Cr, and Zn (Fig. 6) in good agreement with previous experimental studies (e.g. Drake et al., 1989; Ding-well et al., 1994; Holzheid et al., 1994; Gessmann et al., 1999; Corgne et al., 2008). A summary of previous sidero-phile element valence state determinations, including those obtained at 1 atm in gas mixing furnace, is given in Appendix E. Cr^{2+} is likely to be the dominant oxidation state in silicate melts at fO_2 below the IW buffer (Berry et al., 2006) and Cr^{3+} is considered negligible. Only Gessmann et al. (1999) obtained results consistent with Cr^{3+} for similar fO_2 conditions. The explanation for the difference is likely the use of magnesiowüstite as a proxy for silicate melt in which Cr would be in a different oxida-tion state. The results for V, Ga, and Ge are consistent with a valence of 3+ (Fig. 6). For reducing conditions, V^{3+} has also been identified as the predominate valence by XANES spectroscopy (Righter et al., 2006; Karner et al., 2008) as

well as in previous metal–silicate partitioning experiments (Drake et al., 1989). Small amounts of V^{2+} may exist near IW-2 but was considered negligible. Results from Gess-mann et al. (1999) indicative of V^{2+} may again be attributed to a different oxidation state in magnesiowüstite, as opposed to silicate melt, for this element. In the case of gallium, our results confirm previous work at atmospheric pressure conditions that report a trivalent state for fO_2 ranging from IW+2 to slightly above IW-2 (Capobianco et al., 1999). For germanium, the 3+ valence could indicate a mixture of both Ge^{2+} and Ge^{4+} under the reduced exper-imental conditions of this work. However, the range of fO_2 investigated here is likely too small to reveal any change in the slope that would result from reduction of Ge^{4+} to Ge^{2+}. Capobianco et al. (1999) questioned the coexistence of Ge^{4+} to Ge^{2+} and concluded that only Ge^{4+} is required after correcting for interactions between Ge and major metallic component Ni or Fe. However, these experiments
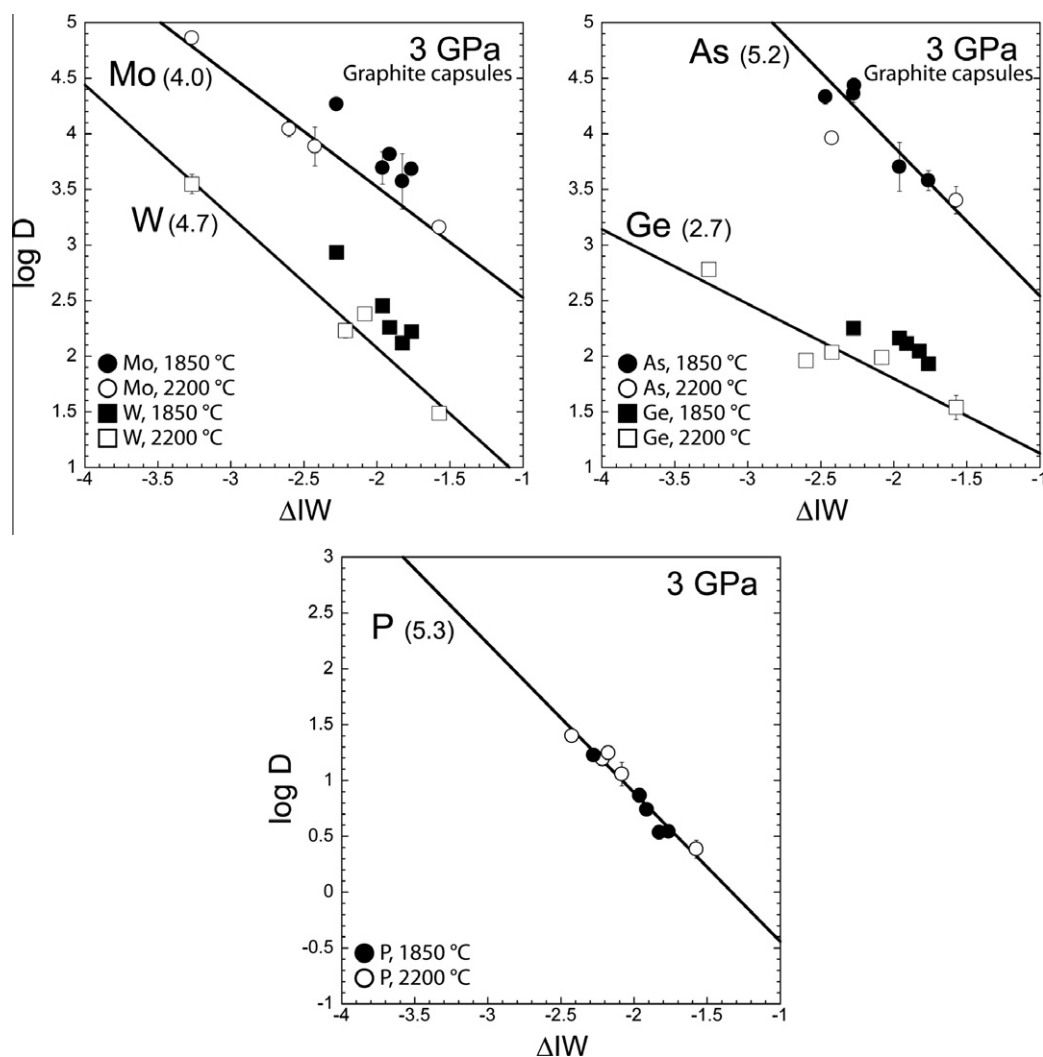
Fig. 6 (continued)

were conducted under more oxidized conditions (>IW-2), using various Fe–Ni alloy compositions, and partition coefficients at low fO_2 were measured with large uncertainties. This could explain the discrepancy observed for the valence of germanium between our work and that of Capobianco et al. (1999). From our dataset, a tetravalent state for Mo and W was considered. We derived valences of 4.1 and 4.5 for Mo and W, respectively (Fig. 6) and consider a tetravalent state as the predominant species for both elements. This result is in good agreement with several previous studies reporting Mo^{4+} as the dominant valence for fO_2 values below IW-1 (Holzheid et al., 1994; O'Neill and Eggins, 2002; Farges and Siewert, 2006). The valence state for W is more controversial. At 2200 °C, W^{4+} appears to be the dominant species but the fraction present as W^{6+} is significant. Less reduced conditions at 1850 °C, yield a slope consistent with W as W^{+6} (Fig. 6). Most of the available studies of metal–silicate partitioning imply an average oxidation state higher than 4+ for W in silicate melts (Schmitt et al., 1989; Walter and Thibault, 1995) as do recent XANES spectroscopic results from O'Neill et al. (2008). However, pressure effects could decrease the valence toward

W^{4+} as recently suggested by Cottrell et al. (2009). Thus, we assumed W^{4+} as the dominant species in subsequent parameterizations. Finally, regression yields valences of 5+ for P, As and Nb (Fig. 6) consistent with previous works (Righter et al., 1997; Wade and Wood, 2001; Corgne et al., 2008). No constraint on Ta valence state was obtained in this work due to the lack of reliable data over a sufficiently large range of fO_2. We thus assume a 5+ valence for Ta as observed by Corgne et al. (2008). Heterovalent elements are likely to occur in more than one oxidation state at redox conditions relevant to Earth's core formation. This work does not provide a systematic study of the transitions between the different valence state regimes and the relative proportions of the different species present at fO_2s relevant to core formation. This issue should be considered in future work and could provide insight on the behavior of the geochemical twins, e.g. Mo/W, Nb/Ta, etc. and their mantle ratios. There is currently no solid experimental evidence to assess possible changes in the oxidation state as a function of pressure and we consider the valence states obtained at 3 GPa reliable for higher-pressure conditions in subsequent discussion.
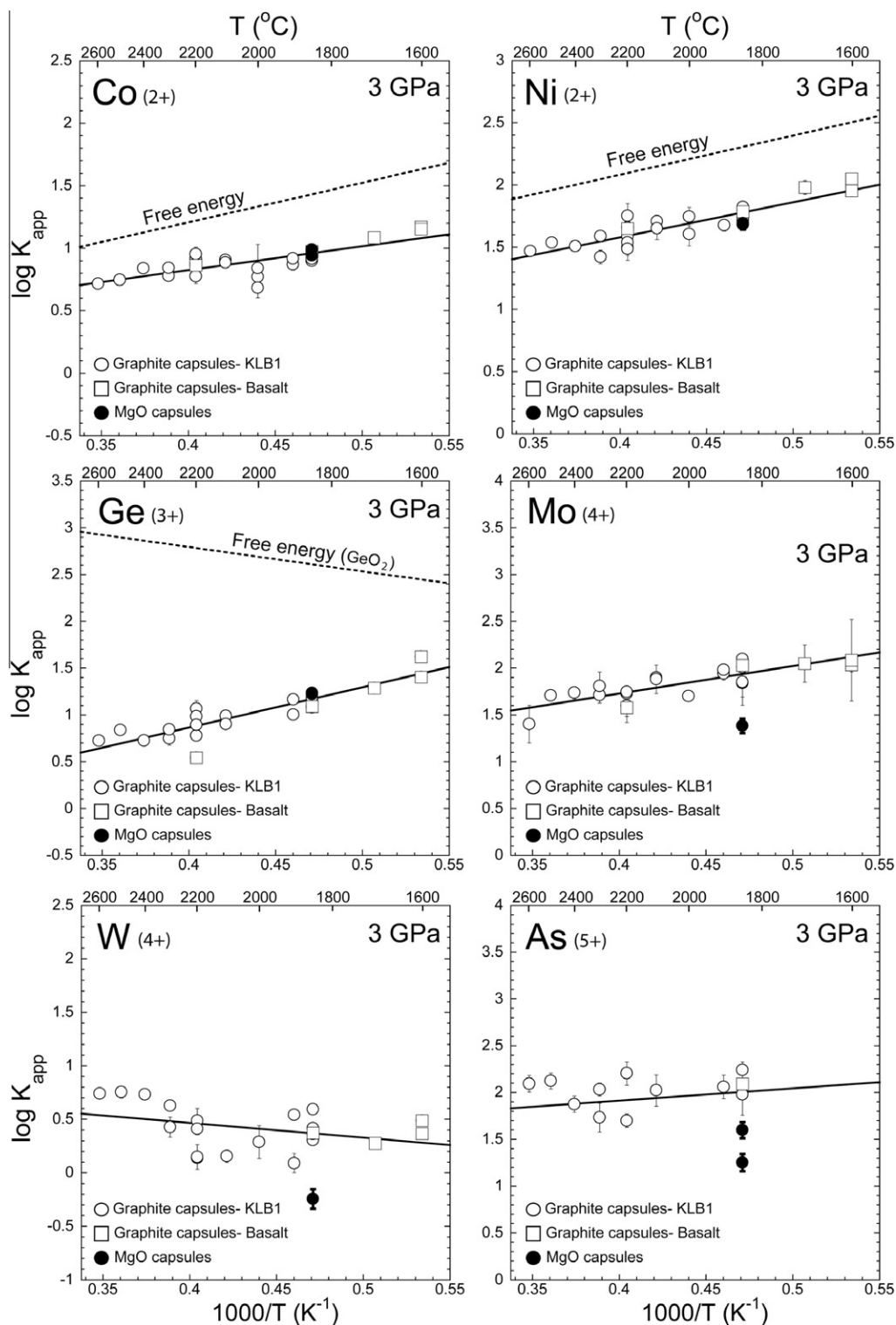
Fig. 7. Apparent equilibrium constant (K_{app}) plotted as a function of reciprocal temperature ($1000/T$). Data shown here were obtained from experiments conducted at 3 GPa with graphite (unfilled white symbols) or MgO (filled black symbols) capsules and are recalculated for *nbo/t* of 2.75. Data collected with KLB-1 or tholeiite basalt as starting silicate material present a good agreement after corrections for the silicate melt composition. Dashed lines representing 1 bar free energy data taken from Barin et al. (1989) and Chase (1998) do not match the *T* dependencies (solid lines) observed for many elements (i.e. Ga, Nb, Ta, V, Zn). Ge presents mixed 2+ and 4+ valence state while the free energy trend showed here is defined for a 4+ valence state. Regression constant for the T effect is derived from graphite capsule experiments. Data obtained with MgO capsule for W, Mo, As, and Ga show that interaction parameters used to correct for the effect of C on partitioning should be better constrained at conditions of our experiments.
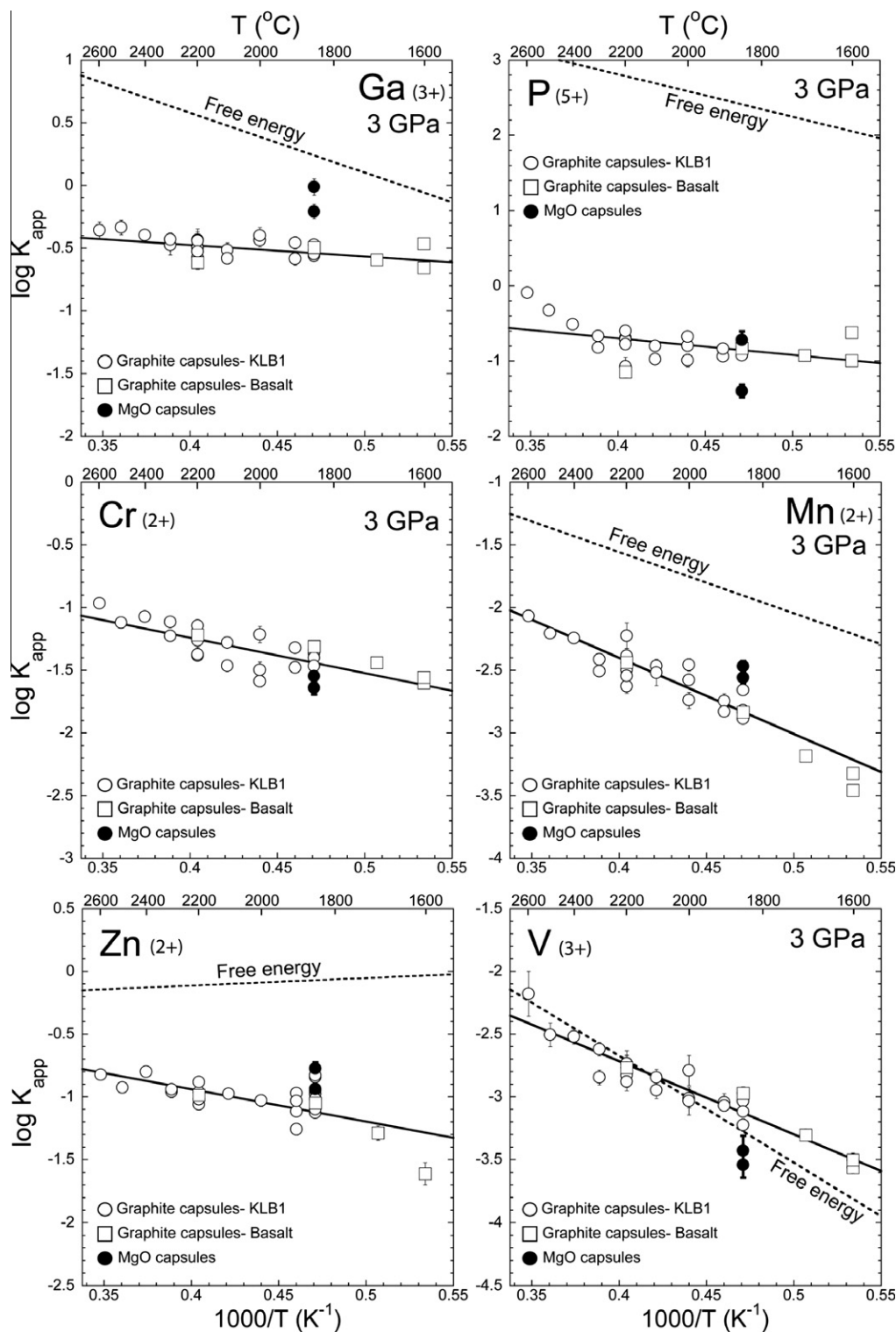
Fig. 7 (continued)

4.7. Temperature dependence

An important focus of this work was to constrain more precisely the effect of temperature on metal–silicate partitioning. Experiments were performed at 100 °C intervals over a wide temperature range (1600–2600 °C) above the liquidus of both silicate and metal at 3 GPa. We used a basalt composition with a lower melting point than peridotite for experiments between 1600 and 1800 °C to extend the domain of studied temperature and derive accurate regression coefficients for modeling temperature dependence. Note that an experiment at 2200 °C was also performed
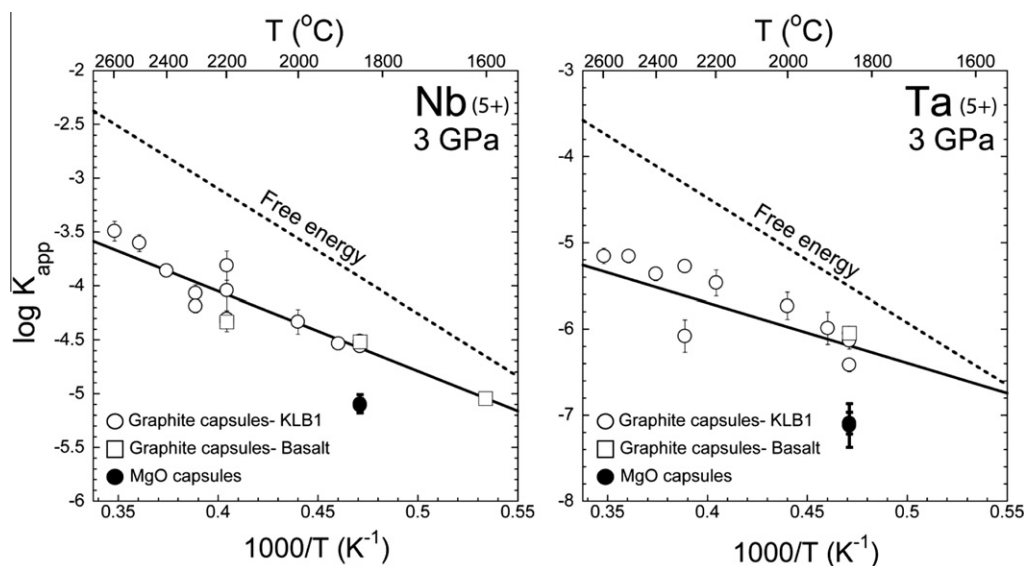
Fig. 7 *(continued)*

with basaltic melt to compare directly with results obtained at the same temperature for a peridotite melt. The partitioning data for different compositions were then "corrected" to a peridotite melt composition ($nbo/t = 2.75$) using the results described in Section 4.5 (Fig. 5). As expected, trace element partitioning dependence on temperature varies for different elements (Fig. 7). Values of K_{app} decrease for Ni, Co, Ge, Mo and As and increase for V, Cr, Mn, Zn, Nb and Ta with increasing temperature. Negligible or very weak dependence of K_{app} with temperature is reported for Ga, P, and W, however. For most of the elements, the observed trends are in good agreement with previous works on the effect of temperature on partitioning (e.g. Walter and Thibault, 1995; Gessmann and Rubie, 1998; Chabot and Agee, 2003; Chabot et al., 2005; Wade and Wood, 2005; Corgne et al., 2008; Wood et al., 2008). A summary of individual effects of P, T, fO_2 and composition on partitioning for the elements studied in this work and by other investigators is given in Appendix F. However, we obtained trends different from published ones for Ga (Righter and Drake, 2000), P (Righter et al., 1997; Righter and Drake, 2000), W (Righter et al., 1997), Zn (Corgne et al., 2008), and Ge (Schmitt et al., 1989). These discrepancies are likely due to a combination of factors in these investigations including: (1) a limited range of temperatures investigated, (2) compositional effects associated with Fe-poor metallic alloys and high trace element doping levels, (3) subliquidus experimental conditions, (4) oxidizing experimental conditions (>IW-1) leading eventually to a change in the valence state of some elements. In this context, we note that recent results on W (Cottrell et al., 2009) or Zn (Mann et al., 2009), collected over a large temperature range, displayed temperature effects similar to those observed here.

Wade and Wood (2005) and Corgne et al. (2008) estimated the effect of temperature on partitioning by assuming that low pressure log K_{app} experimental data should define trends parallel to log K_{app} of exchange reaction (5) calculated from 1 bar free energy data of pure components. Our results, along with recent work by Mann et al. (2009), indicate that this method provides reliable approximations for the effect of temperature on partitioning for a number of low valence cations e.g. Ni, Co, Mn (Fig. 7). However, as demonstrated by results for Cr (see Mann et al., 2009), Zn, Ga and Ge, this approximation is not universally applicable, with particular difficulties associated with highly charged cations. In these instances application of this approximation may be limited by a number of factors including: (1) unavailability of thermodynamic data for some reduced oxide components (CrO, GeO) in either the solid or liquid state; (2) approximations of liquid state thermodynamics properties for oxides that decompose before melting, e.g. WO_2 and MoO_2, may lead to errors on estimated free energies (entropies of melting are derived from TiO_2 for WO_2 and MO_2 (Chase, 1998)); (3) mixed valence states at fO_2 conditions relevant for core formation precludes the use of the free energy of a single, mono-valent component to model T effect; (4) some elements (Mo, W, P, Nb) dissolve in silicate melts largely as complexes with Ca, Mg or Al notably occurring as discrete anionic units and this is not reflected in the free energy of formation of pure components; and (5) Activity coefficient ratios $\dfrac{\left(\gamma_{FeO}^{silicate}\right)^{n/2}}{\left(\gamma_{MO_{n/2}}^{silicate}\right)}$ may be temperature dependent. Thus, temperature effects predicted from free energy calculations of exchange reaction (5) can be a source of errors for partitioning models of some elements (e.g. Ga, V, Zn, Nb) (See Fig. 7).

4.8. Pressure dependence

A combination of isothermal (1850–1900 °C) multi-anvil and piston-cylinder experiments was conducted between 0.5 and 18 GPa to assess the effect of pressure on metal–silicate partitioning. We used MgO capsules rather than graphite

capsules in this set of experiments to better contain metallic melts at pressure above the graphite/diamond transition and to eliminate the potential effects of C on partitioning (see Methods). Results obtained with MgO capsules as a function of pressure are presented in Fig. 8. All results are "corrected" to a constant nbo/t value of 2.75 corresponding to a peridotite melt composition. A significant decrease in K_{app} values is observed for Ni, Co, Mo, As, Ga, and Nb with increasing pressure. A small negative effect for Zn, W and Ge, and a positive effect for Mn and Cr with pressure are also reported. Effect of pressure on K_{app} for V seems negligible. These results are generally consistent with previous investigations at high pressure (For Ni and Co, Thibault and Walter, 1995; Li and Agee, 2001; Wade and Wood, 2005; Kegler et al., 2008 – Mo, Righter et al., 1997 – Ga, Righter and Drake, 2000 – Nb, Wood et al., 2008 – V, Cr, and Mn, Chabot and Agee, 2003 – W, Cottrell et al., 2009) (see also Appendix F). The magnitude of the pressure effect for these elements is mostly within uncertainty of that from related works except for the Ga results in Wade and Wood (2005). In contrast to the results of Righter and Drake (2000), Corgne et al. (2008), and Wood et al. (2008) no negative pressure effect was detected for Ta, P, and V, respectively. The small number of reliable data for Ta and very scattered results for P in this work as well as in previous investigations does not allow an accurate determination of the effect of pressure on the partitioning of these elements. Note that results obtained for Ge and As are to our knowledge the first to constrain the pressure effect for these elements. Experimental determination of the partial molar volume of GeO_2 in silicate melts (Holzapfel et al., 2001) predicts a negative volume change of reaction (5) leading to an increase in Ge siderophility with pressure. However, this is not applicable for GeO, the dominant germanium oxide at oxygen fugacity of core–mantle equilibrium. A regime transition around 3–5 GPa for pressure dependence has been proposed for Ni, Co, and W. Ni and Co partitioning display a strong pressure effect at low pressure followed by a much weaker dependence above 5 GPa (Kegler et al., 2008) while W exhibits a reversal from positive to negative pressure dependence at ∼3–4 GPa (Cottrell et al., 2009). This could be attributed to a transition in the silicate melt structure with a change in coordination or a change in the valence for these elements. Here, speculation with regard to such changes in pressure dependencies for Ni, Co, Mo, and W are ambiguous. Hence, the regression coefficients derived for pressure in this work do not consider such potential effects. This may not be so critical in any case given the putative high-pressure conditions of core formation. Additional systematic works at low pressure are required to validate these results. Extrapolations to higher pressure (>18 GPa) are only valid if no structural and/or coordination changes are assumed.

5. DISCUSSION

5.1. Parameterizing metal–silicate partition coefficients

To model the geochemical consequences of various core formation scenarios we follow Corgne et al. (2008) expressing the apparent equilibrium constant as a function of the different thermodynamic variables that affect partitioning behavior:

$$\log K_{app} = a + \frac{b}{T} + \frac{c \cdot P}{T} + d \cdot (nbo/t) \tag{13}$$

where a, b, c and d are regression constants, T the temperature in K, P the pressure in GPa, and nbo/t the molar ratio of non-bridging oxygens over tetrahedral cations in the silicate melt. The coefficients, a, b, c and d derived from least squares multi-variable regression are given in Table 5. Note that d was considered negligible for divalent elements. The pressure term for V, Cr, Ge and temperature term for Ga, As, and W are not statistically significant. Regarding the large uncertainties on the pressure and temperature terms and the negligible dependence on silicate melt composition, the results for Ta were not considered reliable for modeling core formation. By combining Eqs. (3), (7), and (13) the molar partition coefficients of an element i measured experimentally can be parameterized as follow:

$$\log D_M = a + \frac{b}{T} + \frac{c \cdot P}{T} + d \cdot (nbo/t) - \frac{n}{2} \log \left(\frac{x_{FeO}^{silicate}}{x_{Fe}^{silicate}} \right)$$
$$- \log \frac{\left(\gamma_M^{metal} \right)}{\left(\gamma_{Fe}^{metal} \right)^{n/2}} \tag{14}$$

We assumed Raoult's Law behavior for Fe, γ_M^{metal} was calculated at the relevant temperature using Eq. (10) and data tabulated in the Steelmaking Data sourcebook (The Japan Society for the Promotion of Science and the Nineteenth Committee on Steelmaking, 1988), and finally a magma ocean melt composition characterized by $nbo/t = 2.75$ was assumed.

For the sake of comparison, Appendix F provides a literature review of partitioning parameterization according to Eq. (13) for all the elements of interest. As a whole, this table summarizes the main agreements or discrepancies between published works and this study regarding the individual effect of each variable on metal–silicate partitioning.

5.2. Implications for single-stage core formation models

Here, we evaluate the possibility that single stage core formation can reproduce the observed terrestrial mantle siderophile element pattern. This scenario implies constant P, T and fO_2 conditions during core–mantle equilibration. In this fairly simplistic scenario, droplets of molten Fe-alloy equilibrate with the surrounding molten mantle at fixed P–T–fO_2 conditions corresponding to the final depth of a magma ocean. The Fe-alloy is then assumed to sink rapidly in the solid lower mantle as large diapirs with negligible re-equilibration (Stevenson, 1990). Alternatively, if the silicate magma ocean equilibrates with falling metallic droplets at local P–T conditions over its thickness then a compositional gradient will develop in the primitive mantle due to P–T variations in the partition coefficients. In this case, the P–T conditions of equilibration represent an average for the entire mantle and the depth of the magma ocean would be significantly greater than the value suggested by the apparent equilibration pressure (Rubie et al., 2003). Moreover, in a more
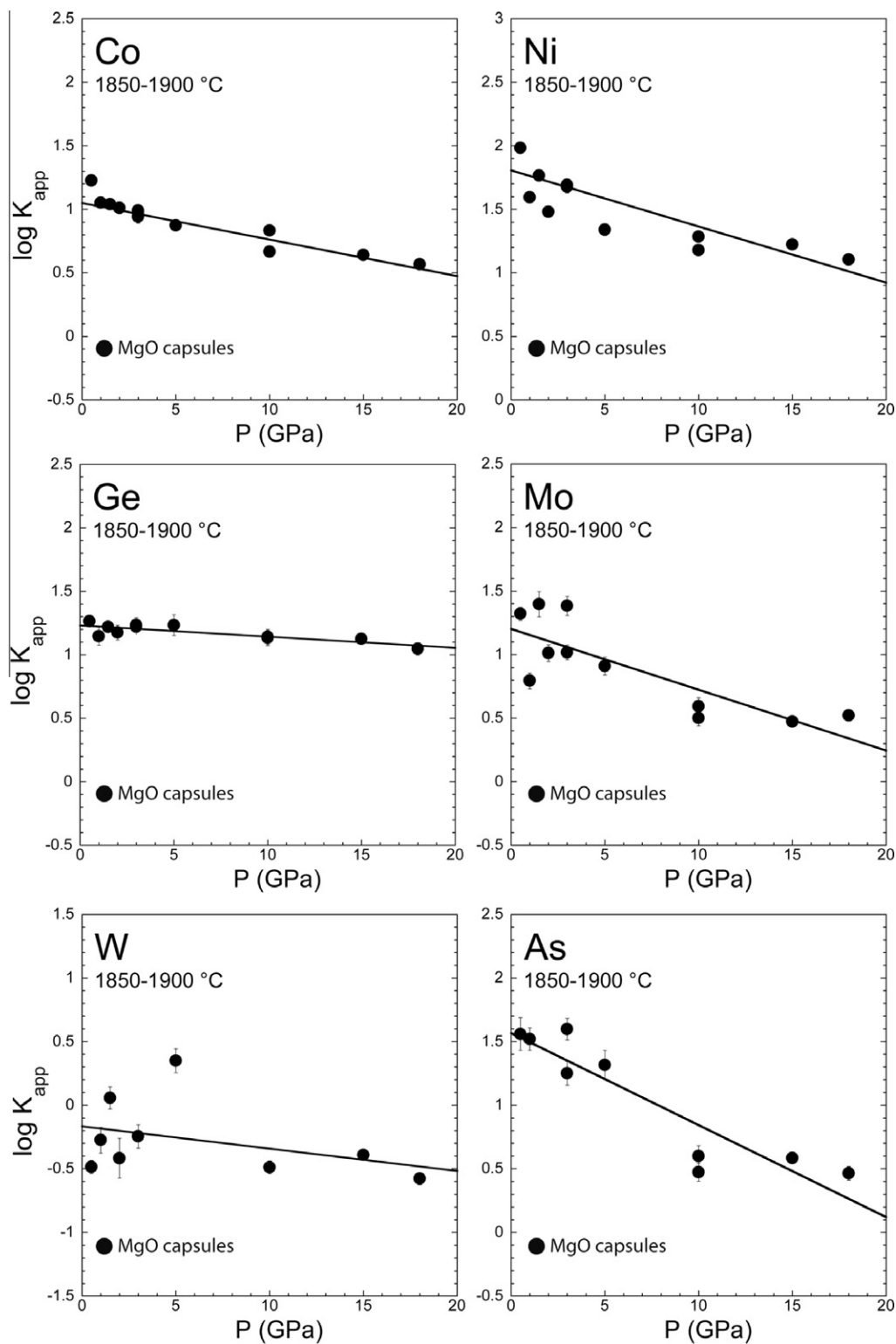
Fig. 8. Apparent equilibrium constant (K_{app}) plotted as a function of pressure. Data for constraining pressure dependencies (regression constant c in Eq. (13)) were obtained from experiments conducted at isothermal temperature (1850–1900 °C) in MgO capsules and recalculated for *nbo/t* of 2.75.

dynamic process, the single P–T condition is likely to represent the average of a wide range of conditions for the magma ocean generated from a series of various accretion events

including late giant impacts. No matter which hypothesis is the most physically relevant, we address here the possibility of a single P–T–fO_2 solution for the core–mantle
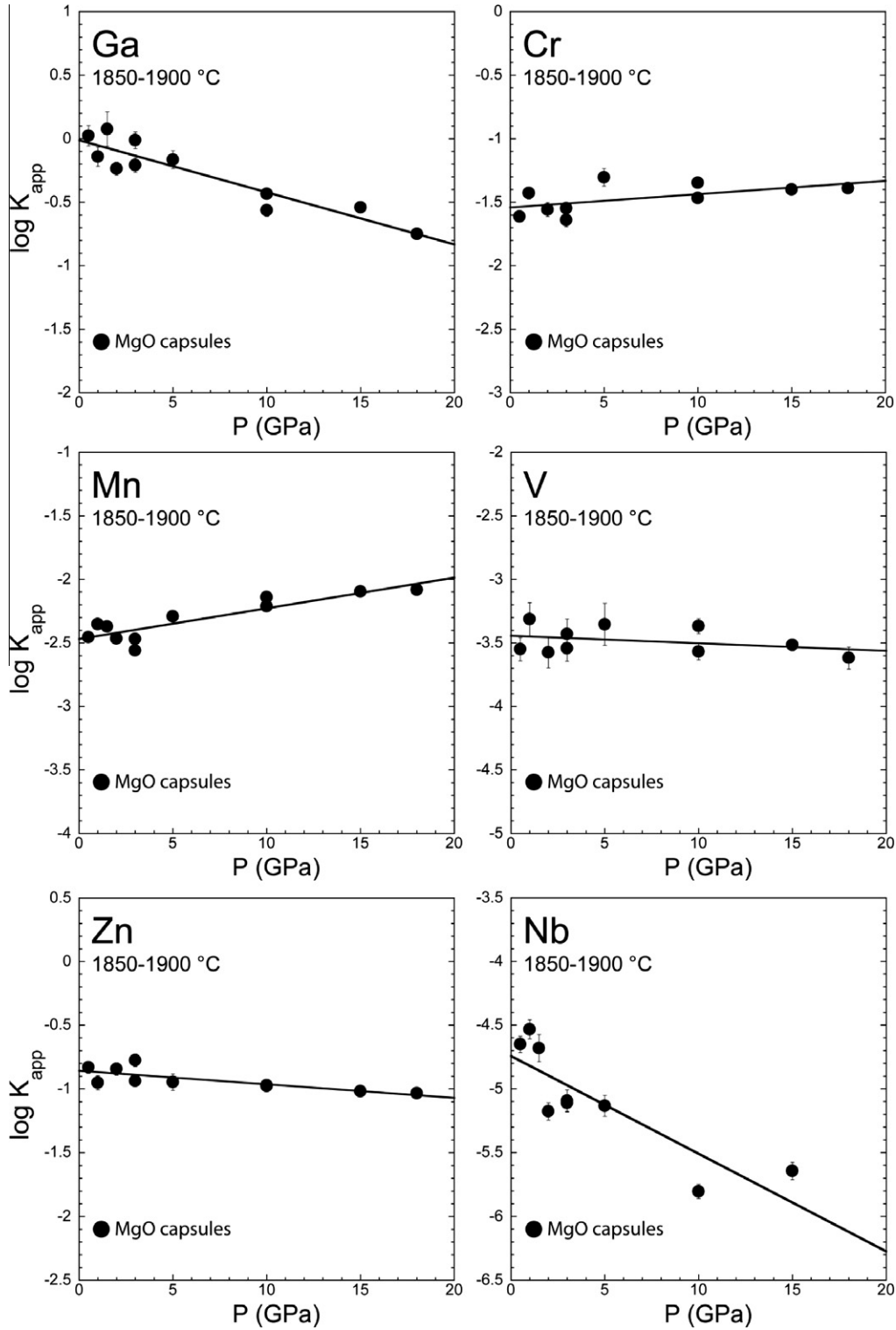
Fig. 8 *(continued)*

equilibration to account for the observed abundances of many siderophile elements in the mantle.

Rearranging Eq. (14) to express pressure as a function of temperature leads to:

$$P = \frac{T}{c} \cdot \left[\log D_i - a - d \cdot (nbo/t) + \frac{n}{2} \log \left(\frac{x_{\mathrm{FeO}}^{\mathrm{silicate}}}{x_{\mathrm{Fe}}^{\mathrm{metal}}} \right) \right.$$

$$\left. + \log \frac{\left(\gamma_{\mathrm{M}}^{\mathrm{metal}} \right)}{\left(\gamma_{\mathrm{Fe}}^{\mathrm{metal}} \right)^{n/2}} \right] - \frac{b}{c} \qquad (15)$$

Table 5
Multiple linear regression coefficients.

Element	v[a]	n[b]	a	±[c]	b	±	c	±	d	±
Ni	2	35	0.35	0.07	2934	279	−83	17	0	0
Co	2	35	0.20	0.03	1892	238	−66	8	0	0
Mn	2	36	0.53	0.04	−6356	418	46	10	0	0
Zn	2	31	0.57	0.03	−3015	406	−26	7	0	0
V	3	36	−0.46	0.06	−5964	513	−19[*]	14	−0.063	0.026
Cr	2	36	0.26	0.06	−3318	495	13[*]	14	−0.056	0.025
Ga	3	36	0.51	0.05	−795[*]	375	−88	12	−0.06	0.02
Nb	5	25	−0.97	0.10	−6855	653	−154	32	−0.23	0.04
Ta	5	17	−3.41	0.12	−7910	969	35[*]	31	0	0
Ge	2	33	0.01	0.03	4504	387	−3[*]	8	−0.12	0.04
As	5	21	2.56	0.10	982[*]	799	−155	23	−0.41	0.04
Mo	4	33	0.42	0.10	3117	539	−97	25	−0.27	0.03
P	5	37	2.03	0.17	−2698	1062	99[*]	42	−0.71	0.05
W	4	29	1.96	0.14	−937[*]	741	−55	35	−0.57	0.04

[*] When values for coefficients b or c are not statistically significant.
[a] Valence used for the regression.
[b] Number of experimental data from this work used for the regression.
[c] Errors are two standard deviations.

Using this expression it is then possible to calculate the conditions of pressure and temperature which mutually satisfy the apparent bulk core–mantle partition coefficients D_i for the elements investigated here. Taking the current FeO content of the mantle ~8 wt% based on upper mantle rocks (massif peridotites and xenoliths) and chondritic abundances (Allègre et al., 1995; McDonough and Sun, 1995; Palme and O'Neill, 2003) and a core containing 85 wt% Fe, the fO_2 is constrained during a single stage core formation event to approximately IW-2.3. Apparent core–mantle partition coefficients D_i listed in Table 6 are derived from the relative abundances of a siderophile element and a lithophile element with similar volatility trend (i.e. with similar half-mass condensation temperature) in the primitive mantle (based on upper mantle rock analyses) and CI chondrites. Mantle abundances for volatile elements such as Ga, Ge, and Zn are far less well constrained than for Ni and Co (e.g. Corgne et al., 2008). Mantle concentrations of refractory elements such as W, Mo or Nb (McDonough and Sun, 1995; McDonough, 2003; Palme and O'Neill, 2003) are also not sufficiently well-known to provide a reduced range of possible apparent core–mantle partition coefficients. This, combined with errors on regression constants a, b, c, d leads to large P–T solution domains for most of the siderophile elements. It is therefore necessary to combine constraints from multiple elements to converge towards an allowable mutual solution. Given the complex relationship linking P and T in Eq. (15), we propagated uncertainties using Monte–Carlo simulations. 10,000 values of partition coefficients (D_i) and regression coefficients were randomly generated with the density appropriate to the probability distribution. P at fixed T and T at fixed P were then calculated for each of the 10,000 simulations. From their statistics, we derived the 2σ uncertainties on P–T solutions to Eq. (15), which we use in the subsequent models.

The P–T solution domains for metal–silicate equilibration at an oxygen fugacity fixed by the current FeO content of the present upper mantle (8 wt%), corresponding to

Table 6
Apparent core–mantle partition coefficients.

Element	D core/mantle	Lithophile element[a]	References[e]
Ni	24–28	–[b]	(1)–(4)
Co	23–26	–	(1)–(4)
Mn	0–2	–	(1)–(4)
Zn	0–8	F ($T_c \sim 730$ K)[c]	(1) and (2)
V	1.3–2.5	RLE[d] ($T_c > 1400$ K)	(1) and (2)
Cr	2–4	–	(1)–(4)
Ga	0–0.8	Na ($T_c \sim 950$ K)	(1) and (2)
Nb	0–1	RLE	(1) and (2)
Ta	0–0.4	RLE	(1) and (2)
Ge	9–17	Rb ($T_c \sim 950$ K)	(1) and (2)
As	40–100	Li ($T_c \sim 1150$ K)	(1) and (2)
Mo	90–150	RLE	(1) and (2)
P	20–50	–	(1)–(4)
W	10–30	RLE	(1)–(5)

[a] Lithophile element used to determine the bulk Earth abundance of a siderophile element with similar volatility trend.
[b] Bulk Earth abundance was taken directly from references.
[c] Reference temperature at which half the mass of a specific element condensates into a mineral from a cooling solar nebula under a given oxygen partial pressure. Condensation temperatures and volatility order are from Wasson (1985), Allègre et al. (2001), and Lodders (2003).
[d] Refractory lithophile elements (e.g. Al, Ti, Ca, Sc, REE).
[e] References for siderophile and lithophile element abundances in both upper mantle rocks and chondrites CI used to calculate the ranges of apparent core–mantle partition coefficients. (1) McDonough and Sun (1995); (2) Palme and O'Neill (2003); (3) Allègre et al. (2001); (4) Allègre et al. (1995); and (5) McDonough (2003).

IW-2, illustrate how the final mutual P–T solution domain for Ni, Co, Cr and Mn is obtained from the overlap of each individual solution domains (Fig. 9a). Ni and Co are mainly pressure dependent and constrain a high pressure solution between 32 and 42 GPa. Mn and Cr limit the range of possible T solutions between 2500 and 4000 K. In this framework, addition of Mo, Zn and W slightly lowers the
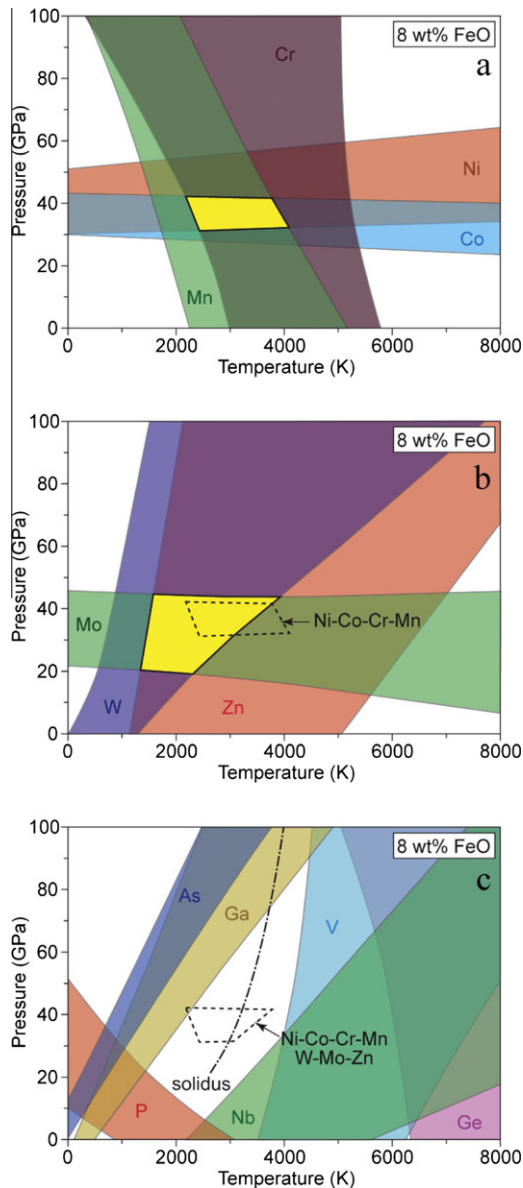
Fig. 9. Diagrams showing the *P–T* conditions of core–mantle equilibration required to match the mantle abundances of the studied siderophile elements for a fO_2 fixed by present FeO content of the mantle (8 wt%). The individual solution for each element is calculated using Eq. (15) and taking account of uncertainties on the *a–b–c–d* regression constants and the apparent core–mantle partition coefficients values. In (a) the solution domain is first constrained from the Ni–Co–Mn–Cr set. It is further restricted in (b) with the additions of solutions for Mo, W, and Zn. In (c) the P–T solution domain for Ni–Co–Mn–Cr–Zn–Mo–W overlap the mantle solidus but is not consistent with the solutions for Ga, Ge, Nb, V, As, and P. A single stage core formation model at this fO_2 condition would not match the abundances of these elements in the mantle. Note that the modeling assumes no effect of core's unknown light element(s) on metal–silicate partitioning.

T domain below 4000 K (Fig. 9b). From this experimental dataset, we derive a possible *P–T* region at high pressure and high temperature (Fig. 9c) to explain the mantle depletions of seven siderophile elements Ni, Co, Mn, Cr, Zn,

Mo, and W all together. As can be seen in Fig. 9c, estimate of the mantle solidus by Zerr et al. (1998) lie within that *P–T* solution domain giving a physically relevant single stage solution at 32–42 GPa and 3000–3200 K. It is indeed necessary that the last equilibration of the sinking metallic droplets takes place at a solid–liquid interface (i.e. bottom of the magma ocean) whether we consider gradual or homogeneous equilibration of the magma ocean (see above in the
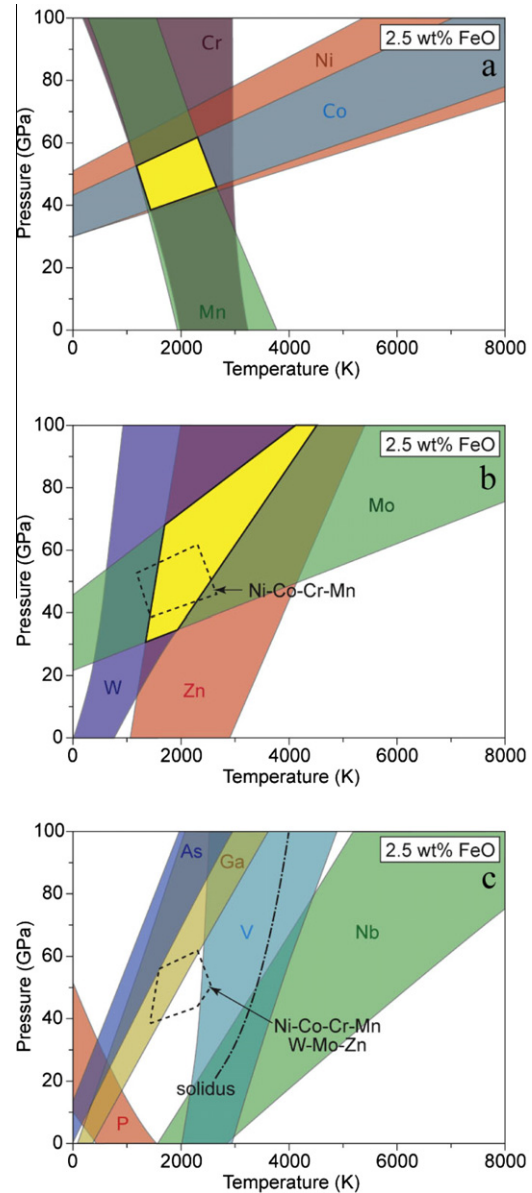
Fig. 10. Diagrams showing the conditions of pressure and temperature required to match the mantle abundances of the studied siderophile elements for a fO_2 fixed by a low FeO content of the mantle of 2.5 wt% (~IW-3.3). In (a) and (b) a solution domain is constrained from the individual solutions of Ni–Co–Mn–Cr–Zn–Mo–W. In (c) solutions for V, Ga, and As intersect the solution domain defined by Ni–Co–Mn–Cr–Zn–Mo–W but well below the mantle solidus. No solution for Ge is available at these conditions. These reducing conditions do not provide a viable solution for a magma ocean scenario.

discussion). However, this P–T solution domain is not consistent with the individual solutions for Ga, Ge, V, Nb, As, and P (Fig. 9c). The minimum temperature defined by the V–Nb solution is ~1000 K above the peridotite solidus and ~600 K above our single stage solution defined for the seven elements considered above, in relatively good agreement with previous works for V (Wood et al., 2008; Corgne et al., 2008). The solution for Ge, taken as 2+ for this low fO_2, is well above 5000 K. Modeling Ge as Ge^{4+} would have little effect on the solution, which would still require the temperature to be in excess of 4500 K. Finally Ga, P, and As solutions are well below the solidus and the T range of the Ni–Co–Mn–Cr–Zn–Mo–W solution. The disparity between all these possible solutions indicates that a single-stage model cannot be supported at this fO_2 condition.

The disparity among the various "IW-2.3" solutions is diminished if we consider core segregation at lower oxygen fugacity, IW-3.3 (Fig. 10). For these conditions the temperature obtained for the Ni–Co–Cr–V–Zn–W–Mo solution combined with solutions for Ga, As, and V is lower than that at IW-2.3 and yields P–T conditions that are well below the peridotite solidus. This mismatch is exacerbated considering that the mantle solidus at low fO_2 and low FeO content should be located at higher temperatures than that of normal peridotite. Thus, these conditions are not relevant for core formation within a magma ocean, do not provide any possible solution for Ge, and further, would lead to an unrealistic FeO content for the mantle of 2.5 wt%.

Although its viability is questioned by the present results, we cannot unambiguously exclude the possibility of a single stage core equilibration scenario without considering the effects of light elements (Si, S, C, O) on metal–silicate partitioning. In this context, Corgne et al. (2009) have recently proposed that presence of oxygen in the segregating core could shift the required conditions, notably

for V, towards the mantle solidus. Additional experimental data and calculations are required to determine the effects of light elements on several key siderophile elements (e.g. V, Ge, Ga). Moreover, thermodynamic extrapolations performed in this work are only valid if no liquid structural transitions in both silicate and metallic melts occur at higher pressure. Diamond anvil cell experiments above 30 GPa and 3000 K would be required to directly constrain partitioning coefficients if these are core forming conditions.

5.3. Implications for a continuous core segregation model

Recognizing the disparity between allowable single stage core formation P–T conditions and the peridotite liquidus, Wade and Wood (2005) proposed a more physically plausible continuous core formation scenario. In this model, P–T conditions at the base of the magma ocean, the locus of final core–mantle equilibrium, change with time as the Earth grows. Also, fO_2 conditions evolve during accretion from initially reducing, to explain observed depletions of slightly siderophile elements (e.g. V, Mn), to more oxidized at the end. With growth and increasing pressure, perovskite becomes stable in the lower mantle, and its affinity for ferric iron drives the disproportionation of ferrous iron yielding Fe^{3+}-rich perovskite iron plus iron metal (Frost et al., 2004). Ferric iron is subsequently released to the magma ocean during repeated dissolution of Fe^{3+}-rich perovskite. This raises the FeO content of the mantle to its present-day level at the end of core formation. Here, we use our partitioning results to calculate the evolution of siderophile elements core–mantle concentration ratio during continuous core segregation.

Following Wade and Wood (2005) accretion is modeled in 1% steps and the pressure of equilibration in the magma ocean was fixed at 35% of the value at the core–mantle boundary according to Ni and Co partitioning. This leads to a mean pressure of accretion of 29 GPa. Equilibration
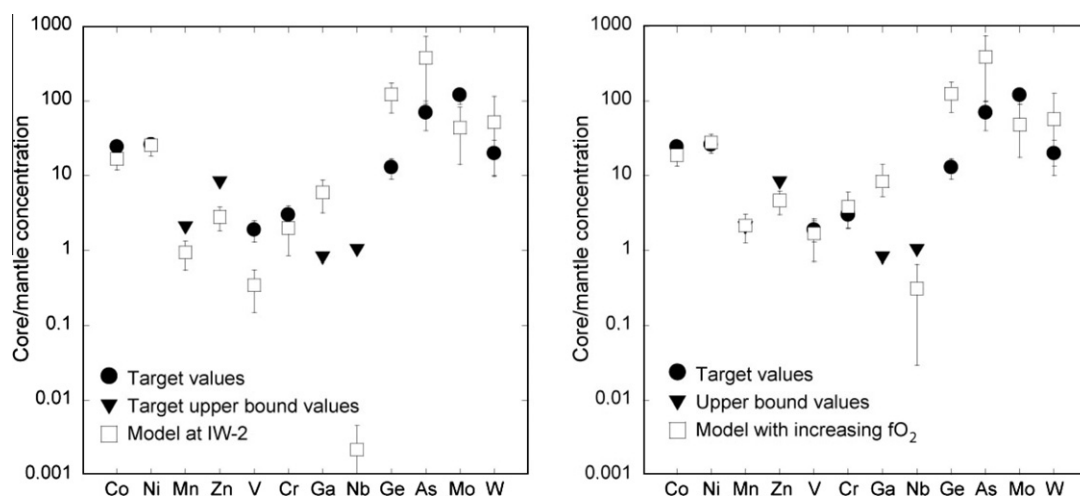
Fig. 11. Calculated core–mantle partition coefficients obtained using the present experimental data as input to a continuous core formation model. Filled black dots and triangles give respectively the target values and upper limits for observed core–mantle partitioning following Table 6. Unfilled dots give the results obtained at the end of the accretion process. Error bars give 2σ uncertainties. (A) Results for a continuous core formation model with constant oxygen fugacity. (B) Results for a continuous core formation model with increasing oxygen fugacity conditions during accretion (from 0.8 wt% FeO to 8 wt% FeO in the silicate Earth, see text for details).

temperatures were constrained to the peridotite solidus, estimated from the data of Fiquet et al. (2010). This leads to a mean temperature of accretion of 2930 K. We estimated the core to constitute 32 wt% of the Earth. We consider two fO_2 paths by varying the FeO content of the silicate melt. In the first case, the FeO content of the mantle was fixed at its current value (8 wt%). This means that the fO_2 is fixed during core formation at about IW-2. In the second case, conditions become progressively oxidizing starting from reduced conditions with an initial FeO mantle content of 0.8 wt% (Wood et al., 2008). Oxygen fugacity was fixed at this value for the first 35% of accretion until perovskite is stable, and then gradually increased to reach current core–mantle equilibrium value (8 wt%) at the end of accretion. A 2-sigma uncertainty on the regression coefficients (Table 5) was propagated in predicting the range of core–mantle partitioning results. The calculated Ni, Co, Mn, Zn, Cr, As, Nb and W partitioning, with a fixed FeO-constant fO_2 magma ocean matches the observed core mantle partition coefficients values (Fig. 11). However, as shown in Figs. 11 and 12, calculated partitioning values

for V, Ga, Ge, and Mo do not match the observed terrestrial values. A more successful agreement for the partitioning of V and Mo was achieved starting with reduced conditions followed by progressive oxidation during accretion (Figs. 11 and 12). In that case V becomes more siderophile and its target value can be reached for temperatures along the mantle solidus during core–mantle equilibrium. A similar effect is observed for Nb (Fig. 11b). However, this model results in Ga and Ge becoming more siderophile which is the opposite of the behavior required to match their observed target values. Note that using the slightly different oxygen fugacity path proposed by Wood et al. (2008), with the mantle oxidizing in two steps, do not change our conclusions for these elements. These partitioning results show that current abundances of Ga and Ge in the Earth cannot be reconciled with proposed continuous core formation models. The delivery of a late veneer (around ∼0.5% according to Brenan and McDonough (2009)) of chondritic component to the mantle after core formation is neither likely to provide the abundances of Ge and Ga in the silicate Earth. Considering natural
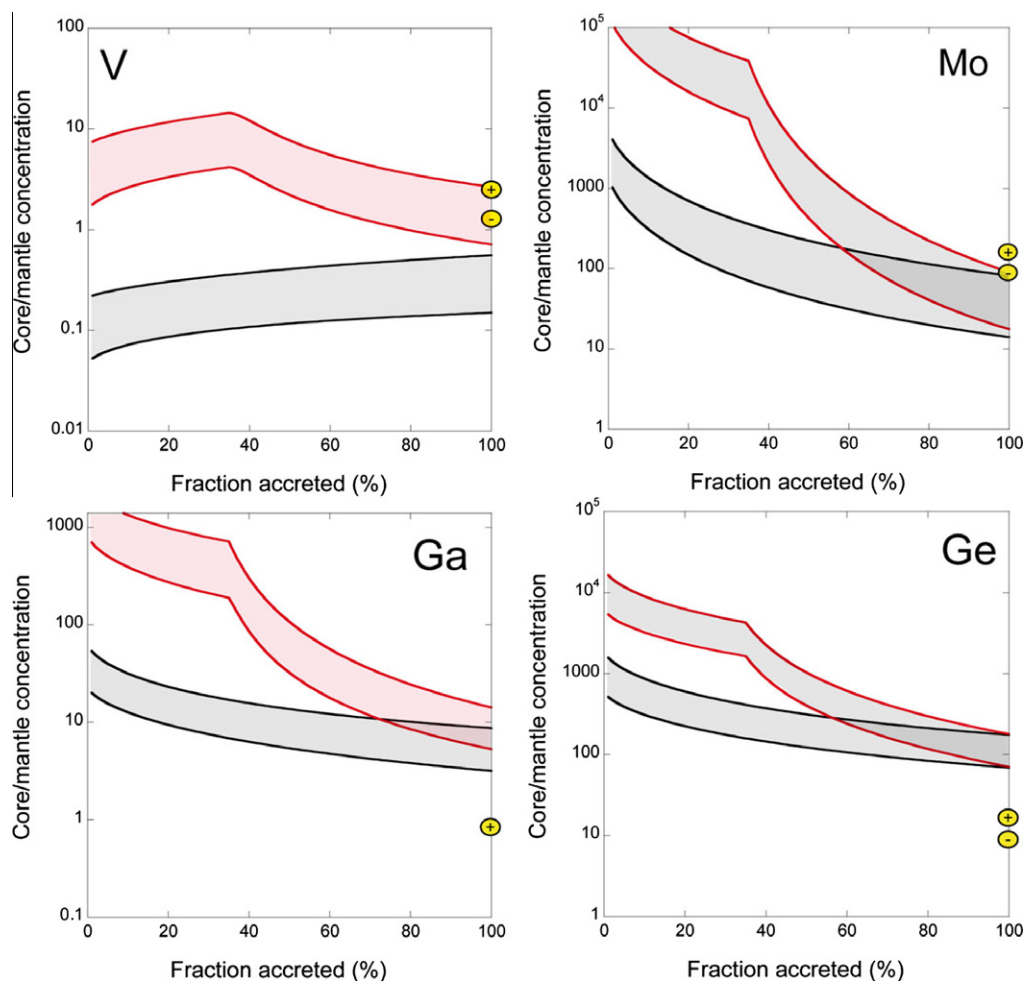
Fig. 12. Evolution of V, Mo, Ga, and Ge "partitioning" during continuous core segregation in a deep magma ocean during accretion. Upper and lower limits of apparent core–mantle partitioning values of the Earth are represented by + and − symbols. Black path shows results for model with constant oxygen fugacity corresponding to 8 wt% FeO in the silicate Earth. Red path shows results for model with increasing oxygen fugacity conditions (from 0.8 wt% FeO to 8 wt% FeO in the silicate Earth). Required partitioning values for Ga and Ge cannot be match in either case. (For interpretation of the references in colour in this figure legend, the reader is referred to the web version of this article.)

abundances (McDonough and Sun, 1995; Palme and O'Neill, 2003) and metal–silicate partitioning from this work, the addition of at least 3% CI material would be required to match Ge and 20% for Ga. Effects of light elements on partitioning of these two elements need to be investigated experimentally to provide further constraints on this type of model.

6. CONCLUSION

Our systematic experimental study provides tight new constraints on the factors that affect metal–silicate partitioning for 14 siderophile elements. New results are obtained for elements whose partitioning behavior was poorly constrained or not integrated into any accretion or core formation models. Carbon dissolved in liquid metal has a positive effect on the partitioning of W, Mo, Nb, Ta and V and decreases the partitioning of Ga, P and Zn sometimes by more than an order of magnitude. Isolation of the carbon effect was performed using carbon-free experiments and thermodynamic corrections to assess correctly the individual effects of other variables. We find, as in previous investigations, that the influence of silicate melt composition on partitioning is a function of the oxidation state. Highly charged cations (e.g. W, Mo, P) are greatly affected by silicate melt composition while no effect is evidenced for low valence state elements (e.g. Ni, Zn, Cr). We derived the valences of the studied cations in silicate melt from the dependence of partitioning on oxygen fugacity. Our data indicate, notably, a 2+ state for Zn and Cr, a 3+ state for Ga and V, a 4+ state for Mo and a 5+ state for Nb and As. We also derive a mixture of 2+ and 4+ oxidation states for Ge and 4+ and 6+ for W at redox conditions of the experiments. However, we show that Ge^{2+} and W^{4+} are likely to be the dominant species at oxygen fugacities relevant to core–mantle equilibration. We obtain tight constraints on the temperature effect for most of the elements. With increasing temperature, V, Cr, Mn, Zn, Nb and Ta become more siderophile while Ni, Co, Mo, Ge and As become less siderophile. Temperature has no significant effect on the partitioning of Ga, W and P. We show that the assumption of temperature trends parallel to those predicted from oxide free energy are not applicable for some elements (e.g. V, Ga) and can lead to significant imprecision when modeling core formation scenarios. The individual effect of pressure was also assessed. The siderophility of Ni, Co, Ga, W, Mo, As and Nb decreases with increasing pressure. Pressure influence is not very significant or even negligible for other elements.

We used multi-variable regression to parameterize and extrapolate partitioning at conditions of core formation. For single stage, fixed P–T–fO_2, core–mantle equilibrium at the base of a magma ocean, consideration of partitioning behavior for multiple siderophile elements reduces the range of acceptable P–T solutions regarding the large uncertainties on apparent core–mantle partition coefficients and regression parameters for each element. Required abundances of Ni, Co, Cr, Mn, Zn, W and Mo in the mantle can be explained by single core–mantle equilibration at 32–42 GPa and 3000–3200 K for a FeO content of the present mantle. However, higher temperatures would be required to explain abundances of V, Nb and Ge while solutions for Ga, As and P are below the mantle solidus at these conditions. These disparities argue against the single stage core formation model. We also tested the hypothesis of continuous core formation with both fixed and increasing oxygen fugacity during accretion. As previously demonstrated (Wade and Wood, 2005; Wood et al. 2008), the model invoking progressive oxidation provides a solution to match current mantle abundances of numerous siderophile elements, including Co, Ni, Mn Cr and most notably V which is not well matched by continuous core formation at fixed fO_2. However current abundances of Ga and Ge cannot be reconciled with this scenario. The effects of light elements (Si, C, S, O and H) and validation of thermodynamic models estimating their influence on activity-composition behavior at relevant P–T conditions is still poorly constrained and should be further evaluated to fully test these core equilibration models.

Appendix A
Pressure calibration for 1/2″ assemblies.

Runs #	Assembly (see Fig. 1)	P (Kbar)[a]	T (°C)	T (h)	Al_2O_3 (wt.%) measured in Enstatite[b]	Friction loss (%)[c]
56	1/2″ classic	30	1300	24	5.4 ± 0.1	4
57	1/2″ classic	30	1600	24	10.2 ± 0.2	3
91	1/2″ High T	30	1600	20	10.5 ± 0.2	7
92	1/2″ High T	30	1300	20	5.7 ± 0.2	10

[a] Nominal (gauge) pressures.

[b] Measurements of Al_2O_3 were done by EPMA running at 15 kV and 10 nA.

[c] Runs effective pressure and associated friction loss were constrained using the Al_2O_3 contents of enstatite in equilibrium with pyrope following Perkins et al. (1981). Starting materials were mixtures of synthetic pyrope + Al-free enstatite.

Appendix B
LA-ICPMS analyses of glass reference materials and comparison with published values.

Standards (ppm)	NIST 610 (references)	NIST[c]	BCR-2G (this work) N = 20	BCR-2G (references)	BCR-2 (USGS)[h]	BHVO-2G (this work) N = 20	BHVO-2G (references)	BHVO-2 (USGS)	#124 (metal) N = 10	#124 (metal) (EPMA) wt%
P 31	342 (53)[a]	–	1275 (14)	1590 (24)[b]	1500 (100)	986 (18)	980–1539[b,f]	1200 (100)	4636 (429)	0.428 (0.031)
Ti 47	434 (15)[a]	(437)	12964 (206)	13005 (1081)[d]	13500 (300)	15587 (201)	15621 (453)[d]	16400 (200)	5 (2)	–
V 51	442 (43)[a]	–	419 (4)	425 (7)[d]	416 (14)	317 (2)	329 (9)[d]	317 (11)	2818 (172)	0.292 (0.011)
Cr 52	405 (32)[a]	–	17.7 (0.3)	17 (2)[d]	18 (2)	281 (3)	285 (14)[d]	280 (19)	5469 (102)	0.555 (0.019)
Mn 55	433 (32)[a]	485	1472 (12)	1463 (23)[d]	1520 (60)	1269 (11)	1345 (25)[d]	1290 (40)	264 (8)	0.0180 (0.040)
Co 59	405 (23)[a]	(390)	39 (1)	39 (2.7)[e]	37 (3)	47.5 (1.2)	47 (2)[d]	45 (3)	(int. Std.)	1.384 (0.028)
Ni 60	444 (24)[a]	459	11.4 (0.4)	11 (1)[e]	–	120.5 (1.4)	112 (9)[d]	119 (7)	57813 (730)	5.577 (0.120)
Zn 66	456 (19)[a]	(433)	142 (3)	153 (9)[d]	127 (9)	107.4 (1.4)	107 (26)[d]	103 (6)	2386 (53)	0.216 (0.015)
Ga 69	438 (11)[a]	–	46 (5)	22.3 (1.2)[e]	23 (2)	26.7 (1.2)	21 (1)[d]	21.7 (0.9)	17614 (636)	1.429 (0.049)
Ge 72	426 (9)[a]	–	2.1 (0.1)	1.9 (0.1)[b]	–	2.0 (0.1)	1.60–2.40[g,b]	–	11872 (480)	1.113 (0.051)
As 75	317 (12)[a]	–	1.1 (0.1)	< 2.4[f]	–	0.85 (0.08)	–	–	11759 (648)	1.084 (0.068)
Nb 93	419 (58)[a]	–	11.6 (0. 3)	12.69 (0.73)[e]	–	16.8 (0.5)	16.4 (0.7)[d]	18 (2)	359 (19)	–
Mo 95	377 (45)[a]	–	232 (3)	238–269[g,b]	248 (15)	3.7 (0.1)	3.8–4.1[g,b]	–	14551 (355)	1.545 (0.051)
Ta 181	377 (78)[a]	–	0.62 (0.02)	0.63 (0.06)[d]	–	0.90 (0.03)	0.94 (0.07)[d]	–	42 (5)	–
W 182	447 (21)[b]	–	0.50 (0.02)	0.53 (0.02)[e]	–	0.22 (0.02)	0.24 (0.02)[b]	–	19054 (425)	1.985 (0.072)

[a] Pearce et al. (1997).
[b] Shaheen et al. (2008).
[c] NIST = NIST certified values (open) and information values (in brackets).
[d] Gao et al. (2002).
[e] Barrat et al. (2007).
[f] Gagnon et al. (2008).
[g] Jochum et al. (2005).
[h] USGS (2002) data are USGS certified values for the BCR-2 and BHVO-2 bulk powder reference material.

Appendix C
Summary of metal/silicate partition coefficients (D_M).

D_M	D_{Ni}		D_{Co}		D_{Mn}		D_{Zn}		D_V		D_{Cr}		D_{Ga}		D_{Nb}	
50	330,6	(16,0)	79,6	(3,5)	0,0090	(0,0003)	–		–		0,189	(0,011)	1,47	(0,19)	–	
51	325,6	(16,7)	77,7	(3,6)	0,0086	(0,0003)	–		0,026	(0,005)	0,195	(0,007)	1,45	(0,13)	–	
52	828,0	(48,7)	177,5	(8,8)	0,0355	(0,0010)	–		–		–		29,10	(8,42)	0,010	(0,001)
85	441,5	(101)	90,3	(9,3)	0,0641	(0,0139)	–		0,445	(0,041)	0,998	(0,201)	3,31	(0,47)	–	
93	425,0	(91,6)	83,7	(5,2)	0,0251	(0,0019)	–		0,298	(0,031)	0,392	(0,038)	3,64	(0,41)	–	
94	406,4	(40,9)	86,1	(8,0)	0,0135	(0,0017)	0,143	(0,014)	0,21	(0,017)	0,403	(0,021)	2,47	(0,23)	0,011	(0,001)
95	524,3	(37,9)	111,2	(5,8)	0,0321	(0,0031)	–		0,344	(0,024)	0,510	(0,021)	2,64	(0,29)	–	
96	293,3	(28,9)	64,5	(3,5)	0,0242	(0,0011)	0,221	(0,012)	0,223	(0,020)	0,385	(0,028)	1,26	(0,34)	0,010	(0,003)
97	235,0	(26,1)	71,3	(2,9)	0,0263	(0,0018)	0,319	(0,029)	0,265	(0,005)	0,777	(0,037)	2,49	(0,38)	0,023	(0,001)
101	758,0	(56,6)	139,9	(7,3)	0,0020	(0,0001)	–		0,073	(0,002)	0,233	(0,011)	2,24	(0,13)	0,009	(0,001)
102	627,9	(97,4)	74,5	(12,6)	0,0191	(0,0025)	–		0,316	(0,041)	0,522	(0,068)	4,30	(0,45)	0,034	(0,005)
103	418,8	(93,9)	66,1	(18,1)	0,0453	(0,0064)	–		0,497	(0,048)	1,077	(0,118)	3,97	(0,47)	0,054	(0,021)
116	852,2	(59,9)	175,2	(6,4)	0,0188	(0,0015)	0,386	(0,020)	0,567	(0,026)	0,995	(0,037)	4,92	(0,25)	0,071	(0,005)
118	–		184,8	(9,0)	0,0201	(0,0015)	0,419	(0,028)	0,61	(0,027)	1,127	(0,061)	5,28	(0,54)	–	
120	–		237,8	(102)	0,0749	(0,0056)	0,742	(0,048)	1,613	(0,185)	2,220	(0,264)	5,48	(0,69)	–	
121	678,0	(137)	154,2	(6,8)	0,0398	(0,0094)	0,493	(0,030)	0,574	(0,043)	1,158	(0,073)	4,73	(0,36)	–	
122	596,6	(56,6)	189,2	(9,7)	0,0486	(0,0055)	0,490	(0,026)	1,037	(0,081)	1,814	(0,124)	5,77	(0,47)	–	
124	546,7	(46,5)	114,2	(5,1)	0,0200	(0,0007)	0,280	(0,022)	0,347	(0,027)	0,648	(0,028)	3,55	(0,31)	0,031	(0,002)
126	511,8	(21,0)	107,1	(3,2)	0,0106	(0,0002)	0,229	(0,014)	0,333	(0,009)	0,587	(0,012)	3,14	(0,11)	0,058	(0,001)
127	864,6	(106)	150,7	(10,3)	0,0049	(0,0003)	0,135	(0,017)	0,16	(0,007)	0,462	(0,016)	2,70	(0,14)	–	
128	836,7	(78,6)	182,7	(8,0)	0,0036	(0,0001)	0,067	(0,013)	0,131	(0,006)	0,359	(0,011)	2,40	(0,08)	–	
129	455,6	(24,4)	109,2	(4,5)	0,0444	(0,0021)	0,428	(0,034)	0,657	(0,029)	1,320	(0,064)	4,65	(0,43)	0,056	(0,003)
130	353,8	(27,2)	100,6	(7,2)	0,0622	(0,0028)	0,646	(0,024)	0,897	(0,063)	1,413	(0,046)	4,56	(0,28)	0,101	(0,002)
131	339,1	(16,7)	72,6	(2,9)	0,0619	(0,0033)	0,468	(0,032)	0,613	(0,073)	1,156	(0,044)	4,44	(0,46)	0,131	(0,011)
132	365,1	(19,8)	85,1	(4,2)	0,1091	(0,0072)	0,717	(0,053)	1,849	(0,446)	2,094	(0,106)	5,53	(0,68)	0,213	(0,024)
133	721,4	(160)	123,7	(41,3)	0,0287	(0,0036)	0,531	(0,026)	0,679	(0,029)	0,801	(0,052)	5,25	(0,22)	–	
134	938,1	(67,8)	203,7	(8,9)	0,0717	(0,0035)	0,937	(0,070)	1,41	(0,072)	1,886	(0,123)	8,18	(0,49)	0,330	(0,017)
135	1374	(148)	543,0	(32,4)	0,1625	(0,0090)	1,368	(0,157)	3,422	(0,256)	3,626	(0,176)	28,94	(3,23)	1,799	(0,080)
139	939,1	(54,1)	200,6	(12,8)	0,0324	(0,0017)	2,389	(0,207)	0,185	(0,029)	0,484	(0,026)	45,25	(4,44)	0,018	(0,001)
140	1205	(63,8)	278,9	(11,0)	0,0482	(0,0036)	2,232	(0,119)	0,192	(0,027)	0,487	(0,053)	41,10	(3,98)	0,033	(0,001)
141	836,2	(59,9)	331,9	(28,1)	0,0551	(0,0022)	3,146	(0,301)	0,192	(0,036)	0,658	(0,075)	43,93	(3,32)	0,031	(0,001)
142	632,1	(32,5)	211,2	(13,3)	0,0376	(0,0026)	1,899	(0,211)	0,134	(0,025)	0,502	(0,043)	23,46	(3,33)	0,030	(0,001)
143	568,2	(42,7)	115,6	(7,8)	0,0114	(0,0005)	0,260	(0,017)	0,249	(0,014)	0,506	(0,023)	3,12	(0,11)	–	
144	665,2	(45,0)	111,7	(6,1)	0,0112	(0,0006)	0,292	(0,021)	0,22	(0,015)	0,481	(0,019)	3,11	(0,11)	0,038	(0,001)
145	1778	(70,2)	364,3	(16,8)	0,0364	(0,0017)	1,898	(0,184)	0,11	(0,015)	0,380	(0,034)	45,12	(7,65)	0,043	(0,002)
MA17	571,1	(15,5)	160,8	(9,0)	0,1057	(0,0041)	2,103	(0,160)	0,254	(0,020)	0,879	(0,041)	25,52	(1,96)	–	
MA18	445,4	(19,2)	234,9	(12,0)	0,1233	(0,0036)	2,201	(0,147)	0,37	(0,026)	1,128	(0,043)	32,75	(2,57)	0,011	(0,001)
MA20	591,8	(50,1)	236,3	(14,3)	0,0870	(0,0037)	2,375	(0,309)	0,301	(0,075)	1,171	(0,164)	45,74	(5,85)	0,022	(0,002)
MA21	354,4	(10,0)	108,8	(2,5)	0,0987	(0,0022)	1,362	(0,091)	0,169	(0,011)	0,734	(0,043)	16,49	(1,05)	0,009	(0,001)
MA22	296,0	(10,9)	100,6	(2,2)	0,1129	(0,0039)	1,695	(0,108)	0,154	(0,020)	0,806	(0,024)	11,85	(0,55)	–	

D_M	D_{Ta}		D_{Ge}		D_{As}		D_{Mo}		D_P		D_W	
50	–		54,7	(2,5)	–		744	(37)	0,71	(0,18)	10,0	(1,5)
51	–		49,7	(2,4)	–		705	(43)	0,76	(0,13)	11,2	(1,7)
52	–		326,1	(33,9)	–		782	(135)	9,45	(4,80)	26,3	(3,4)
85	–		68,8	(9,7)	–		–		0,51	(0,12)	31,4	(3,5)
93	–		258,2	(33,5)	–		2164	(254)	2,52	(0,39)	103,5	(5,4)
94	0,0022	(0,0007)	84,2	(6,9)	1769	(473)	2132	(278)	1,01	(0,09)	43,0	(2,5)
95	–		62,6	(4,1)	1451	(531)	1591	(193)	0,68	(0,09)	34,8	(1,9)
96	0,0027	(0,0007)	25,0	(6,2)	371	(104)	360	(29)	0,15	(0,03)	4,7	(0,3)
97	0,0012	(0,0004)	33,1	(4,7)	710	(227)	1100	(169)	1,32	(0,21)	44,2	(3,1)
101	–		328,3	(8,7)	–		7692	(1304)	20,35	(1,90)	518,9	(75,0)
102	–		–		–		–		3,49	(0,46)	–	
103	–		–		–		–		1,71	(0,20)	40,0	(6,0)
116	0,0039	(0,0005)	199,3	(16,7)	18405	(3486)	14847	(1240)	15,57	(1,46)	737,6	(31,9)
118	–		188,1	(19,9)	–		13193	(1088)	13,63	(0,94)	616,3	(40,5)
120	0,0575	(0,0110)	–		–		–		4,32	(0,59)	–	
121	–		135,3	(8,4)	–		9143	(3091)	14,23	(1,14)	–	
122	–		119,1	(6,4)	6484	(839)	5714	(2287)	18,23	(1,60)	–	
124	0,0037	(0,0004)	168,6	(14,5)	4516	(2276)	4291	(1437)	8,01	(0,86)	275,7	(20,9)
126	0,0019	(0,0001)	159,8	(8,3)	18912	(3846)	13722	(622)	55,26	(5,19)	969,6	(43,9)
127	–		267,7	(29,0)	–		15901	(7233)	44,51	(3,52)	1315,3	(79,8)
128	–		360,9	(34,6)	–		17851	(17901)	36,52	(3,47)	1483,0	(149,2)
129	0,0168	(0,0014)	79,9	(6,9)	5364	(595)	4322	(1449)	8,14	(0,92)	222,8	(20,6)
130	0,0104	(0,0012)	56,1	(7,3)	3323	(588)	3392	(444)	11,56	(1,01)	283,6	(18,5)
131	0,0114	(0,0007)	61,1	(2,3)	4353	(606)	2527	(67)	11,38	(2,07)	230,4	(38,0)
132	0,0181	(0,0016)	57,7	(4,6)	4676	(669)	1487	(662)	16,74	(2,43)	228,4	(12,8)
133	–		–		–		–		13,54	(0,95)	–	
134	0,0015	(0,0003)	127,5	(9,1)	4264	(2140)	14522	(2350)	40,87	(11,10)	–	
135	–		747,0	(94,1)	–		73947	(4980)	245,57	(123,27)	4366	(875)
139	0,0009	(0,0004)	791,7	(56,7)	17431	(937)	3015	(262)	182,86	(36,30)	–	
140	0,0016	(0,0003)	1140,2	(50,8)	16139	(2426)	2239	(138)	34,83	(4,63)	172,9	(14,6)
141	–		1091,3	(105,6)	–		2246	(192)	30,93	(2,98)	104,5	(29,5)
142	–		427,4	(53,9)	6490	(773)	411	(24)	2,75	(0,39)	37,5	(6,4)
143	–		179,0	(17,3)	–		7504	(4291)	21,59	(1,80)	447,3	(58,9)
144	0,0026	(0,0004)	178,8	(9,0)	–		8846	(630)	12,07	(0,81)	338,5	(33,2)
145	–		791,2	(51,4)	14598	(3943)	2381	(159)	10,76	(1,70)	46,4	(2,4)

Appendix C (*continued*)

D_M	D_{Ta}		D_{Ge}		D_{As}		D_{Mo}		D_P		D_W	
MA17	–		1382,4	(159,6)	8057	(1093)	1539	(176)	301,44	(86,32)	–	
MA18	0,0017	(0,0004)	1279,1	(151,8)	4591	(562)	1030	(115)	515,25	(258,05)	152,0	(6,4)
MA20	0,0045	(0,0007)	996,7	(154,8)	9958	(2018)	1161	(91)	102,73	(6,03)	338,0	(39,1)
MA21	0,0027	(0,0005)	844,2	(54,9)	3639	(142)	628	(40)	406,75	(82,40)	139,2	(3,9)
MA22	–	–	826,0	(80,6)	3736	(292)	886	(58)	410,89	(82,94)	117,2	(4,8)

Appendix D

(A) Summary of interaction parameters used to calculate activity coefficients in carbon saturated multicomponent iron alloy (experiments using graphite capsules). (B) Summary of interaction parameters used to calculate activity coefficients in carbon unsaturated multicomponent iron alloy (experiments using a MgO capsules).

ε_{ij}	C	Si	P	V	Cr	Mn	Co	Ni	Ga	Ge	Nb	Mo	Ta	W	As	Zn
C	12.81	3.62	3.98	−2.12	−1.00	−0.66	0.45	0.92	2.62	3.04	−2.58	−1.11	−2.39	−3.05	3.12	4.00
Si	3.62	12.41	11.93	5.24	−0.01	−3.22	–	1.16	–	–	−0.66	43.00	27.57	–	–	–
P	3.98	11.95	7.33	−4.95	−3.79	−6.35	0.92	0.67	–	–	−5.26	−0.32	–	−17.50	–	–
V	−2.12	5.26	−4.91	6.57	2.62	1.28	–	–	–	–	–	–	–	–	–	–
Cr	−1.00	0.02	−3.76	2.61	–	0.90	−4.76	–	–	–	–	–	–	–	–	–
Mn	−0.66	−3.29	−6.33	1.28	0.91	0.02	−0.90	−1.75	–	–	2.11	1.10	0.38	3.05	–	–
Co	0.45	–	0.92	–	−4.73	−0.90	1.18	–	–	–	–	–	–	–	–	–
Ni	0.92	1.19	0.67	–	–	−1.75	–	0.12	–	–	–	–	–	–	–	–
Ga	2.62	–	–	–	–	–	–	–	–	1.79	–	–	–	–	–	–
Ge	3.04	–	–	–	–	–	–	–	1.79	–	–	–	–	–	–	–
Nb	−2.58	−0.66	−5.30	–	–	2.10	–	–	–	–	−0.66	–	–	–	–	–
Mo	−1.11	43.00	−0.32	–	–	1.10	–	–	–	–	–	3.98	–	–	–	–
Ta	−2.39	27.10	0	–	–	0.39	–	–	–	–	–	–	79.74	–	–	–
W	−3.05	–	−17.73	–	–	3.06	–	–	–	–	–	–	–	–	–	–
As	3.12	–	–	–	–	0	–	–	–	–	–	–	–	–	–	–
Zn	4.00	–	–	–	–	0	–	–	–	–	–	–	–	–	–	–
γ_i^0	−0.62	−6.65	–	−2.53	–	0.36	−0.60	−0.42	–	–	−1.61	–	−3.22	–	–	–

ε_{ij}	C	Si	P	V	Cr	Mn	Co	Ni	Ga	Ge	Nb	Mo	Ta	W	As	Zn
C	12.81	9.75	6.95	−6.01	−4.86	−1.84	1.74	2.33	–	2.09	−22.72	−5.98	−169.9	−6.37	12.93	–
Si	9.69	12.41	11.93	5.24	−0.01	−3.22	–	1.16	–	–	−0.66	43.00	27.57	–	–	–
P	7.02	11.95	7.33	−4.95	−3.79	−6.35	0.92	0.67	–	–	−5.26	−0.32	–	−17.50	–	–
V	−5.95	5.26	−4.91	6.57	2.62	1.28	–	–	–	–	–	–	–	–	–	–
Cr	−4.85	0.02	−3.76	2.61	–	0.90	−4.76	–	–	–	−0.01	–	–	–	–	–
Mn	−1.88	−3.29	−6.33	1.28	0.91	0.02	−0.90	−1.75	–	–	2.11	1.10	0.38	3.05	–	–
Co	1.75	–	0.92	–	−4.73	−0.90	1.18	–	–	–	–	–	–	–	–	–
Ni	2.33	1.19	0.67	–	–	−1.75	–	0.12	–	–	–	–	–	–	–	–
Ga	–	–	–	–	–	–	–	–	–	–	–	–	–	–	–	–
Ge	2.27	–	–	–	–	–	–	–	–	1.79	–	–	–	–	–	–
Nb	−22.74	−0.66	−5.30	–	–	2.10	–	–	–	–	−0.66	–	–	–	–	–
Mo	−5.99	43.00	−0.32	–	–	1.10	–	–	–	–	–	3.98	–	–	–	–
Ta	−168.65	27.10	–	–	–	0.39	–	–	–	–	–	–	79.74	–	–	–
W	−6.47	–	−17.73	–	–	3.06	–	–	–	–	–	–	–	–	–	–
As	13.15	–	–	–	–	–	–	–	–	–	–	–	–	–	–	–
Zn	0	–	–	–	–	–	–	–	–	–	–	–	–	–	–	–
γ_i^0	−0.62	−6.65	–	−2.53	–	0.36	−0.60	−0.42	–	–	−1.61	–	−3.22	–	–	–

Appendix E

Summary of experimentally determined valence states of siderophile elements in silicate melts.

Element	T range (°C)	P range (GPa)	fO$_2$ range	Valence state	References[b]
Ni	1300–2200	0-8	Air–ΔIW-4.4[a]	2+	1–6
Co	1300–2200	0–5	Air–ΔIW-3	2+	1,2,4
Mn	1260–2200	0–18	ΔIW-1–ΔIW-6	2+	6–8[*],9
Zn	1740–2200	2–8	ΔIW-1.5–ΔIW-4.4	2+	6,9
Cr	1260–2200	0–18	ΔIW-1–ΔIW-6	2+, (3+)[c]	6,7,(8[*])[c]
V	1260–2200	0–18	ΔIW-1–ΔIW-6	3+, (2+)	7,(8[*]),9
Ga	1260–2200	0–8	ΔIW+2–ΔIW-4.4	3+, (2+)	6, (9),10,11
Ge	1260–1600	0	ΔIW+2–ΔIW-3	2+, 4+	10, 11
W	1300–2500	0–18	IW–ΔIW-4	4+, 6+	11–15
Mo	1300–2500	0-7	IW- ΔIW-3	4+, 6+	1, 11, 13, 16
Nb	1740–2300	2–25	ΔIW-1–ΔIW-4.4	5+	6, 9, 17
Ta	1740–2200	2-8	ΔIW-1.5–ΔIW-4.4	5+	6, 9
P	1190–1600	0	IW–ΔIW-3	5+	11 ,18
As	–	–	–	–	–

[a] Oxygen fugacity relative to the iron-wüstite (IW) buffer calculated assuming ideal mixing behavior.

[b] Chosen references give a representative sample group of available data without the expectance of cited all available data references complete. Given P, T, fO$_2$ represent roughly the studied ranges of cited experimental works for each element.

[c] Determined exotic value for the valence and associated references are given in parentheses. [1] Holzheid et al. (1994), [2] Capobianco and Amelin (1994), [3] Dingwell et al. (1994), [4] Thibault and Walter (1995), [5] Righter and Drake (1997), [6] Corgne et al. (2008), [7] Drake et al. (1989) and [8] Gessmann et al. (1999).

[*] MgO is taken as a proxy for silicate melt; [9] Mann et al. (2009), [10] Capobianco et al. (1999), [11] Schmitt et al. (1989), [12] Ertel et al. (1996), [13] Walter and Thibault (1995), [14] Cottrell et al. (2009), [15] O'Neill et al. (2008), [16] O'Neill and Eggins (2002), [17] Wade and Wood (2001), [18] Newsom and Drake (1983).

Appendix F
Summary of regression coefficients determined from superliquidus metal-silicate partitioning experimental studies.[a]

Element	v[b]	a	±	b	±	c	±	d	±
Ni									
This work	2	0.35	0.07	2934	279	−83	17	–	–
Gessmann and Rubie (2000)	2	0.78	0.23	1657	543	−66	6	–	–
Li and Agee (2001)	2	1.35	–	2558	–	−81	–	–	–
Chabot et al. (2005)	2	0.18	0.02	3600	630	−68	4	–	–
Wade and Wood (2005)	2	0.64	–	3097*	–	−123	9	–	–
Corgne et al. (2008)	2	0.50	–	3100*	–	−78	5	–	–
Kegler et al. (2008) + lit. (> 5GPa)	2	0.26	0.21	3284	453	−74	8	–	–
Co									
This work	2	0.20	0.03	1892	238	−66	8	–	–
Gessmann and Rubie (2000)	2	0.17	0.26	1169	601	−34	8	–	–
Li and Agee (2001)	2	0.11	–	3046	–	−30	–	–	–
Chabot et al. (2005)	2	0.33	0.02	1702	378	−31	3	–	–
Wade and Wood (2005)	2	0.01	–	2511*	–	−45	11	–	–
Kegler et al. (2008) + lit. (> 5GPa)	2	0.30	0.18	1405	369	−40	7	–	–
Mn									
This work	2	0.53	0.04	−6356	418	46	10	–	–
Gessmann and Rubie (2000)	2	0.79	0.60	−6624	1259	26	17	–	–
Chabot and Agee (2003)	2	−0.22	–	−4777	–	–	–	–	–
Wade and Wood (2005)	2	0.04	–	−5761*	–	−49	16	–	–
Corgne et al. (2008)	2	−0.02	–	−5600*	–	38	6	0.036	0.010
Mann et al. (2009)	2	0.54	0.05	−7142*	–	52	9	–	–
V									
This work	3	−0.46	0.06	−5964	513	−19	14	−0.063	0.026
Gessmann and Rubie (2000)*	2	−0.14	0.91	−5173	2011	24	15	–	–
Chabot and Agee (2003)	3	−0.87	–	−4212	–	–	–	–	–
Wood et al. (2008)	3	0.855	–	−8548*	–	−62	19	−0.101	0.029
Mann et al. (2009)	3	−0.48	0.38	−5063	894	–	–	–	–

Appendix F (*continued*)

Element	v[b]	a	±	b	±	c	±	d	±
Cr									
This work	2	0.26	0.06	−3318	495	13	14	−0.056	0.025
Gessmann and Rubie (2000)	3	−0.15	0.43	−4370	986	34	13	–	–
Chabot and Agee (2003)	2	−0.52	–	−1911	–	–	–	–	–
Wood et al. (2008)	2	0.643	–	−4232	538	−22	13	–	–
Corgne et al. (2008)	2	0.09	–	−2845	461	−20	10	0.000	0.013
Mann et al. (2009)	2	−0.17	0.13	−2730	312	–	–	–	–
Nb									
This work	5	−0.97	0.10	−6855	653	−154	32	−0.23	0.04
Wood et al. (2008)	5	2.837	–	−13240*	–	−114	43	−0.47	0.15
Corgne et al. (2008)	5	4.09	–	−15500*	–	−166	31	−0.75	0.16
Mann et al. (2009)	5	2.66	0.11	−14032*	–	−199	16	–	–
Ga									
This work	3	0.51	0.05	−795	375	−88	12	−0.06	0.02
Corgne et al. (2008)	3	3.50*	–	−4800*		−126	36	−0.97	0.15
Mann et al. (2009)	2	0.52	0.45	−514	914	−78	13	–	–
Zn									
This work	2	0.57	0.03	−3015	406	−26	7	–	–
Corgne et al. (2008)	2	−1.11	–	600*	–	−23	102	−0.21	0.24
Mann et al. (2009)	2	−0.30	0.36	−1574	739	−51	12	–	–
Ta									
This work	5	−3.41	0.12	−7910	969	35	31	–	–
Corgne et al. (2008)	5	7.74	–	−20000*	–	−264	81	−1.69	53
Mann et al. (2009)	5	0.84	0.09	−13806*	–	−101	15	–	–
W									
This work	4	1.96	0.14	−937	741	−55	35	−0.57	0.04
Cottrell et al. (2009) (> 6 GPa)	4 (4.4)	2.02	0.29	–	–	−104	14	−0.84	0.07
Cottrell et al. (2009) (< 6 GPa)	4 (4.7)	1.29	0.16	–	–	553	93	−0.85	–
Wade and Wood (2005)	4	2.39	–	−1605	–	−68	–	−0.79	–
P									
This work	5	2.03	0.17	−2698	1062	99	42	−0.71	0.05
Wade and Wood (2005)	5	0.64	–	−1593	–	−75	–	–	–

* Regression constants are derived from the free energy data.
[a] Chosen references give a representative sample group of available data that parameterize metal–silicate partitioning according to Eq. (13).
[b] Valence state of the element in the silicate liquid.

APPENDIX A

APPENDIX B

APPENDIX C

APPENDIX D

APPENDIX E

APPENDIX F

REFERENCES

Allègre C. J., Poirier J. P., Humler E. and Hofmann A. W. (1995) The chemical composition of the Earth. *Earth Planet. Sci. Lett.* **134**, 515–526.

Allègre C. J., Manhes G. and Lewin E. (2001) Chemical composition of the Earth and the volatility control on planetary genetics. *Earth Planet. Sci. Lett.* **185**, 49–69.

Armstrong J. T. (1995) CITZAF- A package of correction programs for the quantitative electron microbeam X-ray analysis of thick polished materials, thin films, and particles. *Microbeam Anal.* **4**, 177–200.

Asahara Y., Frost D. J. and Rubie D. C. (2007) Partitioning of FeO between magnesiowustite and liquid iron at high pressures and temperatures: implications for the composition of the Earth's outer core. *Earth Planet. Sci. Lett.* **257**, 435–439.

Barin I., Sauert F., Schultze-Rhonhof E. and Sheng W. S. (1989) *Thermochemical Data of Pure Substances, Part I and Part II.* Verlagsgesellschaft, Weinheim, Germany, pp. 1739.

Barrat J. A., Yamaguchi A., Greenwood R. C., Bohn M., Cotten J., Benoit M. and Franchi I. A. (2007) The Stannern trend eucrites: contamination of main group eucritic magmas by crustal partial melts. *Geochim. Cosmochim. Acta* **71**, 4108–4124.

Berry A. J., Neill H. S., Scott D. R., Foran G. J. and Shelley J. M. G. (2006) The effect of composition on Cr^{2+}/Cr^{3+} in silicate melts. *Am. Mineral.* **91**, 1901–1908.

Brenan J. M. and McDonough W. F. (2009) Core formation and metal–silicate fractionation of osmium and iridium from gold. *Nat. Geosci.* **2**, 798–801.

Capobianco C. J. and Amelin A. A. (1994) Metal–silicate partitioning of nickel and cobalt: the influence of temperature and oxygen fugacity. *Geochim. Cosmochim. Acta* **58**, 125–140.

Capobianco C. J., Drake M. J. and De'Aro J. (1999) Siderophile geochemistry of Ga, Ge, and Sn: cationic oxidation states in silicate melts and the effect of composition in iron-nickel alloys. *Geochim. Cosmochim. Acta* **63**, 2667–2677.

Chabot N. L. and Agee C. B. (2003) Core formation in the Earth and Moon: new experimental constraints from V, Cr, and Mn. *Geochim. Cosmochim. Acta* **67**, 2077–2091.

Chabot N. L., Draper D. S. and Agee C. B. (2005) Conditions of Earth's core formation: constraints from nickel and cobalt partitioning. *Geochim. Cosmochim. Acta* **69**, 2141–2151.

Chase M. W. (1998) NIST-JANAF thermochemical tables, 4th edition. *J. Phys. Chem. Ref. data* **9**.

Chipman J. (1972) Thermodynamics and phase diagram of the Fe–C system. *Metall. Mater. Trans. B* **3**, 55–64.

Corgne A., Keshav S., Wood B. J., McDonough W. F. and Fei Y. (2008) Metal–silicate partitioning and constraints on core composition and oxygen fugacity during Earth accretion. *Geochim. Cosmochim. Acta* **72**, 574–589.

Corgne A., Siebert J. and Badro J. (2009) Oxygen as a light element: A solution to single-stage core formation. *Earth Planet. Sci. Lett.* **288**, 108–114.

Cottrell E. and Walker D. (2006) Constraints on core formation from Pt partitioning in mafic silicate liquids at high temperatures. *Geochim. Cosmochim. Acta* **70**, 1565–1580.

Cottrell E., Walter M. J. and Walker D. (2009) Metal–silicate partitioning of tungsten at high pressure and temperature: implications for equilibrium core formation in Earth. *Earth Planet. Sci. Lett.* **281**, 275–287.

Dasgupta R. and Walker D. (2008) Carbon solubility in core melts in a shallow magma ocean environment and distribution of carbon between the Earth's core and the mantle. *Geochim. Cosmochim. Acta* **72**, 4627–4641.

Dingwell D. B., O'Neill H. S. C., Ertel W. and Spettel B. (1994) The solubility and oxidation state of nickel in silicate melt at low oxygen fugacities: results using a mechanically assisted equilibration technique. *Geochim. Cosmochim. Acta* **58**, 1967–1974.

Drake M. J., Newsom H. E. and Capobianco C. J. (1989) V, Cr, and Mn in the Earth, Moon, EPB, and SPB and the origin of the Moon: experimental studies. *Geochim. Cosmochim. Acta* **53**, 2101–2111.

Ertel W., Dingwell D. B. and O'Neill H. S. C. (1996) Solubility of tungsten in haplobasaltic melt as a function of temperature and oxygen fugacity. *Geochim. Cosmochim. Acta* **61**, 1171–1180.

Ertel W., Walter M. J., Drake M. J. and Sylvester P. J. (2006) Experimental study of platinum solubility in silicate melt to 14 GPa and 2273 K: implications for accretion and core formation in Earth. *Geochim. Cosmochim. Acta* **70**, 2591–2602.

Farges F. and Siewert R. (2006) Structural environments around molybdenum in silicate glasses and melts. I. Influence of composition and oxygen fugacity on the local structure of molybdenum. *Can. Mineral.* **44**, 731–753.

Fiquet G., Auzende A. L., Siebert J., Corgne A., Bureau H., Ozawa H. and Garbarino G. (2010) Melting of peridotite to 140 gigapascals. *Science* **329**, 516–518.

Frost D. J., Liebske C., Langenhorst F., McCammon C. A., Tronnes R. G. and Rubie D. C. (2004) Experimental evidence for the existence of iron-rich metal in the Earth's lower mantle. *Nature* **428**, 409–412.

Gagnon J. E., Fryer B. J., Samson I. M. and Williams-Jones A. E. (2008) Quantitative analysis of silicate certified reference materials by LA-ICPMS with and without an internal standard. *J. Anal. At. Spectrom.* **23**, 1529–1537.

Gao S., Liu X., Yuan H., Hattendorf B., Günther D., Chen L. and Hu S. (2002) Determination of forty two major and trace elements in USGS and NIST SRM glasses by laser ablation-inductively coupled plasma-mass spectrometry. *Geostandards Newslett.* **26**, 181–196.

Gessmann C. K. and Rubie D. C. (1998) The effect of temperature on the partitioning of Ni, Co, Mn, Cr and V at 9 GPa and constraints on formation of the Earth's core. *Geochim. Cosmochim. Acta* **62**, 867–882.

Gessmann C. K. and Rubie D. C. (2000) The origin of the depletions of V, Cr and Mn in the mantles of the Earth and Moon. *Earth Planet. Sci. Lett.* **184**, 95–107.

Gessmann C. K., Rubie D. C. and McCammon C. A. (1999) Oxygen fugacity dependence of Ni, Co, Mn, Cr, V and Si partitioning between liquid metal and magnesiowüstite at 9–18 GPa and 2200 °C. *Geochim. Cosmochim. Acta* **63**, 1853–1863.

Hanfland M., Beister H. and Syassen K. (1989) Graphite under pressure: equation of state and first-order Raman modes. *Phys. Rev. B* **39**, 12598–12603.

Hirschmann M. M. and Ghiorso M. S. (1994) Activities of nickel, cobalt, and manganese silicates in magmatic liquids and applications to olivine/liquid and to silicate/metal partitioning. *Geochim. Cosmochim. Acta* **58**, 4109–4126.

Hofmann A. W. and Magaritz M. (1977) Diffusion of Ca, Sr, Ba, and Co in basalt melt – implications for geochemistry of mantle. *J. Geophys. Res.* **82**, 5432–5440.

Holzapfel C., Courtial P., Chakraborty S. and Palme H. (2001) Experimental determination of partial molar volumes of Ga_2O_3 and GeO_2 in silicate melts: implications for the pressure dependence of metal–silicate partition coefficients. *Chem. Geol.* **174**, 33–49.

Holzheid A., Borisov A. and Palme H. (1994) The effect of oxygen fugacity and temperature on solubilities of nickel, cobalt, and molybdenum in silicate melts. *Geochim. Cosmochim. Acta* **58**, 1975–1981.

Holzheid A., Palme H. and Chakraborty S. (1997) The activities of NiO, CoO and FeO in silicate melts. *Chem. Geol.* **139**, 21–38.

Holzheid A., Sylvester P., O'Neill H. S. C., Rubie D. C. and Palme H. (2000) Evidence of a late chondritic veneer in the Earth's mantle from high-pressure partitioning of palladium and platinum. *Nature* **406**, 396–399.

Jaeger W. L. and Drake M. J. (2000) Metal–silicate partitioning of Co, Ga, and W: dependence on silicate melt composition. *Geochim. Cosmochim. Acta* **64**, 3887–3895.

Jana D. and Walker D. (1997a) The impact of carbon on element distribution during core formation. *Geochim. Cosmochim. Acta* **61**, 2759–2763.

Jana D. and Walker D. (1997b) The influence of silicate melt composition on distribution of siderophile elements among metal and silicate liquids. *Earth Planet. Sci. Lett.* **150**, 463–472.

Jimbo I. and Cramb A. W. (1993) The density of liquid iron–carbon alloys. *Metall. Trans. B* **24**, 5–10.

Jochum K. P., Willbold M., Raczek I., Stoll B. and Herwig K. (2005) Chemical characterisation of the USGS reference glasses GSA-1G, GSC-1G, GSD-1G, GSE-1G, BCR-2G, BHVO-2G and BIR-1G using EPMA, ID-TIMS, ID-ICP-MS and LA-ICPMS. *Geostand. Geoanal. Res.* **29**, 285–302.

Karner J. M., Papike J. J., Sutton S. R., Shearer C. K., Burger P., McKay G. and Le L. (2008) Valence state partitioning of V between pyroxene-melt: effects of pyroxene and melt composition, and direct determination of V valence states by XANES. Application to Martian basalt QUE 94201 composition. *Meteorit. Planet. Sci.* **43**, 1275–1285.

Kegler P., Holzheid A., Frost D. J., Rubie D. C., Dohmen R. and Palme H. (2008) New Ni and Co metal–silicate partitioning data and their relevance for an early terrestrial magma ocean. *Earth Planet. Sci. Lett.* **268**, 28–40.

Li J. and Agee C. B. (1996) Geochemistry of mantle-core differentiation at high pressure. *Nature* **381**, 686–689.

Li J. and Agee C. B. (2001) The effect of pressure, temperature, oxygen fugacity and composition on the partitioning of nickel and cobalt between liquid Fe–Ni–S alloy and liquid silicate: implications for the Earth's core formation. *Geochim. Cosmochim. Acta* **65**, 1821–1832.

Lodders K. (2003) Solar system abundances and condensation temperatures of the elements. *Astrophys. J.* **591**, 1220–1247.

Ma Z. (2001) Thermodynamic description for concentrated metallic solutions using interaction parameters. *Metall. Mater. Trans. B* **32**, 87–103.

Mann U., Frost D. J. and Rubie D. C. (2009) Evidence for high-pressure core–mantle differentiation from the metal–silicate partitioning of lithophile and weakly-siderophile elements. *Geochim. Cosmochim. Acta* **73**, 7360–7386.

McDade P., Wood B. J., Van Westrenen W., Brooker R., Gudmundsson G., Soulard H., Najorka J. and Blundy J. (2002) Pressure corrections for a selection of piston-cylinder cell assemblies. *Mineral. Mag.* **66**, 1021–1028.

McDonough W. F. (2003) Compositional model for the Earth's core. In *Treatise on Geochemistry, vol. 2* (ed. R. W. Carlson). Elsevier-Pergamon, Oxford. pp. 547–568.

McDonough W. F. and Sun S. S. (1995) The composition of the Earth. *Chem. Geol.* **120**, 223–253.

McSkimin H. J. and Andreatch P. (1972) Elastic moduli of diamonds as a function of pressure and temperature. *J. Appl. Phys.* **43**, 2944–2945.

Mysen B. O., Virgo D. and Seifert F. A. (1982) The structure of silicate melts: Implications for chemical and physical properties of natural magma. *Rev. Geophys. Space Phys.* **20**, 353–383.

Nakajima Y., Takahashi E., Suzuki T. and Funakoshi K. (2009) "Carbon in the core" revisited. *Phys. Earth Planet. In.* **174**, 202–211.

Newsom H. E. (1990) Accretion and core formation in the Earth: evidence from siderophile elements. In *The Origin of the Earth* (eds. H. E. Newsom and J. H. Jones). Oxford Univ. Press, New York. pp. 273–288.

Newsom H. E. and Drake M. J. (1983) Experimental investigations of the partitioning of phosphorus between metal and silicate phases: implications for the Earth, Moon and eucrite parent body. *Geochim. Cosmochim. Acta* **47**, 93–100.

Newsom H. E. and Sims K. W. W. (1991) Core formation during early accretion of the Earth. *Science* **252**, 926–933.

Ogino K., Nishiwaki A. and Hosotani Y. (1984) Density of molten Fe–C alloys. *J. Iron Steel Inst. Jpn.* **10**, 1004–1010.

Ohtani E., Yurimoto H. and Seto S. (1997) Element partitioning between metallic liquid, silicate liquid, and lower-mantle minerals: implications for core formation of the Earth. *Phys. Earth Planet. In.* **100**, 97–114.

O'Neill H. S. C. (1991) The origin of the Moon and the early history of the Earth-A chemical model. Part 2: the Earth. *Geochim. Cosmochim. Acta* **55**, 1159–1172.

O'Neill H. S. C. and Berry A. J. (2006) Activity coefficients at low dilution of CrO, NiO and CoO in melts in the system CaO–MgO–Al_2O_3–SiO_2 at 1400 °C: using the thermodynamic behaviour of transition metal oxides in silicate melts to probe their structure. *Chem. Geol.* **231**, 77–89.

O'Neill H. S. C. and Eggins S. M. (2002) The effect of melt composition on trace element partitioning: an experimental investigation of the activity coefficients of FeO, NiO, CoO, MoO_2 and MoO_3 in silicate melts. *Chem. Geol.* **186**, 151–181.

O'Neill H. S. C., Canil D. and Rubie D. C. (1998) Oxide–metal equilibria to 2500 C and 25 GPa: implications for core formation and the light component in the Earth's core. *J. Geophys. Res.* **13**, 12239–12260.

O'Neill H. S. C., Berry A. J. and Eggins S. M. (2008) The solubility and oxidation state of tungsten in silicate melts: implications for the comparative chemistry of W and Mo in planetary differentiation process. *Chem. Geol.* **255**, 346–359.

Palme H. and O'Neill H. S. C. (2003) Cosmochemical estimates of mantle composition. In *Treatise on Geochemistry, vol. 2* (ed. R. W. Carlson). Elsevier-Pergamon, Oxford. pp. 1–38.

Pearce N. J. G., Perkins W. T., Westgate J. A., Gorton M. P., Jackson S. E., Neal C. R. and Chenery S. P. (1997) A compilation of new and published major and trace element data for NIST SRM 610 and NIST SRM 612 glass reference materials. *Geostandards Newsletter* **21**, 115–144.

Perkins D., Holland T. J. B. and Newton R. C. (1981) The Al2O3 contents of enstatite in equilibrium with garnet in the system

MgO–Al$_2$O$_3$–SiO$_2$ at 15–40 kbar and 900–1600 °C. *Contrib. Mineral. Petrol.* **78**, 99–109.

Righter K. and Drake M. J. (1999) Effect of water on metal–silicate partitioning of siderophile elements: a high pressure and temperature terrestrial magma ocean and core formation. *Earth Planet. Sci. Lett.* **171**, 383–399.

Righter K. and Drake M. J. (2000) Metal/silicate equilibrium in the early Earth – new constraints from the volatile moderately siderophile elements Ga, Cu, P, and Sn. *Geochim. Cosmochim. Acta* **64**, 3581–3597.

Righter K., Drake M. J. and Yaxley G. (1997) Prediction of siderophile element metal–silicate partition coefficients to 20 GPa and 2800 °C: the effects of pressure, temperature, oxygen fugacity and silicate and metallic melt compositions. *Phys. Earth Planet. In.* **100**, 115–134.

Righter K., Sutton S. R., Newville M., Lei L., Schwandt C. S., Uchida H., Lavina B. and Downs R. T. (2006) An experimental study of the oxidation state of vanadium in spinel and basaltic melt with implications for the origin of planetary basalt. *Am. Mineral.* **91**, 1643–1656.

Righter K., Humayun M. and Danielson L. (2008) Partitioning of palladium at high pressures and temperatures during core formation. *Nat. Geosci.* **1**, 321–323.

Righter K., Pando K. M., Danielson L. and Lee C. (2010) Partitioning of Mo, P and other siderophile elements (Cu, Ga, Sn, Ni, Co, Mn, Cr, V and W) between metal and silicate melt as a function of temperature and silicate melt composition. *Earth Planet. Sci. Lett.* **291**, 1–9.

Ringwood A. E. (1966) Chemical evolution of the terrestrial planets. *Geochim. Cosmochim. Acta* **30**, 41–104.

Ringwood A. E., Kato T., Hibberson W. and Ware N. (1991) Partitioning of Cr, V and Mn between mantles and cores of differentiated planetesimals – implications for giant impact hypotheses of lunar origin. *Icarus* **89**, 122–128.

Robie R. A., Hemingway B. S. and Fisher J. R. (1978) Thermodynamic properties of mineral and related substances at 298.15 K and 1 bar (10^5 Pascals) pressure and higher temperatures. *U.S. Geol. Surv. Bull.* **1452**.

Rubie D. C., Melosh H. J., Reid J. E., Liebske C. and Righter K. (2003) Mechanisms of metal–silicate equilibration in the terrestrial magma ocean. *Earth Planet. Sci. Lett.* **205**, 239–255.

Ryerson F. J. (1985) Oxide solution mechanisms in silicate melts - systematic variations in the activity-coefficient of SiO$_2$. *Geochim. Cosmochim. Acta* **49**, 637–649.

Schmitt W., Palme H. and Wänke H. (1989) Experimental determination of metal/silicate partition coefficients for P, Co, Ni, Cu, Ga, Ge, Mo, and W and some implications for the early evolution of the Earth. *Geochim. Cosmochim. Acta* **53**, 173–185.

Shaheen M., Gagnon J. E., Yang Z. and Fryer B. J. (2008) Evaluation of the analytical performance of femtosecond laser ablation inductively coupled mass spectrometry at 785 nm with glass reference materials. *J. Anal. At. Spectrom.* **23**, 1610–1621.

Skinner B. J. (1966) Thermal expansion. In *Handbook of physical constants* (ed. S.P. Clark). Geol. Soc. Am. Mem., New York. pp. 75–95.

Stevenson D. J. (1990) Fluids dynamics of core formation. In *The Origin of the Earth* (eds. H. E. Newsom and J. H. Jones). Oxford Univ. Press, New York. pp. 231–249.

The Japan Society for the Promotion of Science and The Nineteenth Committee on Steelmaking (1988) Part 2: Recommended values of activity and activity coefficients, and interaction parameters of elements in iron alloys. In *Steelmaking Data Sourcebook*. Gordon and Breach Science Publishers, New York. pp. 273–297.

Thibault Y. and Walter M. J. (1995) The influence of pressure and temperature on the metal–silicate partition coefficients of nickel and cobalt in a model C1 chondrite and implications for metal segregation in a deep magma ocean. *Geochim. Cosmochim. Acta* **59**, 991–1002.

Van Achterbergh E., Ryan C. G., Jackson S. E. and Griffin W. L. (2001) Data reduction software for LA-ICP-MS. In *Laser-ablation-ICPMS in the earth sciences: principles and applications* (ed. P. Sylvester). Mineralog. Assoc. Can., Short Course Series, Ottawa. pp. 239–243.

Wade J. and Wood B. J. (2001) The Earth's missing niobium may be in the core. *Nature* **409**, 75–78.

Wade J. and Wood B. J. (2002) A high-temperature (3000 K) assembly for piston cylinder experiments. *Geochem. Geophys. Geosyst.* **3**, art. no. 1006.

Wade J. and Wood B. J. (2005) Core formation and the oxidation state of the Earth. *Earth Planet. Sci. Lett.* **236**, 78–95.

Walter M. J. and Thibault Y. (1995) Partitioning of tungsten and molybdenum between metallic liquid and silicate melt. *Science* **270**, 1186–1189.

Walter M. J., Newsom H. E., Ertel W. and Holzheid A. (2000) Siderophile elements in the Earth and Moon. Metal/silicate partitioning and implication for core formation. In *Origin of the Earth and Moon* (eds. R. M. Canup and K. Righter). University of Arizona Press, Tucson. pp. 265–289.

Wänke H. (1981) Constitution of terrestrial planets. *Phil. Trans. Roy. Soc. London* **A303**, 287–302.

Wänke H. and Dreibus G. (1988) Chemical composition and accretion history of terrestrial planets. *Phil. Trans. R. Soc. London* **A325**, 545–557.

Wasson J. T. (1985) *Meteorites: their record of early solar-system history*. W.H. Freeman, New York.

Wood B. J. (1993) Carbon in the core. *Earth Planet. Sci. Lett.* **117**, 593–607.

Wood B. J., Wade J. and Kilburn M. R. (2008) Core formation and the oxidation state of the Earth: additional constraints from Nb, V and Cr partitioning. *Geochim. Cosmochim. Acta* **72**, 1415–1426.

Zerr A., Diegeler A. and Boehler R. (1998) Solidus of Earth's deep mantle. *Science* **281**, 243–246.

Associate editor: Richard J. Walker